

Lawrence Berkeley National Laboratory

Lawrence Berkeley National Laboratory

Title

Toward Femtosecond X-ray Spectroscopy at the Advanced Light Source

Permalink

<https://escholarship.org/uc/item/4x26q126>

Author

Chong, Henry Heng Wei

Publication Date

2004-04-16

Toward Femtosecond X-ray Spectroscopy at the Advanced Light Source

by

Henry Heng Wei Chong

B.S. (Massachusetts Institute of Technology) 1996
M.Eng. (Massachusetts Institute of Technology) 1997

A dissertation submitted in partial satisfaction of the
requirement for the degree of

Doctor of Philosophy
in

Applied Science and Technology

in the

GRADUATE DIVISION

of the

UNIVERSITY OF CALIFORNIA, BERKELEY

Committee in charge:

Professor Charles V. Shank, Chair
Professor David T. Attwood
Professor Graham R. Fleming

Spring 2004

The dissertation of Henry Heng Wei Chong is approved:

Charles V. Shank, Chair

Date

David T. Attwood

Date

Graham R. Fleming

Date

University of California, Berkeley

Spring 2004

Toward Femtosecond X-ray Spectroscopy at the Advanced Light Source

© 2004

by

Henry Heng Wei Chong

Abstract

Toward Femtosecond X-ray Spectroscopy at the Advanced Light Source

by

Henry Heng Wei Chong

Doctor of Philosophy in Applied Science and Technology

University of California, Berkeley

Professor Charles V. Shank, Chair

The realization of tunable, ultrashort pulse x-ray sources promises to open new venues of science and to shed new light on long-standing problems in condensed matter physics and chemistry. Fundamentally new information can now be accessed. Used in a pump-probe spectroscopy, ultrashort x-ray pulses provide a means to monitor atomic re-arrangement and changes in electronic structure in condensed-matter and chemical systems on the physically-limiting time-scales of atomic motion. This opens the way for the study of fast structural dynamics and the role they play in phase transitions, chemical reactions and the emergence of exotic properties in materials with strongly interacting degrees of freedom.

The ultrashort pulse x-ray source developed at the Advanced Light Source at the Lawrence Berkeley Laboratory is based on electron slicing in storage rings, and generates ~100 femtosecond pulses of synchrotron radiation spanning wavelengths from the far-infrared to the hard x-ray region of the electromagnetic spectrum. The tunability of the source allows for the adaptation of a broad range of static x-ray spectroscopies to useful pump-probe measurements.

Initial experiments are attempted on transition metal complexes that exhibit relatively large structural changes upon photo-excitation and which have excited-state evolution determined by strongly interacting structural, electronic and magnetic degrees of freedom. Specifically, iron(II) complexes undergo a spin-crossover transition upon

optical irradiation. The dynamics of the transition involve a metal-to-ligand charge transfer, a $\Delta S=2$ change in magnetic moment and 10% bond dilation in the first coordination shell of the iron. Studies of the electronic dynamics are studied with time-resolved optical absorption measurements. The current progress of time-resolved structural studies to complete the picture of the spin-crossover transition is presented.

TABLE OF CONTENTS

1. An Introduction, Context and Motivation	1
1.1 Why: Atoms Sit Still for No One.	1
1.2 How: Ultrafast Meets X-rays.	2
1.3 Overview	5
2. Tools	7
2.1 Sources	7
2.1.1 History and the State-of-the-Art	7
2.1.2 Requirements for the Ideal Ultrashort X-ray Pulse Source	10
2.1.3 Looking Forward	15
2.2 Spectroscopic Techniques and Detection Schemes	16
2.2.1 Techniques	16
2.2.2 Detection	22
3. Ultrashort X-ray Pulses at the Advanced Light Source	25
3.1 Rudiments of Synchrotron Radiators	25
3.1.1 Bend Magnets	25
3.1.2 Insertion Devices	26
3.2 Slicing in a Storage Ring	29
3.2.1 Pictures at an Exhibition	29
3.2.2 Mathematical Considerations	35
3.3 Implementation at the Advanced Light Source: Beamline 5.3.1	38
3.4 Source Characterization	42
3.4.1 Single-Pass Electron Laser Gain	42
3.4.2 Visible Light Cross-correlation	44
3.4.3 Spatial Beam Profile at ALS Beamline 5.3.1	46
4. Time -Resolved Studies of Transition Metal Complexes	48
4.1 Engineering Molecular Properties	49
4.2 An Example: Fe[py ₃ tren] ²⁺	51
4.3 Excited-State Dynamics of Fe[py ₃ tren] ²⁺	54
4.4 Feasibility Calculations for Optical Pump/X-ray Probe Measurements	61
4.5 Experimental Considerations and Difficulties	67
5. Consideration for Future Work	73
References	77
Appendices	82

LIST OF FIGURES

Figure 1.1: Radial electron density distribution for hydrogenic atom	3
Figure 1.2: Schematic of experimental apparatus for pump-probe spectroscopy	4
Figure 2.1: Laser-electron interaction in 90° Thomson Scattering Source	9
Figure 2.2: Sample damage in Fe[py ₃ tren]Cl ₂ due to x-ray radiation and thermal melting	13
Figure 2.3: Synchronization jitter in pump-probe experiments	14
Figure 2.4: X-ray absorption features	19
Figure 2.5: EXAFS computation for octahedral iron-nitrogen complex at the iron K-edge	20
Figure 2.6: Photo-electron interference in EXAFS	21
Figure 3.1: Bend magnet	26
Figure 3.2: Insertion device	27
Figure 3.3: Hertzian dipole gain pattern	28
Figure 3.4: Insertion device spontaneous emission spectrum	28
Figure 3.5: Doppler shift of radiation due to relativistic electron propagation	29
Figure 3.6: Electron slicing overview	30
Figure 3.7: Electron energy modulation: Laser light polarization projected on to electron transverse velocity	31
Figure 3.8: Electron energy modulation: Resonance condition	32
Figure 3.9: Electron energy modulation: Phase slippage	33
Figure 3.10: Electron slice separation and radiation	34
Figure 3.11: Overview of Advanced Light Source	39

Figure 3.12: Ti:sapphire ultrashort pulse laser system	40
Figure 3.13: Overview of ALS beamline 5.3.1.	42
Figure 3.14: Schematic for single-pass free-electron laser gain measurements	43
Figure 3.15: Plot of single-pass free-electron laser gain measurement	44
Figure 3.16: Schematic of visible light cross-correlation diagnostic	45
Figure 3.17: Plot of visible light cross-correlation measurements	45
Figure 3.18: Schematic of x-ray beam profile apparatus	46
Figure 3.19: Plots of x-ray beam profile at ALS beamline 5.3.1.	47
Figure 4.1: Schematic of Co[acac] ₃	48
Figure 4.2: Orientation of constant density surfaces of atomic d-orbitals	49
Figure 4.3: Ligand-field splitting of atomic d-orbitals	50
Figure 4.4: Fe[py ₃ tren] ²⁺ schematic and iron-nitrogen bond lengths	52
Figure 4.5: Tanabe-Sugano diagram for octahedral <i>d</i> ⁶ systems explicit electronic configurations for ground states	53
Figure 4.6: Electronic dynamics of Fe[py ₃ tren] ²⁺ with time-resolved optical absorption plots of solution- and solid-state samples	55
Figure 4.7: Steric distortions associated with spin-crossover transitions	57
Figure 4.8: Bond length comparison of Fe[py ₃ tren] ²⁺ and Fe[Me-py ₃ tren] ²⁺	58
Figure 4.9: Scenario for spin-crossover transition driven by electronic dynamics in the MLCT state	59
Figure 4.10: Tanabe-Sugano diagrams for octahedral <i>d</i> ⁵ and <i>d</i> ⁶ systems	60
Figure 4.11: Crystal structure, optical absorption spectrum and x-ray attenuation spectrum of Fe[py ₃ tren]Cl ₂	63
Figure 4.12: Sample photolysis computation for Fe[py ₃ tren]Cl ₂	64

Figure 4.13: Single-wavelength, pump-probe measurements of Fe[py ₃ tren]Cl ₂ crystals at different excitation fluences	65
Figure 4.14: Sample thickness optimization computation for Fe[py ₃ tren]Cl ₂	66
Figure 4.15: Silicon nitride window and sample	69
Figure 4.16: Gas flow chamber for convective thermal relief	70
Figure 4.17: X-ray spectrum and damage of Fe[py ₃ tren]Cl ₂ in white-light transmission experimental geometry	71
Figure 4.18: X-ray spectrum and damage of Fe[py ₃ tren]Cl ₂ in monochromatic-light transmission experimental geometry	72

LIST OF TABLES

Table 2.1: Feasibility estimates for two candidate experimental systems	12
Table 2.2: Ideal Properties for Ultrashort X-ray Pulse Sources	15
Table 4.1: Experimental parameters and expectations for a time-resolved x-ray measurement on Fe[py ₃ tren]Cl ₂ crystals at the iron L-edge.	67

ACKNOWLEDGEMENTS

My graduate school experience has been unique. As a student at Lawrence Berkeley Lab, I have benefited from the collective wisdom and perspective of scientists from around the world at various stages of their careers, and have been privy to a perspective on the scientific enterprise that ranges from day-to-day activities in laser lab to long-term plans and considerations for a national user facility. I have enjoyed my time as a student, and have many to thank for my experience.

My greatest thanks are extended to Bob. He is a cherished mentor and advisor and close colleague. He took a chance on me when all I had to offer was enthusiasm and a background completely unrelated to the group's scientific interests. He stood by me when I needed support and drew a hard line when I became distracted and lost focus. Few students are lucky to have mentors, like Bob, who bother to take a vested interest in their student's professional and personal well-being. I'm forever in his debt for the role he's played in my development as a scientist and as a person.

Along with Bob, my time has been spent with Andrea, Ernie, Phil, Max, Sasha and Marc. Each has shared with me their experiences and has helped me determine my own scientific vision and professional direction. A couple pages in a dissertation are unable to do justice to the gratitude I owe each of these gentlemen, nor fully depict the heated discussions, unabated laughter and unforgettable memories we've shared over the last few years. At the risk of oversimplification, I would like to thank Andrea for his enthusiasm, drive and plates of *spaghetti*; Ernie for his maverick sensibilities, humor and the 5.3.1 donkey; Phil for his calm and grounded perspective; Max for his creativity, frankness and *Pornoscience*; Sasha for his fearlessness; and Marc for unicycles, licorice and attention to detail. As my time as a student draws to a close, I would be remiss not to acknowledge the indelible influence each of these guys has had on me. As a matter course, I must also acknowledge the staff and financial support of the Advanced Light Source during my tenure.

I also greatly appreciate the faculty members who have taken time from their busy schedules to serve on my academic committees and to counsel me. I would like to thank my faculty advisor, Chuck, for lending me his perspective as Lab Director and showing me how science on a large-scale is managed. I would also like to thank Graham for his genteel wisdom and warmth; Daniel for his quiet intensity and timely advice; Daryl for his brutal honesty and acerbic wit; Roger for his scientific perspective and affability; and Dave for his support and sharing his sandwich and beverage with me when I visited as a prospective student.

I would especially like to thank Pat for making life easy for me as a student in the University of California, Berkeley system. For all the horrors and frustrations students on a large campus face, Pat has, without fail, been a warm and welcoming interface to the chaos that lurks beneath. She has created a comfortable environment for me since the day arrived at her office as a panic-stricken applicant with missing documents. Thanks, Pat.

There are also a number of people who have help me acclimate to the unique and, frankly, bizarre community of Berkeley and broader Bay Area. Thank you Oscar and Sanjay for supporting me through the most difficult times of my life. I will forever carry with me the memories of buffets, Foreman grills and long afternoon naps through J. Lo movies—I won't mention *The Exorcist*. Thank you Jamie, Bridget, Lara, Brian, Wade and Bobbie for providing a sense of wholeness to my life outside of work. Thank you, New Church.

Thank you Mom, Dad and Aimee for always supporting me regardless of the choices I've made in my life. Thank you, Renai, for always being there.

To Berkeley, I bid a fond farewell. For all its contradictions, idiosyncrasies, veiled intolerance and inevitable *Twilight Zone* happenings, I have learned to embrace its diversity of thought, opportunities and acceptance of those who have chosen to take the path less taken. This is truly a special community, and I feel fortunate to have been part of it...can you get a Wal-Mart already?

1 AN INTRODUCTION, CONTEXT AND MOTIVATION

1.1 Why: Atoms Sit Still for No One.

Modern advances in science and technology have involved designing and implementing systems that approach the limits of physically relevant spatial and time scales. The information revolution heralded by pervasive and prolific developments in communications finds its roots in the scientific enterprise of generating ever-shorter pulses of radiation to probe fast, transient dynamics in chemical and condensed matter systems. Continued miniaturization of semiconductor systems have led to the rise of nanotechnology as a promising field of investigation, portending a wide spectrum of potential applications, with a natural endpoint being the engineering of materials and systems at atomic-scales to achieve desirable macroscopic properties.

As these two seemingly divergent scientific endeavors progress, they will inevitably meet. To fully utilize short-pulse radiation at all wavelengths will require the development of novel materials and material systems that can manipulate short (or equivalently broadband) pulses of electromagnetic radiation. Proper design and synthesis of materials, especially of optical or photonic materials (light being the information

transport vehicle of choice), requires knowledge of how the many degrees of freedom in a material interact and give rise to exotic, macroscopic properties. Complete characterization of a material demands a means to resolve atomic re-arrangement in a material on the time-scale that the atoms move.

A particularly illustrative example of this problem is the accurate prediction of electronic properties of solid-state systems. There exists an age-old arsenal of tools to calculate energy-levels and band structures for systems, given static atomic configurations. These robust methods can even account for perturbative, harmonic structural modes in the system. However, when electronic dynamics are tied to gross atomic re-arrangement, potentially forcing non-adiabatic transitions, these methods fail. A dynamic distortion of the electronic potential energy surface makes the calculation of even simple electronic properties intractable. For systems where the electronic structure is intimately tied to atomic re-arrangement, accurate prediction of electronic properties still remains a work in progress, and requires new information regarding the dynamics of structural re-arrangement to proceed.

1.2 How: Ultrafast Meets X-Rays.

One approach to measuring atomic rearrangement on the shortest relevant time scales of atomic motion is the application of ultrashort¹ x-ray pulses in a stroboscopic spectroscopy. X-rays are the natural probe for direct determination of atomic location; atomic scale structural determination has long been the purview of x-ray spectroscopy. At issue is energy scale: x-rays interact with core-shell electrons, which are tightly bound to the atomic nucleus, and generally do not participate in bonding, as shown in Figure 1.1. Probing a core-shell electron reveals information local to the environment of its nucleus.

¹The term “ultrashort” has been defined on a sliding scale of magnitude since the initial development of short-pulse radiation sources many decades ago. Colloquially, the term refers to the shortest pulse durations which can be generated by most research groups with reasonable ease. At this moment in scientific history, it refers to pulse durations on the order of one-hundred femtoseconds (fs, 10^{-15} s) or less, certainly less than a picosecond (ps, 10^{-12} s).

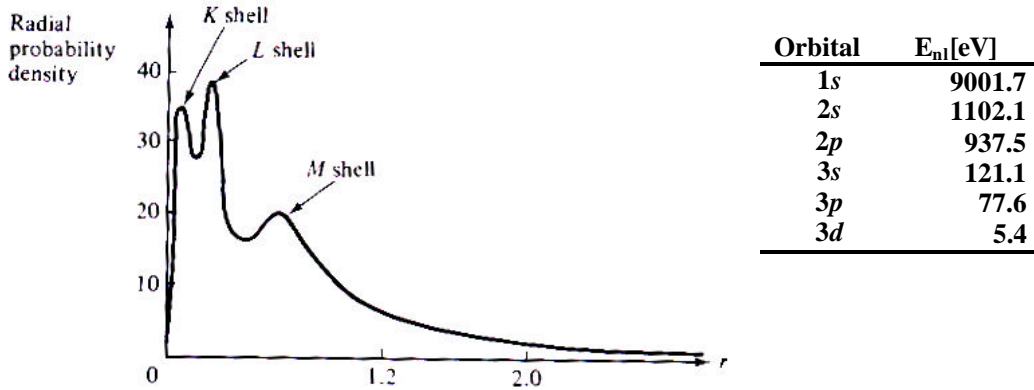


Figure 1.1: Calculated radial electron distribution and binding energies for Cu^+ under the Hartree approximation, taken from [Mor91]. Peaks order by principal shell: K ($n=1$), L ($n=2$), M ($n=3$), etc. Of note: the radial distribution center of mass for $l \neq 0$ sub-shells is actually closer to the nucleus than the $l = 0$ sub-shell. The $l = 0$ sub-shell, however possesses a higher binding energy as it screens the $l \neq 0$ sub-shells.

To achieve the necessary time-resolution requires the application of pulses as short or shorter in duration than the time scales of interest in a stroboscopic spectroscopy. Stroboscopic spectroscopy is simple. As illustrated in Figure 1.2, time-resolved measurements can be made on a system by initiating dynamics with an impulsive excitation and following the impulsive excitation at a specific time-delay with an impulsive, perturbative probe to ascertain the state of the system at that point in time after excitation. By varying the time-delay, the evolution of the system following excitation can be mapped out as a function of time, essentially producing a flipbook of the system as it evolves after excitation.

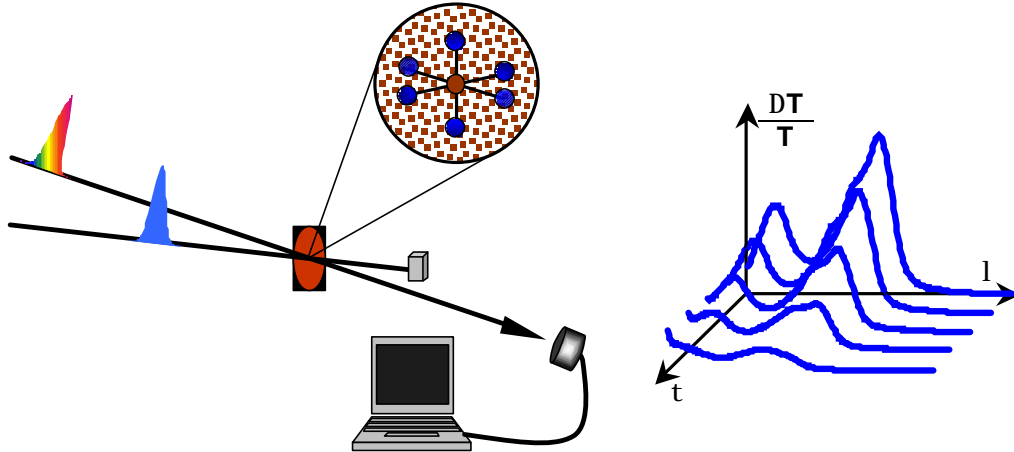


Figure 1.2: Experimental set up and time-resolved spectra derived from pump-probe spectroscopy. A simple static probe provides absorption spectra. Probing at a series of delays after excitation provides a series of absorption spectra which depict the evolution of the system after excitation.

For perturbative excitations, this is equivalent to extracting the impulse response (or the system function) of the system, in the terminology of linear time-invariant systems. For intense excitation, what is probed is the non-equilibrium linear response of the system. The purpose of stroboscopic spectroscopy, however, is not to simply measure the macroscopic response of the system, but to understand the microscopic dynamics that underlie the response. Excitation dynamics in condensed matter systems generally reflect complex couplings between the structural, electronic and magnetic degrees of freedom. However, these excitations and couplings have natural time and energy scales. If appropriate probes of these excitations can be performed with adequately fine time-resolution, it becomes possible to unravel the role each degree of freedom plays in the behavior of the system. In this way, a physical system can be fully characterized and reasonable models to describe their excitation dynamics can be constructed.

Ultrafast x-ray spectroscopy is an emergent field of science borne of the need to determine atomic re-arrangement on the ultrafast time scale. The scope of ultrafast x-ray spectroscopy is to develop ultrashort x-ray pulse sources, techniques and detectors to perform time-resolved measurements with atomic-scale spatial resolution and ultrafast time resolution. It is the confluence of two mature fields of science, x-ray spectroscopy

and ultrafast optical spectroscopy, and represents a *fundamental* experimental advancement in the study of dynamics in condensed matter and chemical systems.

Clearly, the capability to track atomic re-arrangement has great appeal for the scientific community in general. A myriad of long-asked questions can now be addressed. Fast, transient structural dynamics and phase transitions in materials can be studied. Complex interactions between electronic, magnetic and structural degrees of freedom in a material can be unraveled: the role played by structural dynamics in the mechanism for high- T_c superconduction, for example, can be investigated. Conformational pathways followed by photo-active proteins can be mapped. Complex photochemical reactions can be fully characterized. As experimental techniques and capabilities continue to evolve and mature, ultrafast x-ray spectroscopy will become less a nascent field of study, and more a standard spectroscopic tool.

Ultrafast x-ray spectroscopy greatly enhances the spectroscopist's toolbox. With the realization of ultrashort x-ray pulse sources, ultrashort pulse radiation can now be generated across the entire electromagnetic spectrum. This allows for condensed matter systems to be excited and probed at almost all relevant energy and length scales with time resolution necessary for a complete characterization of excitation dynamics.

1.3 Overview

Section 1: An Introduction, Context and Motivation

Ultrafast x-ray spectroscopy presses the physically relevant limits of measurement in condensed-matter and chemical systems. It is of fundamental importance. Ultrashort x-ray pulses complete the spectral complement of ultrashort pulse electromagnetic radiation, extending from the far-infrared to hard x-rays, needed to fully characterize excitation dynamics in chemical, biological and other complex systems and materials.

Section 2: Tools

Development of a new spectroscopy requires the design and implementation of useful sources and appropriate techniques with their associated detectors. A criteria for useful sources, techniques and detectors is outlined and presented against a backdrop of past practice. An argument for the future development of ultrashort x-ray sources is made based on the success of present-day, state-of-the-art continuous wave (cw) x-ray user facilities.

Section 3: Ultrashort X-Ray Pulses at the Advanced Light Source

The first-generation ultrashort x-ray pulse facility at the Advanced Light Source (ALS) at Lawrence Berkeley National Laboratory (LBNL) is discussed. The physical principles underlying electron slicing ala Zholents and Zoloterev are discussed in detail. Results are presented against model calculations.

Section 4: Time-Resolved Studies of Transition Metal Complexes

An iron-based transition metal complex which displays an intersystem crossing (spin-crossover) concomitant with structural distortions upon photo-excitation on an ultrafast time-scale is studied. An overview of this behavior is presented along with results from optical spectroscopy to describe the roles of electronic, spin and steric degrees of freedom in the transition.

Section 5: Considerations for Future Work

Ultrafast x-ray spectroscopy used in concert with other time-resolved methods is a promising means of studying strongly interacting systems, as these complex systems (e.g., material, chemical, biological) often have function (e.g., protein conformational pathways), which follow from structural dynamics. Experiments in this spirit are proposed for future incarnations of machine-based ultrashort-pulse x-ray sources. In the near-term, a number of technical hurdles need to be overcome due to the unique nature of this spectroscopic technique. These issues are discussed along with potential solutions.

2 TOOLS

As with most fields of experimental science, ultrafast x-ray spectroscopy is a field driven by inquiry and, only recently, enabled by technology. The continued development of this enabling technology must be guided by the demands of scientifically interesting investigation and lessons learned from prior art. This chapter is separated into two distinct halves: sources and experimental considerations. The first half provides a brief overview of current and past ultrashort pulse x-ray sources with advantages and limitations for each. General considerations for current efforts in source development are outlined with benchmarks assessed from needs of more demanding experiments. In the second half, empirically derived considerations for development in detector technology are described in the context of various spectroscopic techniques, which are desirable for time-resolved studies with ultrashort x-ray pulses.

2.1 Sources

2.1.1 History and the State-of-the-Art

Over the past decade, much effort has been made in the construction of ultrashort pulse x-ray sources with modest results. These sources fall into two main divisions: table-top sources based on laser-generated plasmas [RRG01] and user-facility scale sources based on free-electrons in machines [SLC⁺96,SCC⁺01]. Each means of generation has its

benefits, and lessons learned from each provide meaningful guidance for the future development of spectroscopic sources for general use by the scientific community.

Laser-Generated Plasma Sources

Laser-generated plasma-based ultrashort pulse x-ray sources are based on plasmas created when high-intensity laser pulses impinge upon an elemental solid-state target. K_a radiation and a spectral background of *bremsstrahlung* are generated from the fast electrons driven into the material through the duration of the laser pulse. Due to the nature of the x-ray generation, these are essentially line-sources with a $4p$ divergence and require toroidally bent crystals for efficient collection. The monochromaticity and spatial divergence of the beam make these sources well-suited for diffraction studies (the entire rocking curve can be simultaneously measured due to the beam divergence) that provide information regarding dynamics in the long-range order of material systems [S-T⁺03, RRF⁺01].

Laser-generated plasma sources are, by nature, table-top scale sources. As laser technology has matured, high-pulse energy ultrashort-pulse laser systems with moderate repetition rates have become more easily realizable, and will allow plasma-based systems to be scaled to higher average flux levels. Synchronization between the generated x-ray probe and optical pump pulse is absolute², since excitation pulses can be easily derived from the laser system used to generate the x-rays. Specialized x-ray collection optics [RRU⁺97], however are required, and the tunability and useful spectral bandwidth of the source is relegated to the K_a lines of different elements, making it difficult to perform compelling absorption measurements to determine local atomic re-organization in material and chemical systems.

Thomson Scattering Sources

The Thomson scattering source developed at the ALS is the first demonstrated generation of tunable femtosecond x-ray pulses from free-electrons interacting with ultrashort laser pulses [Chi98]. An ultrashort, intense laser pulse collides with a relativistic electron-

² Synchronization is absolute up to mechanical fluctuations and drift in excitation and probe pulse paths.

beam in a 90° geometry as illustrated in Figure 2.1. The laser pulse acts as an optical wiggler, forcing the electrons to undergo oscillatory motion, generating x-rays in the forward direction of electron propagation. The pulse length of the x-ray pulse is limited by the laser-electron interaction time (i.e., the electrons only oscillate, and hence radiate, when in the laser field). To obtain the shortest possible x-ray pulses, the transit time of the laser pulse through the electron bunch is minimized first by focusing both beams, and then colliding them in a 90° geometry. Absolute synchronization of x-rays is possible for this system, since an optical pump pulse can be easily derived from the same laser system that used to generate x-rays.

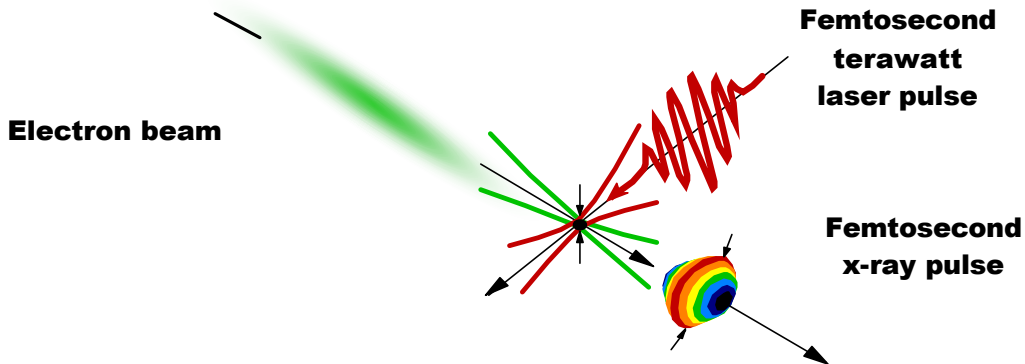


Figure 2.1: Interaction geometry of the Thomson scattering source realized at the ALS. An electron beam and terawatt laser pulse are focused and crossed at 90° at the interaction point. Ultrashort pulses of x-rays are generated in the forward direction of the electrons. Illustration is courtesy of R.W. Schoenlein.

The nature of the x-ray radiation, however, is polychromatic due to the fact that individual electrons follow different trajectories through the focus, smearing the monochromaticity predicted in a single-electron picture. This source, like the plasma source, was used for diffraction studies [CSG⁺99]. Central x-ray wavelength tunability is achieved by tuning free-electron energy. The flux demonstrated with the source constructed at the Beam Test Facility of the ALS is rather low; improvements can be made as the flux scales linearly with the number of laser photons and the number of electrons used in the interaction. Laser development is required to increase average laser

power (most likely via repetition rate) for such a system. Improvements in electron beam properties will enhance the source flux and monochromaticity through the development of cathodes and linear accelerators. But, even with great technological enhancement, the relative x-ray photon yield of these sources is marginally useful for experiments. This approach, however, appears to be the quickest route to the generation of ultrashort pulses of extremely high-energy photons (\sim MeV).

Electron Slicing in Storage Rings

The development and demonstration of a slicing source constitutes the bulk of this thesis and is elaborated upon in Chapter Three. In brief, electron slicing is the generation of ultrashort slices of electrons from electron bunches of standard length that circulate in the storage ring of a synchrotron. The success of third-generation synchrotrons suggests a machine-based approach to ultrashort x-ray pulse generation is most promising. Synchrotrons are capable of generating high-brightness, high-flux x-ray beams throughout the entire x-ray spectrum, and can manipulate x-ray polarization and coherence to provide interesting experimental modalities for a wide-range of experiments and applications. Synchrotron radiation has motivated great advancements in static x-ray spectroscopy over the past two decades [DOE97].

The concept of electron slicing is simple. A laser pulse modulates the energy in a short slice of the electron bunch. In a dispersive section of the storage ring, the energy-modulated slice spatially separates from the main bunch. Now, the same radiating structures, transport optics and other mature technologies employed at these facilities can be used with ultrashort electron slices to generate synchrotron radiation with ultrafast time-structure that are absolutely synchronized to laser excitation pulses for pump-probe style experiments.

2.1.2 Requirements for the Ideal Ultrashort X-ray Pulse Source

The requirements for useful ultrafast x-ray sources can be gleaned from the demands of modern ultrafast optical spectroscopy and static x-ray spectroscopy. The demands of ultrafast optical experiments set the technical requirements for the level of precision

required to perform time-resolved measurements with fine time resolution. Science performed at third-generation synchrotrons set the requirements for x-ray probe characteristics.

Tunability and Broadband Capabilities

The ability to tune radiation across reasonably wide bands of the electromagnetic spectrum has greatly benefited time-resolved spectroscopy. Optical parametric amplifiers [CNS⁺98] for ultrashort pulse lasers allow researchers to tune their sources to excite and probe specific transitions in their system under study. The great success demonstrated at third generation synchrotrons, like the ALS, suggest that with x-ray spectroscopy, wavelength tunability is even more important. Due to the relatively wide spread between the absorption edges of chemically neighboring elements, it is possible to target and probe the local environment of specific atoms in a material system for absorption studies, providing not only chemical specificity, but also spatial localization for the probe.

A current problem under investigation at ALS beamline 5.3.1 benefits from wide spectral tunability. To understand the nature of the metal-to-insulator transition of vanadium dioxide (VO₂) brings into question both the gross structural changes [CTS⁺01] and re-organization of the electronic structure tied to the structural change upon photo-excitation [AdG⁺91]. Detailed study of this material requires probes at two very different spectral locations. To study local structural re-organization about the vanadium metal centers it is preferable to measure changes in the EXAFS following the vanadium K-edge at 5.5kV. Looking at the K-edge EXAFS not only gives probe localization closest to the vanadium, but also provides an observation void of potentially complicating electronic effects. At the vanadium L-edge (520eV), re-organization of the electronic density of states can be observed and deciphered with the appropriate modeling³. Looking at these two edges allows information regarding electronic structure and local atomic order to be separately observed using the same experimental modality, providing consistency in

³ Calculations will involve an *ansatz* for electronic and atomic structure fed into x-ray absorption simulation codes such as FEFF[®]. For molecular systems, quantum chemistry codes such as Gaussian98[®] or Jaguar[®] can be employed to anticipate electronic and structural parameters.

explaining the time-evolution of the physical processes that underlie the metal-to-insulator transition.

Broadband capabilities provide an added convenience and the potential for exploratory study. Broadband x-ray radiation allows for simultaneous measurement of entire absorption spectra or complete Laue diffraction patterns. The collection of data is vastly expedited when multiple channels are available for simultaneous detection, as opposed to individually stepping through x-ray wavelengths. Having the possibility of a broadband beam can only be a benefit. The option always exists to monochromate a white beam with crystals or gratings or to shape a pink beam using multilayer mirrors or thin film filters to address potential technical issues that may arise due to excessive photon flux.

Photon Flux

Spectroscopic measurements are generally made on perturbative effects in systems. In demanding experiments, averaging is required to generate reasonable statistics (or signal-to-noise) to observe the processes of interest. In order to observe effects with a reasonable signal-to-noise in reasonable acquisition times, minimum demands for total flux must be met. Table 2.1 lists two experimental systems of interest in their flux requirements.

Experimental System	CdSe nanocrystals in C ₈ H ₁₆	[Fe(py ₃ tren)]Cl ₂ in H ₂ O
M (moles/liter)	0.1	0.26
X-ray absorption edge	Cd (L _{edge}) 3.54 keV	Fe (K _{edge}) 7.11 keV
Signal: $\Delta\sigma_{\text{x-ray}}$ ($\times 10^{-19}$ cm ²)	1.6	0.33
Sample thickness (μm)	100	100
σ_{opt} ($\times 10^{-17}$ cm ²)	20 (at $h\nu \approx 2.5$ eV)	0.12 (at $h\nu \approx 2.7$ eV)
Pump Fluence ($\times 10^{17}$ ph/cm ²)	0.5	4.3
X-ray photons required (SNR=10)	2.8×10^6	8.7×10^5

Table 2.1: Parameters and expectations for optical-pump/x-ray probe experiments.

As with ultrafast optical spectroscopy, the per-pulse x-ray flux is upper-bounded by the need to maintain a perturbative probe and lower-bounded by experimental requirements for an acceptable signal-to-noise level. Using higher repetition rates to achieve more reasonable acquisition times also requires some consideration. The upper-bound for repetition rates is dictated by the recovery rate of the physical system being excited. Systems of interest tend to interconvert a great deal of excitation energy into structural deformations that decay through pathways that ultimately manifest in heat. Average heating by the excitation pulse (or the probe pulse) may induce unwanted artifacts in the measurement or, even worse, degrade or destroy the sample, as shown in Figure 2.2.

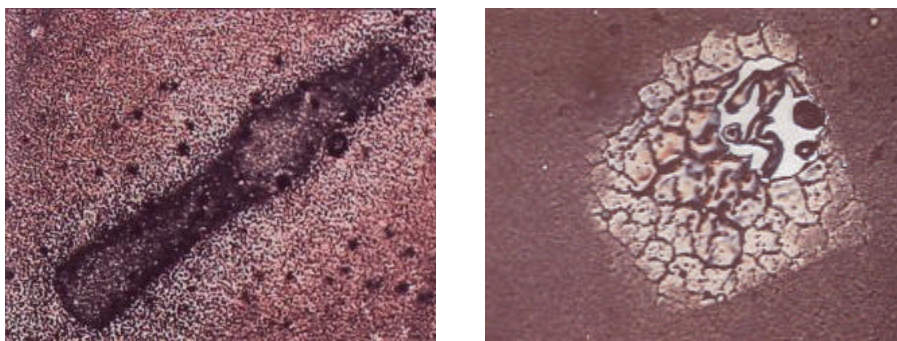


Figure 2.2: Samples scarred due to x-ray damage and an inability to dissipate a high average thermal load. The image to the left is $\text{Fe}[\text{tren}(\text{py})_3]\text{Cl}_2$ on a $10\mu\text{m}$ thick beryllium foil damaged by x-rays. The image to the right is $\text{Fe}[\text{tren}(\text{py})_3]\text{Cl}_2$ on a $0.2\mu\text{m}$ thick silicon nitride window damaged by an inability to dissipate local thermal laser heating.

For machine-based sources, the incident x-ray power needs to be matched to the data acquisition rate for the experiment. Excessive x-ray flux on the sample may unnecessarily expedite the deterioration of the sample. For systems with a wide mismatch between x-ray repetition rate and data acquisition rate, the average power of the x-rays can be mechanical chopped to alter the effective duty-cycle of the source. A beautiful example of using a chopper to single out a particular pulse from a storage ring is the implementation of the Jericho chopper at ESRF ID9⁴.

⁴ http://www.esrf.fr/exp_facilities/ID9/id9.html

Pump-Probe Synchronization

The fine time resolution afforded by spectroscopy using ultrashort pulses of radiation is due not only to the impulsive nature of the radiation, but also from the fact that there is almost no jitter between the pump pulse and the probe pulse. Any jitter between the time when the system is excited and the time when the system is probed yields an ambiguity in the precise timing of the observed properties of the system when the measurement is averaged over many shots. For example, a system with 10fs pulses and jitter of 50fs between the pump and probe cannot resolve features in the evolutionary signature of the system below the 50fs limit imposed by the jitter as illustrated in Figure 2.3.

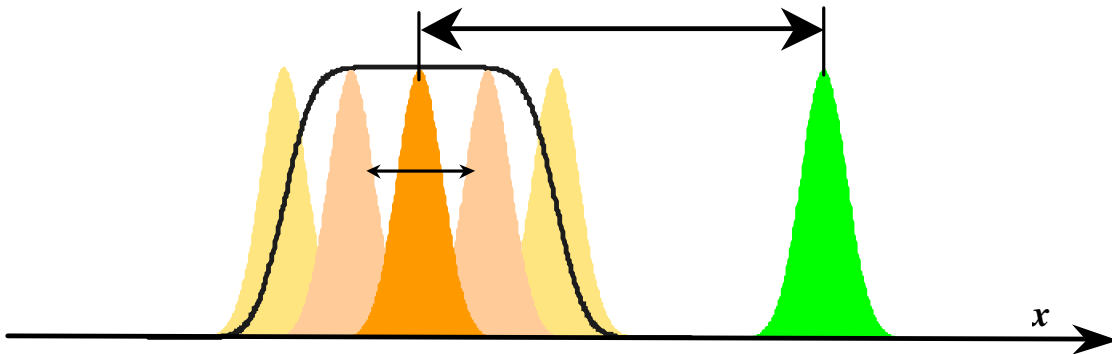


Figure 2.3: The thick curve is the effective envelope of the probe pulse. Jitter in the synchronization of the probe pulse referenced to the excitation pulse effectively smears the time-resolution of the measurement due to the uncertainty in delay following excitation.

Jitter between pump and probe pulses can be minimized. In optical time-resolved spectroscopy, pump and probe pulses are derived from same source (i.e., via beamsplitting), thereby creating an absolute synchronization between the two. Absolute synchronization is corrupted only by fluctuations due to instability of transport optics. For optical pump and x-ray probe systems, this absolute synchronization is achievable if the x-ray generation is tied to a laser system, such as in plasma sources or systems based on laser-electron interactions. For free-running systems, feedback can be employed to lock the two systems to each other to minimize jitter [RBW89].

Wish List

Having outlined the desirable properties for an ultrashort x-ray pulse source with obligatory rationale and context, it seems natural to condense and compile those desires along with other considerations for the sake of record and easy retrieval: Table 2.2.

Source Properties

Number of photons per pulse	$\geq 5 \times 10^4$
Repetition rate	Variable, 10Hz-100MHz
Tunability range	10eV-20keV
Maximum resolving power	10^4
Maximum source bandwidth	1keV
Pulse duration	≤ 100 fs
Synchronization	≤ 10 fs jitter
Pulse contrast	200:1, on negligible absolute background

Table 2.2: Desired ultrashort pulse x-ray source properties.

2.1.3 Looking Forward

In the foreseeable future, a number of machine-based ultrashort pulse x-ray facilities will commence construction or complete commissioning. Within the decade the Ultrafast X-ray Science Facility (UXS) at the ALS will become operational. UXS will be a high-end facility based on an electron slicing source. The source will provide the photon flux necessary for even moderately demanding spectroscopic experiments in the hard and soft x-ray regime. It will also serve as a useful test facility for the continued development of technologies and experimental apparatuses for 4th generation x-ray facilities designed specifically for the generation of ultrashort x-ray pulses.

In the long term, hard x-ray free electron lasers (FEL) based on the principle of spontaneously amplified self-emission (SASE) such as the Linear Coherent Light Source⁵ (LCLS) in the United States and Tera-electron-volt Energy Superconducting Linear

⁵ <http://www-ssrl.slac.stanford.edu/lcls/>

Accelerator⁶ (TESLA) in Germany hope to provide intense, ultrashort x-ray pulses for characterization of systems under high-energy density conditions and for the development of novel techniques for atomic structure determination. Recirculating linear accelerator (LINAC) sources are also being planned. The Linac-based Ultrafast X-ray Source⁷ (LUX) at Lawrence Berkeley Laboratory and the Energy Recovery Linac⁸ (ERL) at Cornell University are designed to be ideal x-ray spectroscopy sources for time-resolved studies on the ~100fs scale, with high-repetition rates and moderate per-pulse x-ray flux.

2.2 Spectroscopic Techniques and Detection Schemes

2.2.1 Techniques

The same techniques used in static x-ray spectroscopy to determine local and long-range structural order, electronic structure and magnetic properties of material and chemical systems can all be adapted to a time-resolved measurement. The choice of spectroscopic technique hinges on the nature of the problem and the properties to be measured or effects to be observed.

The two main approaches to x-ray spectroscopy address atomic order on long- and short length scales. Diffraction techniques require coherent scattering from many ordered scatterers within a material system and thereby probe the long-range order of system under study. Absorption techniques measure absorption spectra with contain features that are indicative of local coordination, bonding geometry and electronic structure due to the influence of neighboring atoms.

X-Ray Diffraction

Diffraction has long been a stalwart tool to characterize ordered materials ranging from mundane metals [Bar62] to proteins [V-S⁺03] to nano-structures [RVW⁺01] to quasi-periodic crystals [RTH⁺00]. Diffraction is implemented in a myriad of ways (Bragg, Laue, rotating-crystal, powder [War69]), but follows from a very simple physical

⁶ <http://www-hasylab.desy.de/facility/fel/xray/xfel-lab.htm>

⁷ <http://www.als.lbl.gov/als/20/LUXtext.html>

⁸ <http://erl.chess.cornell.edu/>

process: constructive scattering of x-rays from periodic scatterers in the crystal system under study. The diffracted radiation pattern that results is the Fourier transform of the scattering sites.

Using kinematic considerations, diffraction is simply a selection rule for the k -vector of the incident radiation [Kit53] for a given set of lattice planes given by equation 2.1,

$$(\bar{k} + \bar{G})^2 = k^2 \quad (2.1),$$

where k is the wave vector of the incident radiation (i.e., propagation vector of magnitude $2\pi/\lambda$) and G is the vector defining the lattice planes (oriented normal to the planes).

Put simply, selection by a lattice plane implies the existence of diffraction spot; since selection is possible by variation of radiation wavelength (via magnitude of k) or angle of incidence relative to the normal of the lattice planes (k is a vector), various means can be employed to fully sample the crystalline structure of the system. Commonly used methods in modern diffraction facilities employ collimated, broadband x-rays (Laue) or vary the orientation of the system under study to fully sample a crystalline structure (powder—randomly oriented many copies of the crystal, rotating sample—physically rotating a single crystal).

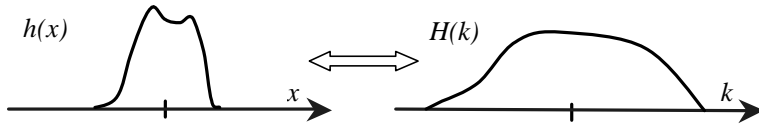
The intensity of a given spot is determined by the geometrical structure factor, which accounts for the phases of the scatterers weighted by the scattering strength of each individual scatterer (atomic scattering factor). A fuller description of x-ray diffraction processes are described by dynamical diffraction theory [BC64] which accounts for additional physical processes involved in x-ray-matter interactions.

A time-resolved diffraction experiment will measure a shift in the position of a diffraction spot, a change in spot intensity or the broadening of a spot. These observed changes in the diffraction pattern can be related to the behavior of the scatterers through their Fourier transform relationship. *Motion of spots suggests change in crystalline*

structure (i.e., a crystallographic phase transition). *Changes in spot intensity correspond to a distortion within unit cell* (a change in relative phase between scatterers).

An one-dimensional analysis of a periodic function and its Fourier transform will make these claims

clear. A basis function and its Fourier



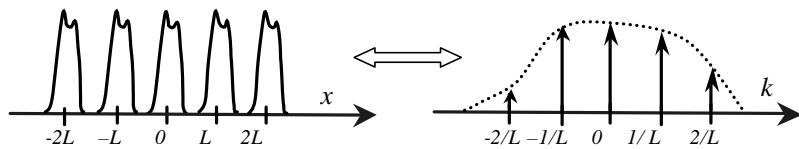
transform represent a unit cell. Lattice periodicity is established by convolving the unit cell with an impulse train of period L . The result is a one-dimensional lattice comprised of a unit cell replicated with period L .



A Fourier transform of the one-dimensional lattice will generate its diffraction pattern.

The Fourier transform of an impulse train of period L is, again, an impulse train of spacing $1/L$. Since convolution in real space is multiplication in Fourier space, the Fourier transform of the one-dimensional lattice becomes an impulse train of spacing $1/L$ with an amplitude

envelope that is the Fourier transform of the unit cell.



Using the properties of Fourier transforms, changes in the diffraction pattern can now be easily related to spatial changes in the atomic scatterers. In the diffraction pattern, the position of the impulses corresponds to the position of the diffraction spots. If the position of the spots is altered, the periodicity of unit cells has changed (the movement is inversely proportional to the change of the spots, in fact). So, in the case of a purely crystallographic phase transition, spot are expected to shift positions. In the case of

atomic re-arrangement confined within the unit cell, the amplitude envelope of the diffraction pattern changes, altering the intensity of a spot. Physically, this corresponds to a change in the phase relationship between the atomic scatterers; the diffracted spot intensity changes as the level of constructive interference changes. Most structural changes will reflect both motion of a spot and a change in its intensity [P~~S~~R⁺98, TSW01], and even broadening of spots due to a reduction in order (i.e., an increase in variation of lattice plane spacing from the mean).

X-Ray Absorption

X-ray absorption spectroscopy is a technique used to access local structural order, electronic structure and magnetic order in ordered (crystals) and non-ordered (amorphous solids, liquids, gases, etc.) material and chemical systems. The ability to tune the x-ray wavelength to a specific atomic K- or L-edge permits the chemical/site specific probing of a sample to determine dynamics specific to a particular location in the sample.

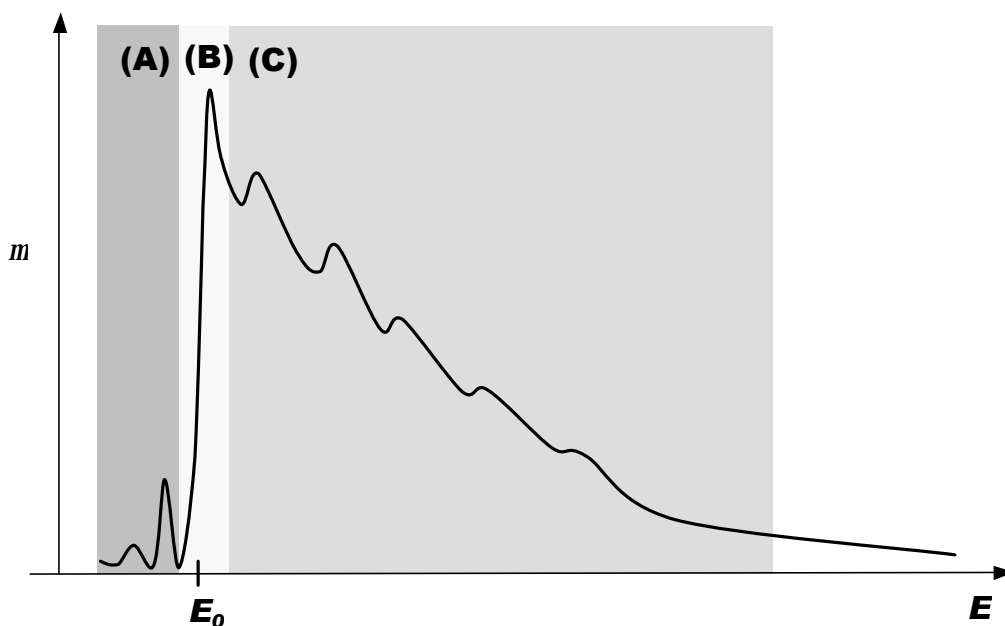
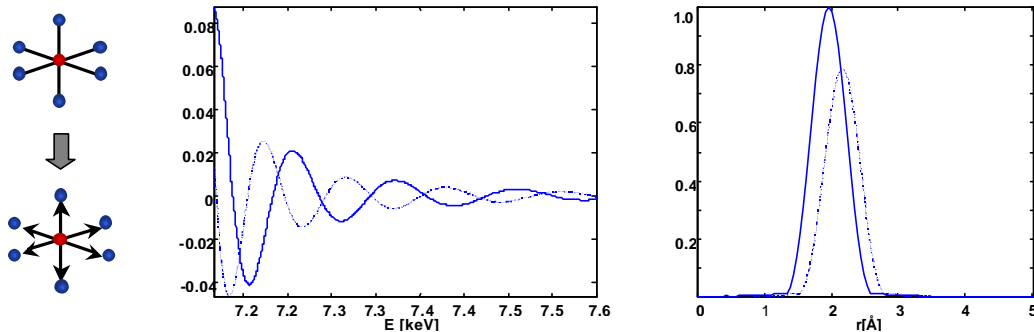


Figure 2.4: A generic x-ray absorption spectra dissected to illustrate three distinct regions. Coded in three shades of gray are (A) pre-edge, (B) edge and (C) EXAFS features.

The major features of interest in a generic x-ray absorption spectrum are illustrated in Figure 2.4, and include the spectral region before the absorption edge, the edge itself, and

the extended x-ray absorption fine structure (EXAFS) that proceeds from the edge toward the high-energy side of the spectrum. The position and intensity of these features are sensitive indicators of the local environment of the target atom, and with proper interpretation, can yield a great deal of information regarding the local atomic coordination (bond distances and bond angles) and electronic structure of the sample under study.

The most straightforward region of the absorption spectrum to interpret is the EXAFS region. EXAFS provides a sense of local coordination of target atom. In fact, as is evident from equation (2.2), with appropriate normalization and calibration, the Fourier transform of the EXAFS wiggles gives the two-point correlation function of the probed atom [Teo86]. In time-resolved measurements, changes in local coordination of the target atom will be reflected in evolutionary changes in the fine structure modulation phase and intensity as depicted in Figure 2.5.



$$c(k) = \sum_{\text{neighbors}} \frac{F_i(k) \cdot \exp\left\{\frac{-2r_i}{l}\right\} \cdot \exp\left\{-2k^2 S^2\right\} \cdot \sin\left(2kr_i + \mathbf{f}_{\text{central}}(k) + \mathbf{f}_{\text{back},i}(k)\right)}{kr_i^2} \quad (2.2)$$

Figure 2.5: Changes in K-edge EXAFS due to bond dilation calculated for a six-coordinate iron-based transition metal complex with a first-ordination shell of nitrogen atoms. The modulations pictured in the left panel are calculated for the EXAFS alone, without any residual absorption background. A Fourier transform of the modulations in the right panel gives the atomic positions.

The EXAFS features in the absorption spectrum manifest due to very simple physical process. As illustrated in Figure 2.6, a core electron liberated by an x-ray photon will

have a spherical wavefunction. This electronic wavefunction scatters from neighboring atoms and constructively and destructively interferes with the original, outgoing wave. This interference manifests in the absorption spectrum as EXAFS, wiggles to the high energy side of the absorption edge (the electron must become unbound), corresponding to the relative permissibility of the transition (since certain electron k-vectors are coherently disallowed). The underlying assumptions used in interpreting EXAFS modulations are

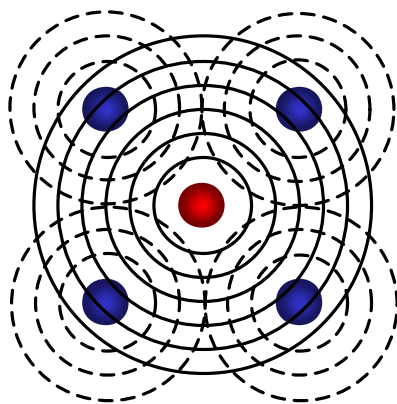


Figure 2.6: An outgoing core electron freed by an x-ray photon (solid-line wavefronts) scatters from neighboring atoms (dashed-line wavefronts) and produces interference in the absorption spectra.

the spherical wave nature of the outgoing and scattered (i.e., the scatterers are point-like) electronic wavefunction and single-scattering events alone account for the observed phenomena (i.e., multiple scattering events do not contribute significantly).

Pre-edge and edge features of a system's x-ray spectrum are much more complicated to interpret [Sto92] due to the many processes which could potentially contribute to their appearance. Time-resolved measurements to observe chemical shifts in the absorption edge and the appearance (or disappearance) of intensity in pre-edges can be performed to determine the time-scale of the processes that manifest in these features. With involved simulation and complementary information, these features can yield information not only related to the atomic structure of the system, but also information regarding the electronic structure of system. Unfortunately, a considerable amount of information and detailed

simulation are required to make scientifically rigorous statements drawn for pre-edge and edge data concerning complex systems.

With the development of elliptically-polarized undulators (EPUs), circularly polarized x-rays can be incorporated to perform magnetically sensitive dichroism studies[FFY⁺02]. Application of different measurement modalities like photo-electron emission and fluorescence can also provide enhanced sensitivity (i.e., surface-sensitive techniques better match the probe depth to the excitation volume in the sample) and are referred to by specific measurement techniques: photo-electron emission spectroscopy (PES), angle-resolved photo-electron spectroscopy (ARPES), fluorescence-yield spectroscopy, etc. Unfortunately, photo-electron and fluorescence emission tend to be low-yield processes and require consideration to determine their utility and feasibility in time-resolved studies.

2.2.2 Detection

Detection systems for time-resolved x-ray measurements have the same sensitivity, efficiency and noise requirements as detection systems for signal-limited static x-ray measurements—as sensitive, efficient and noise-free as possible. Specific demands are made on detectors used in time-resolved measurements, however, due to the nature of the experiments and the character of the sources that will be available soon.

The general requirements for useful detection systems for time-resolved x-ray spectroscopy are

- **Fast time-response detectors:** Machine-based x-ray sources tend to generate x-ray pulses at high repetition rates. For example, the ALS generates 50-70ps pulses of x-rays every 2ns. If the duty cycle of the experiment is only a fraction of the 500MHz repetition rate, it is necessary to isolate individual ALS pulses. Slow-response detectors cannot recovery adequately, and simply smear the pulses together, providing a DC-level.
- **Fast gates:** Again, with unnecessarily high repetition rate, the ability to gate for the appropriate event is paramount. Fast gates can either be applied to the

detector itself, only allowing detection of desired events, or, if a fast-response detector is available, fast gates can be applied to isolate the resultant electronic signal of the desired event for analog integration or discrimination.

- **High-spatial resolution area detection:** The implementation of many spectroscopic techniques would benefit from area detection. For diffraction, a large region of the diffracted constellation could be observed simultaneously, and the nature of diffracted spot motion and broadening can be tracked more conveniently than with a point-detector. For absorption measurements, entire spectral regions can be measured simultaneously using broadband x-rays rather than incrementally stepping through x-ray wavelength with monochromatic beam or using a point detector in a dispersive scheme. In either case, high-spatial resolution detection translates into enhanced sensitivity to time-resolved changes.
- **Tractability in processing:** High-speed electronics will be necessary to digest, process and off-load the volumes of data generated in-parallel by area detectors to a central processing center. As this link in the data acquisition chain will most likely be a bottleneck, design should strive for data acquisition rates that match or exceed the source repetition rate.

Candidates for fast detectors include semiconductor-based detectors such as avalanche photodiodes (APDs), linear APD arrays and pixelated area APDs for direct detection of x-rays in transmission, reflection or other scattering (diffraction) experiments. APDs have high quantum efficiency with an active region that can be fabricated to match the penetration depth of a chosen x-ray wavelength. APDs are sensitive enough to observe individual photon events with reasonable response time (~5ns, perhaps can be fabricated to have even shorter response time). Other promising technologies include fast phosphors [DWK02] used in conjunction with gateable charge-coupled device (CCD) cameras.

Alternative detection modalities can measure other artifacts of the x-ray-matter interaction process. Rather than direct measurement of x-rays, sample fluorescence and photo-electrons emitted by the sample can also be observed. These detection modalities

have the promise of providing low or no background measurements in the proper experimental geometries as photo-excited regions of the sample will constitute a considerable fraction of the probe region. Unfortunately, photo-electron and fluorescence yield are not inherently unity conversion processes, and their benefit must be assessed on a case-by-case basis. Fast, gateable photo-electron detection systems have been demonstrated [Her⁺pp] at beamline 5.3.1 of the ALS.

3 ULTRASHORT X-RAY PULSES AT THE ADVANCED LIGHT SOURCE

Electron slicing ala Zholents and Zolotarev [ZZ96] is presented iteratively: first using pictures and simple concepts from electrodynamics to build an intuition for the nature of the laser-electron interaction employed, then followed by a formal discussion involving the necessary mathematical detail required to perform calculations to accurately predict the character of the generated femtosecond x-ray pulses. The specific implementation of the slicing technique at the Advanced Light Source is showcased with data characterizing the source.

3.1 Rudiments of Synchrotron Radiators

3.1.1 Bend Magnets

Synchrotron radiation is derived from relativistic electrons forced to undertake curved trajectories by magnetic fields⁹. Specifically, the electrons are either forced to turn a corner or forced to oscillate in the plane transverse to their direction of propagation. The time-structure of the resultant radiation is dictated by the time-structure of the radiating electron bunch. Due to electron-electron interactions within an electron bunch, a bunch

⁹An electron traveling at constant velocity will not emit radiation unless the radiation matches a particular mode allowed by a medium (e.g., Cerenkov radiation) [Hau86].

is inherently unstable when it is too short. To maintain a reasonable bunch lifetime at most synchrotron facilities, electrons usually propagate in bunches of ~ 10 ps in duration or longer. Electron slicing creates a short electron slice ~ 100 fs in duration from a long electron bunch circulating in the storage ring by generating an energy modulation on the long electron bunch, and using dispersion to translate this energy modulation into a spatial separation.

Bend magnets and insertion devices are the radiating structures used to generate x-rays at modern synchrotron facilities. They are also the tools used to generate electron slices. A bend magnet, illustrated in Figure 3.1, generates broadband radiation by forcing electrons to take a curved trajectory. Radiation generated from these devices span the infrared to hard x-ray regions of the electromagnetic spectrum. Bend magnets also serve as a means of introducing dispersion into the storage ring. Electrons with different energies (velocities) will take different trajectories through its magnetic field, spatial sorting electrons energy.

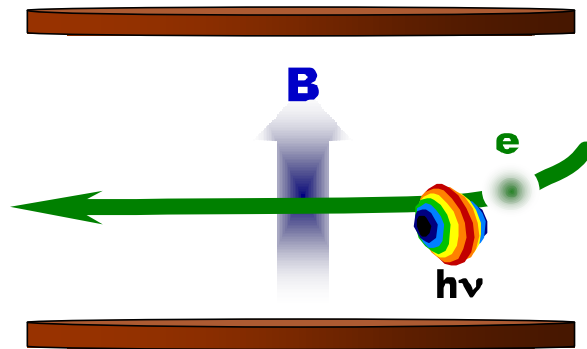


Figure 3.1: A bend magnet forces a relativistic electron to traverse a curved trajectory and emit radiation in a direction tangential to the curved path.

3.1.2 Insertion Devices

Insertion devices generate radiation by forcing relativistic electrons to take an oscillatory path by using alternating magnetic fields, as illustrated in Figure 3.2. Propagating electrons are transformed into traveling hertzian dipoles. Insertion devices operate in two

regimes referred to as the undulator and wiggler regimes. If the magnetic field strength in an insertion device is perturbative, the electron will take a simple, harmonic path through it. The radiation emitted due to the electron's many transverse excursions will interfere to yield nearly monochromatic and partially coherent light. These low-field strength insertion devices are called *undulators*. Above a certain magnetic field strength¹⁰ the trajectory taken is no longer a single harmonic, rather each transverse excursion possesses many harmonic components. As the electron encounters these strong magnetic fields, a significant fraction of its longitudinal velocity is transferred to a transverse component of velocity. The resultant radiation is incoherent and broadband, due to the spectral comb of harmonics that reflects the electron's trajectory. This *wiggler* radiation is akin to having the electron traverse consecutive bend magnets.

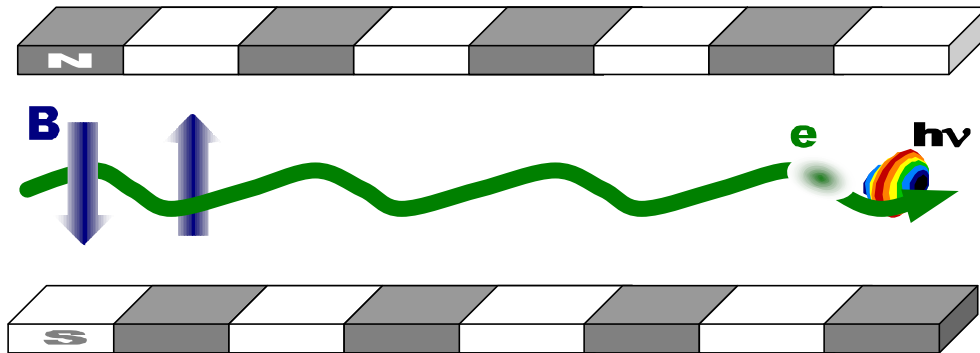


Figure 3.2: An insertion device is a periodic magnetic structure. Built with alternating magnets, the insertion device generates radiation by forcing a charged particle to wiggle or to undulate through it.

Electrons in insertion devices can be considered as traveling hertzian dipoles. Hertzian dipoles are considered canonical radiators, and are used to describe many processes where radiation from a spatially distributed source is considered, including x-ray diffraction and antennas [Kon90]. The radiation gain pattern for a stationary hertzian dipole has lobes in the plane containing the direction of oscillation. Looking down the axis of oscillation, the radiation pattern is axially symmetric and reminiscent of ripples in water, as illustrated in Figure 3.3.

¹⁰ Technically, the wiggler regime is when $B \gg \frac{2\pi mc}{e\lambda_w}$, where m is the mass of the electron, e is the electron charge, c is the speed of light and λ_w is the wiggler period.

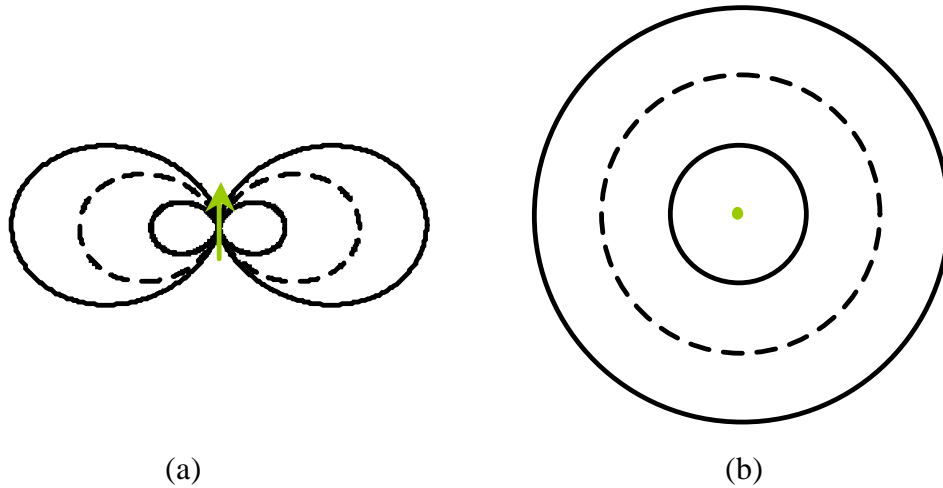


Figure 3.3: A hertzian dipole accurately models an electron traversing an insertion device. The gain pattern of a hertzian dipole is presented. Symmetry is broken in the plane containing the dipole, illustrated by the arrow in (a). Perpendicular to the dipole axis, the radiation pattern is symmetric, as in (b).

Intuitively, the nature of the radiation from an insertion device can be assessed from this picture. The frequency of the dipole oscillation gives the center frequency of the radiation, and the number of oscillations made by the electron sets the bandwidth of the emitted radiation. Taking the Fourier transform of the windowed oscillations gives the spectrum of the radiation as in Figure 3.4.

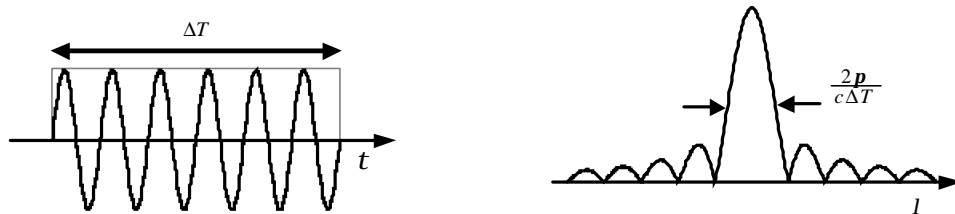


Figure 3.4: The on-axis spontaneous wiggler emission spectrum is the Fourier transform of the windowed oscillations undertaken by the electron as it traverses an undulator.

A dipole propagating at relativistic velocities compresses the ripples in the forward direction of propagation since the electrons are propagating near, but not at, the speed of light, as in Figure 3.5. A quantitative evaluation describing relativistic Doppler shift of the central wavelength on the on-axis radiation can be calculated by using the appropriate Lorentz transformations. The on-axis spectral shape in the forward direction is, however, unchanged.

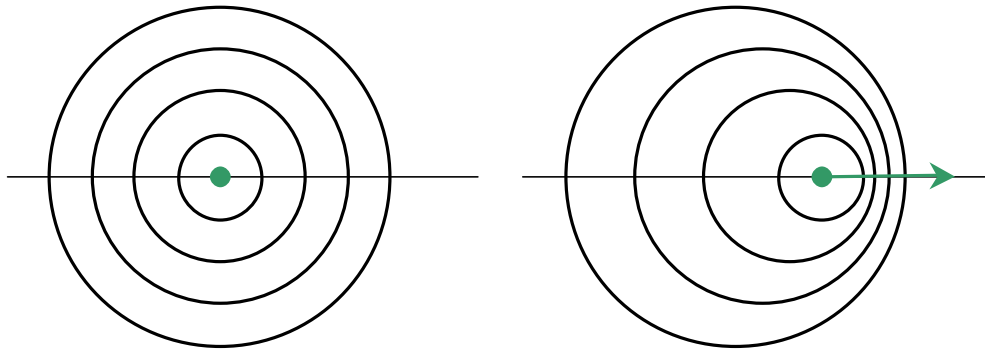


Figure 3.5: Radiation pattern of static hertzian dipole and Doppler shifted radiation pattern with compressed wavelength due to electron propagation at a constant relativistic velocity.

A more detailed discussion of synchrotron radiation can be found in David Attwood's book [Att99] and references therein.

3.2 Slicing in a Storage Ring

Electron slicing places an energy modulation of $\sim 100\text{fs}$ on an 50ps electron bunch using an ultrashort laser pulse. The problem is that simply scattering the laser pulse from the electron bunch does little in the way of efficiently exchanging energy between the light field and the electrons. Fortunately, efficient energy exchange between free-electrons and light fields is the purview free-electron lasers. In free-electron lasers, laser light and electrons co-propagate in a periodic magnetic structure—a wiggler or undulator—to amplify the light field using energy from the electrons. This is a means of placing an energy modulation on an electron bunch. A bend magnet provides dispersion—a means of translating the energy modulation into a spatial separation by sorting the electrons transversely by energy. In this way, ultrashort electron slices can be generated from the structures that are already used at current, modern synchrotron facilities.

3.2.1 Pictures at an Exhibition

The means by which electron slicing is performed is quite natural (in hindsight). The only means of creating a sub-picosecond time-structure is through the use of ultrashort pulse lasers, which routinely and reliably generate sub-picosecond pulses of optical

radiation. If an electron bunch interacts with an ultrashort laser pulse in a manner such that an imprint of equivalently short duration is left on the electron bunch, that imprint can be manipulated to generate an ultrashort slice of electrons which, in turn, can be used in radiating structures (i.e., bend magnets and insertion devices) to generate ultrashort pulse of x-rays as in Figure 3.6. Gaining an intuition for the physics of electron slicing is straightforward and is best accommodated through illustrations and concepts from elementary physics.

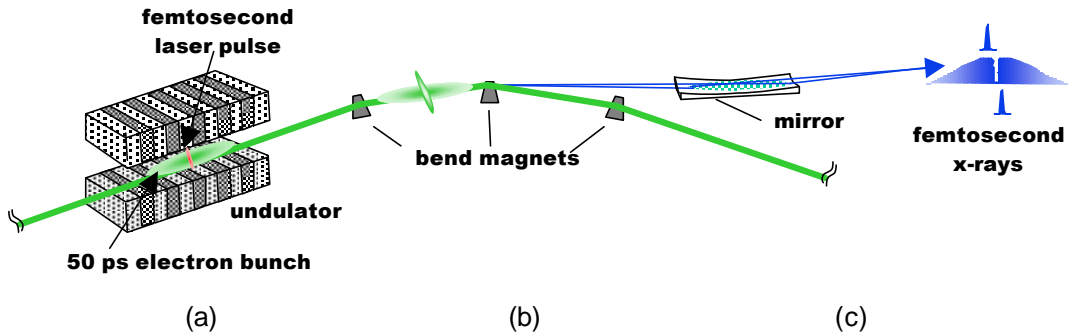


Figure 3.6: Electron slicing involves three steps. (a) Co-propagation of a laser pulse with an electron bunch places a femtosecond energy modulation on the long electron bunch. (b) In a dispersive section of the storage ring, the energy modulation is translated into a spatial separation. (c) A radiator generates x-rays that mimic the time-structure of the electron bunch, possessing ultrashort pulse of x-rays in the spatial wings of the main x-ray pulse. Illustration adapted from [SCC⁺01].

A free-electron that co-propagates with an ultrashort laser pulse leaves the interaction unaffected. The free-electron essentially rides the waves of the laser field, and leaves without doing any work on the field or having the field do work on it—whatever work is done to the electron in the first half-cycle of the laser field is given back to the laser field in the second half-cycle. To mediate net energy transfer requires the electron to have a transverse component of velocity to match the direction of the electric field of the laser as in Figure 3.7. Co-propagation of electrons and a laser pulse in an undulator satisfies this need: the undulator provides a transverse component to the electron trajectory and the laser polarization can be manipulated to match it.

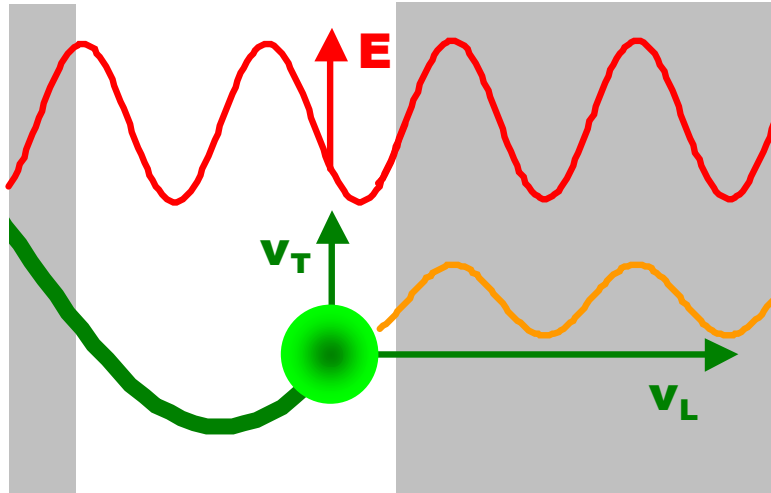


Figure 3.7: Net energy transfer between the electron and the laser field is a function of the electric field projected onto the velocity of the electron ($\mathbf{v} \cdot \mathbf{E}$). Energy exchange (and resultant modulation) requires the light polarization to be in the same plane as the electron oscillation.

A look at the behavior of an electron traversing an undulator provides a clue as to how to further optimize the energy transfer between the electron and a co-propagating laser pulse. The speed with which the electron travels through the undulator can be referenced against the light it emits as it performs oscillations. For each period of the undulator, the electron lags by the one optical cycle of emitted light, as in Figure 3.8. Intuitively, the lag makes sense. With each period of the undulator, the electron must emit one cycle of light, and thus the electron must be traveling at a velocity that is slower than the emitted light by one optical cycle per undulator period.

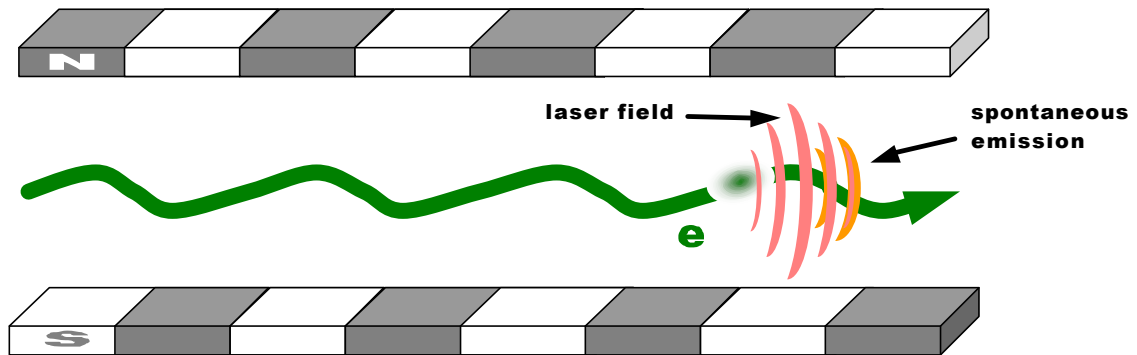


Figure 3.8: The undulator spontaneous emission precedes the radiating electron by an optical cycle per wiggler period. Laser light of the same wavelength as the spontaneous emission will track the progress of the electron in the same fashion as the spontaneous emission.

Now, if laser light of the same wavelength as the spontaneous emission were injected into the undulator at the same time as the electron, this light would also pass the electron by one optical cycle after a single wiggler period. This suggests a resonance condition that ensures energy transfer to the electrons (or to the laser field) through each period of the undulator for the entire duration of the undulator. Illustrated in Figure 3.9, as the electron traverses an undulator period, it will again see an optical field of the same phase that it saw as it entered the preceding period. This optimal interaction is guaranteed if the laser wavelength and the spontaneous emission wavelength match, allowing energy transfer to be to (or from) the electron for the entire duration of the undulator.

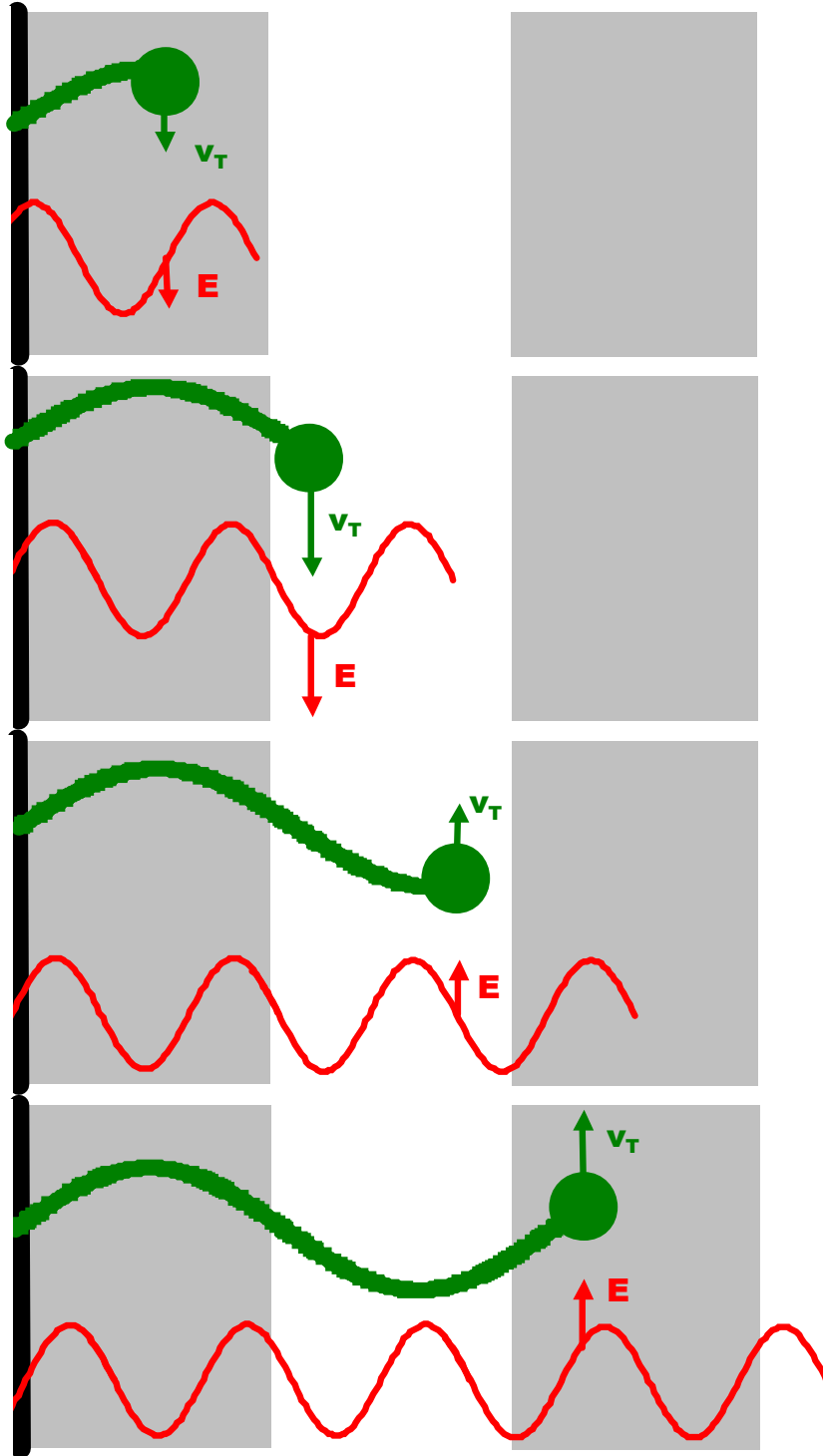


Figure 3.9: Cartoon of laser and electron co-propagation in an undulator under resonance conditions. The electron enters at the laser field maximum in the top panel. As the electron proceeds through the undulator period, it sees a laser field of the same orientation as its transverse motion; this is repeated as the electron enters a next undulator period, and has slipped a full optical cycle. In this way, energy exchange is always in the direction of the electron or laser field for the entire length of the undulator.

Using simple pictures, it is also clear that this sort of energy modulation can be imposed on a harmonic of the electron oscillation. If the magnetic field of undulator is strong enough to be in the wiggler regime, where a spectral comb of the radiation is emitted rather than a single wavelength, Fourier decomposition suggests the resonance condition can be satisfied simply by matching the laser wavelength to the desired harmonic in the spectral comb.

Once the electrons have been imprinted with an ultrashort energy modulation, the modulated electrons can be separated spatially by traversing a dispersive section of the storage ring. The energy-modulated electrons will be sorted from the un-modulated electrons, physically separating themselves from the long electron bunch. Electrons that have been accelerated will take an outer path, electrons that were decelerated will take an inner path relative to those electrons which were unaffected by the laser. A hole in the main electron bunch is created as the energy-modulated electrons are evacuated to spatial wings, as illustrated in Figure 3.10.

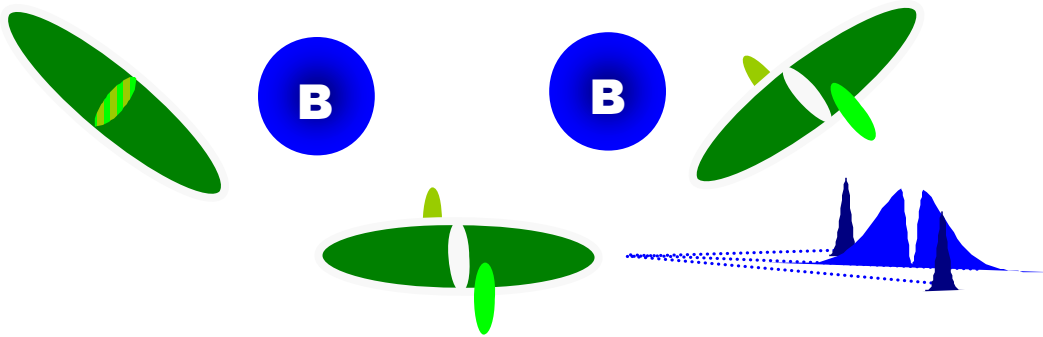


Figure 3.10: An energy modulated electron bunch will spatially separate in a dispersive section of the storage ring, such as a bend magnet. A second bend magnet (or an insertion device) can be used to generate ultrashort pulses of radiation from the electron slices that have been translated into the spatial wings of the main electron bunch.

Unfortunately, in this scheme, there is a limit to which energy can be imparted to or taken away from an electron. An electron interacting with the laser field will be given more energy (or have energy taken away from it) with every wiggler period. An electron traveling faster (with more energy) or slower (with less energy) through the wiggler will oscillate with a correspondingly higher or lower frequency, and the radiation it emits will

also be correspondingly blue- or red-shifted. This is departure from the resonance condition for optimal energy exchange, and places an upper limit on the amount of energy that can be transferred between the electrons and laser field. Physically, this corresponds to an electron being accelerated or decelerated into the nearest null of the optical field where no energy can be transferred— $\mathbf{v} \cdot \mathbf{E} = 0$, since $\mathbf{E} = \mathbf{0}$. This presents a significant experimental limitation: the extent to which an ultrashort slice of electrons can be spatially separated from the main bunch depends on the degree of energy modulation achievable relative to the energy spread of the main bunch.

3.2.2 Mathematical Considerations

The proper design and implementation of an electron slicing source requires mathematical detail to quantify the efficiency with which the source is producing ultrashort pulses of x-rays. A mathematical description of slicing also provides a quantifiable means of scaling and improving the source.

The relevant analytic expressions are those that establish the resonance condition and describe the energy exchange due to the electron-laser interaction. The on-axis spontaneous emission from a wiggler is given by equation (3.1)

$$I_{\text{radiated}} = \frac{I_w}{2g^2}(1 + K^2/2) = I_{\text{laser}} \quad (3.1).$$

The spontaneous emission must match the slicing laser wavelength. The on-axis spontaneous emission wavelength is simply the wiggler period, I_w , appropriately scaled by the relativistic energy of the electrons. The two factors of g reflect Lorentz transformations into the moving frame of the electrons and then back into the lab frame. The magnetic field strength enters through the K -parameter given by equation (3.2)

$$K = \frac{eB_o I_w}{2\mathbf{p}mc} \quad (3.2).$$

K is the magnitude of the vector potential in the wiggler set by the strength of the magnetic field and wiggler period.

The amplitude of the energy modulation can be calculated by considering the total field energy in the wiggler due to the spontaneous emission and laser radiation as in equation (3.3).

$$\begin{aligned} A &\sim \iint |E_L(\mathbf{w}, \bar{r}) + E_R(\mathbf{w}, \bar{r})|^2 dS d\mathbf{w} \\ &= A_L + A_R + 2\sqrt{A_L A_R} \frac{\Delta \mathbf{w}_L}{\Delta \mathbf{w}_R} \cos \mathbf{f} \end{aligned} \quad (3.3)$$

A_L is the energy in the laser field and A_R is the energy in the spontaneous emission field of the undulator given by equation (3.4).

$$A_R \cong \mathbf{p} \mathbf{a} \hbar \mathbf{w}_R \frac{K^2/2}{(1 + K^2/2)} \quad (3.4)$$

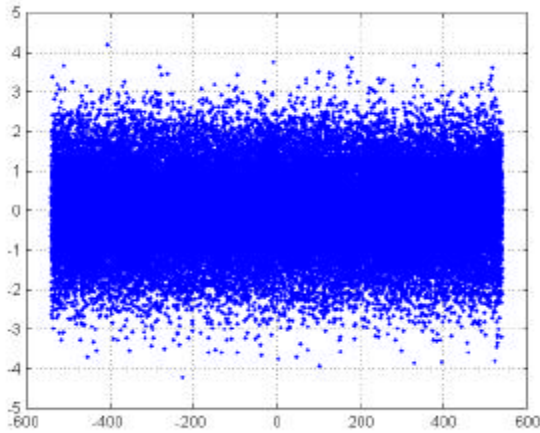
where \mathbf{a} is the fine structure constant. The cross-term

$$(\Delta E)^2 \cong 4A_L A_R \frac{\Delta \mathbf{w}_L}{\Delta \mathbf{w}_R} \quad (3.5)$$

is the magnitude of the energy of modulation which can be achieved under optimal conditions. Equation (3.5) also points out some of the experimental considerations required to enhance the laser-electron interaction.

Ultimately, computational models are needed to calculate the details of the energy and spatial distribution of a sliced electron bunch. Many approaches can be taken to compute the electron distributions: a probabilistic distribution can be manipulated [SCC⁺01] according to energy exchange and storage ring time-of-flight dispersion parameters or a large number of particles with the appropriate initial statistics can be processed with the same dynamics. The latter has been demonstrated here. Once the appropriate computations have been performed, the appropriate sections can be taken to fit experimental data, since the time-structure of synchrotron radiation mimics the time-structure of the radiating electron bunch.

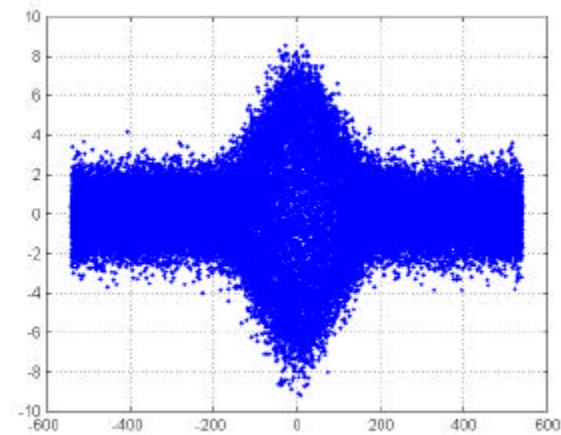
The first consideration to make is the initial energy and spatial distribution for an electron bunch. An electron bunch can be assumed to have an electron density that is normally distributed in both longitudinal and transverse direction. Since the aspect ratio



of the electron slices to the electron bunch is so disparate (almost three orders of magnitude), it is only necessary to simulate a small longitudinal region of an electron bunch near its maximum. Since a gaussian distribution is flat near its maximum, the simulated longitudinal distribution can be assumed to be

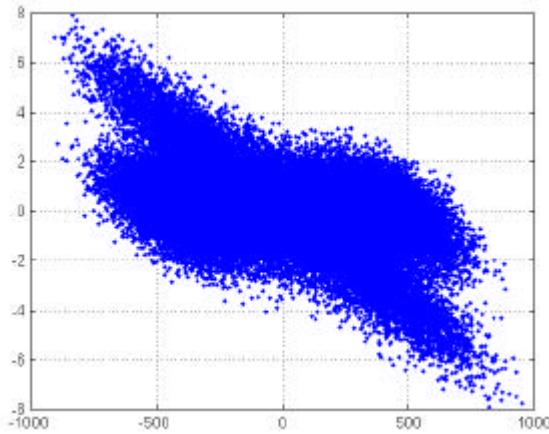
uniform. The energy distribution of the electron bunch is also normally distributed. However, since an electron above the mean bunch energy is as likely to be in the same physical position as an electron below the mean bunch energy, a valid electron energy distribution is also has uniform distribution in time and normal distribution in energy.

To enact energy modulation due to a laser-electron interaction, a modulation can be imposed on the initial energy distribution, reflecting the duration of the laser pulse and desired strength of modulation, assuming resonance conditions are met. Changes will only be reflected in the energy distribution of the electron bunch. Without dispersion, there is no alteration to the spatial profile of the bunch appears.



The spatial evolution of the energy-modulated electron bunch is simply a transformation performed on the spatial

distribution of the electrons. Embodied in the transformation are the dispersion and time-of-flight properties of the storage ring that act on the electrons depending on their energy and physical location in the bunch.



Appropriate sections of these calculations can be taken to fit data taken from visible light cross-correlation measurements and x-ray beam profile measurements to determine if optimal experimental conditions are being met for the generation of femtosecond x-ray pulses.

As is clear from the final computation, the femtosecond x-ray pulses sit against any x-ray background produced by main electron bunch. The required separation for useful femtosecond pulses of x-rays must be judged against the non-specular scattering background of the long x-ray pulse from x-ray optics that may overshadow the femtosecond x-ray pulse.

3.3 Implementation at the Advanced Light Source: Beamline 5.3.1

The femtosecond x-ray slicing source at beamline 5.3.1 is realized within the context of the greater scientific enterprise of the ALS. The ALS is a third-generation synchrotron source with a storage ring operating at 1.9GeV. The ALS produces radiation with photon energies from the mid-infrared (BL 1.4) out to 40keV (BL 8.2). The range of inquiry at the ALS is equally diverse, filling the spectrum from basic spectroscopy and crystallography to highly applied pursuits such as extreme ultraviolet (EUV) lithography and high-precision optical metrology, as illustrated in Figure 3.11.

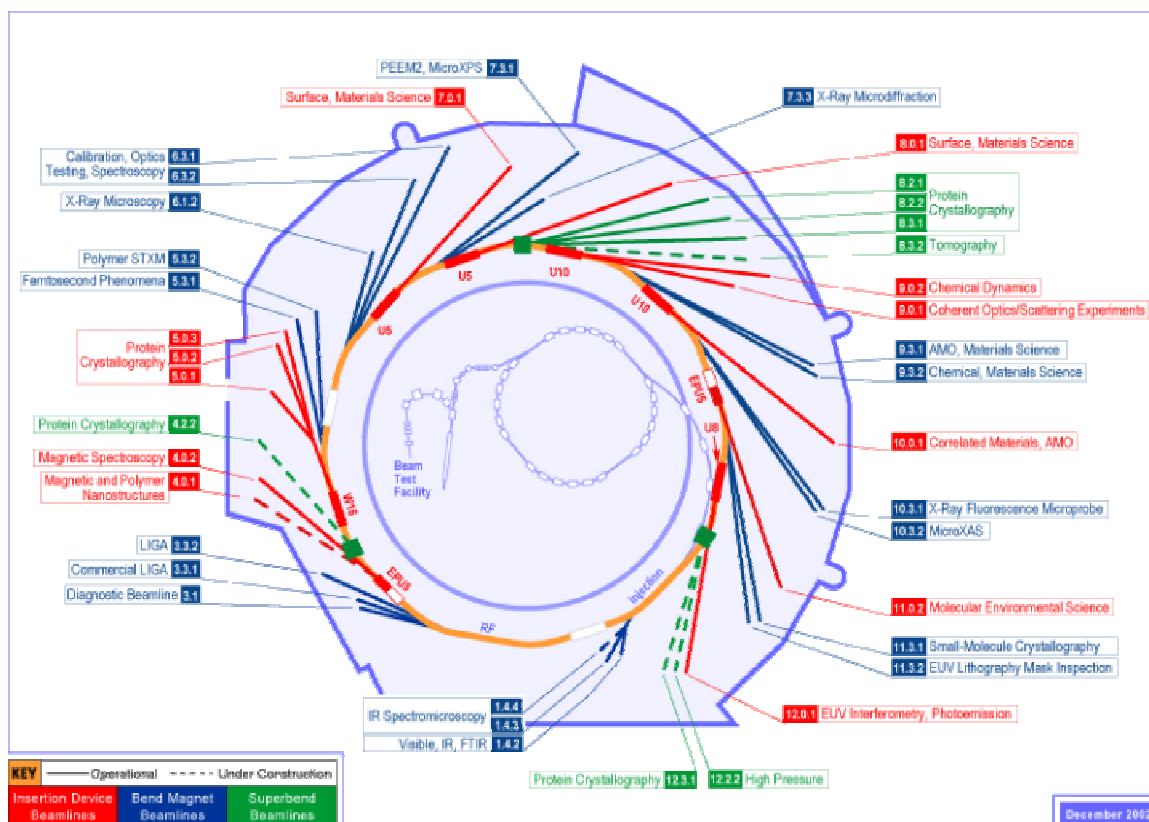


Figure 3.11: Overview of the breadth of scientific inquiry being actively pursued at the ALS. Figure from www-als.lbl.gov.

The development of ultrashort x-ray pulses at this facility, in principle, allows for all the proven capabilities of the ALS to be applied in a time-resolved fashion at the physically limiting time-scale set by the vibrational modes in condensed matter systems. High resolution structural, electronic and magnetic studies of material systems can now be augmented by studies of the underlying microscopic dynamics—excitation and decay pathways—that give rise to the equilibrium macroscopic properties under investigation.

The slicing source resides at beamline 5.3.1. Beamline 5.3.1 is a general-purpose bend-magnet beamline with a single toroidal collection optic in the front-end to collect radiation from the entire spectrum. The slicing source and beamline experimental facilities revolve around a high-average power, ultrashort pulse laser system [BDM⁺98] synchronized to the master oscillator that drives the storage ring. The laser system is

based on titanium-doped sapphire, with a home-built oscillator followed by a chirp-pulse amplification chain, as schematically depicted in Figure 3.12. The oscillator feeds two amplifier chains: one amplifier is used for electron slicing and the other amplifier produces excitation pulses for experiments. In this way, the sample excitation pulse and the generated x-ray pulse are synchronized to a precision limited by mechanical fluctuations of optics in the laser system.

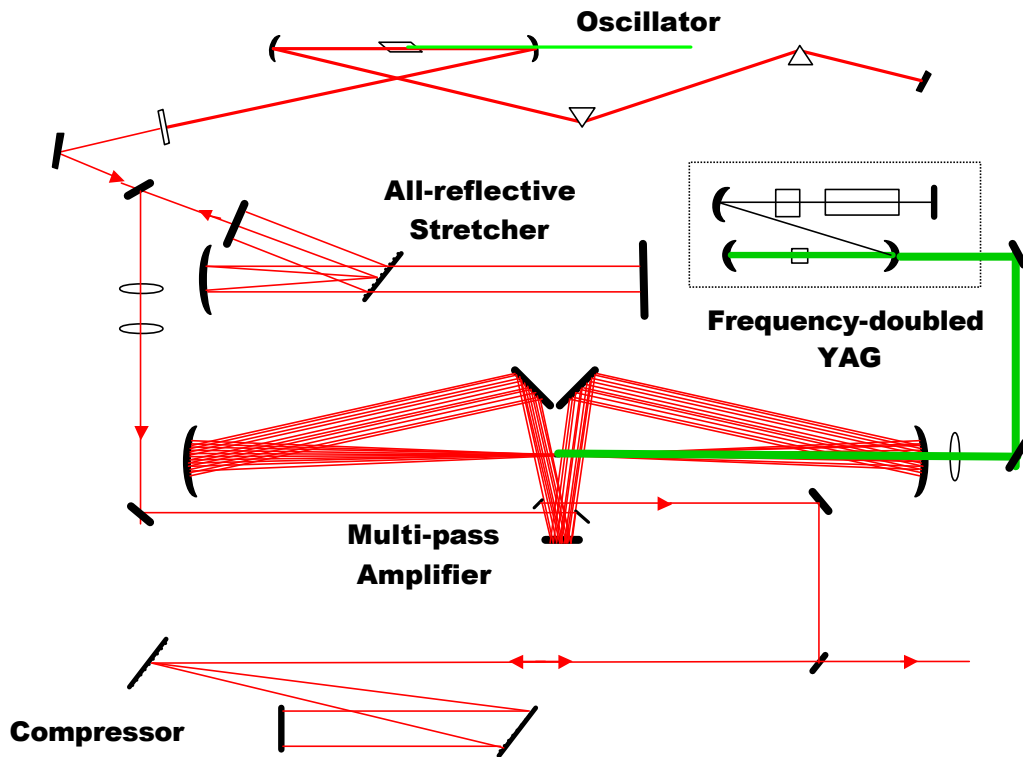


Figure 3.12: Schematic of an ultrashort pulse laser system based on Ti:Sapphire. Nonlinear optical processes in the Ti:Sapphire crystal generates a low-energy, ultrashort pulse in the oscillator. The pulse is then amplified using chirped-pulse amplification techniques to prevent damage in optical components as it acquires energy.

The laser pulse generated for slicing is delivered to an optical port of the storage ring and injected into the straight section of the storage ring that houses wiggler W16. The laser

and electron beam propagate collinearly through the wiggler, placing the energy modulation on the electron bunch.

A number of diagnostics are used to properly align the laser beam to the electron beam. Coarse alignment is performed by imaging the near- and far-field of the visible portion of the spontaneous emission of the wiggler on a camera. The laser image is then aligned to overlap in the appropriate positions.

Fine alignment requires diagnostics that measure explicit artifacts of the laser-electron interaction. One consequence of optimizing the energy modulation of the electron bunch is the complementary amplification of the slicing laser pulse. By picking off the femtosecond laser pulse after the interaction region and measuring its single-pass free-electron laser gain, an assessment of the laser-electron interaction can be made. The spatial overlap of the slicing pulse and the electron bunch can then be fine-tuned by optimization of the gain.

Optimization can also be performed by directly making measurements on the visible portion of the spectrum radiated by the sliced electrons. The benefit of bend magnet radiation is that electrons radiate with the same time-structure through an extremely broad spectrum—in principle, the time-structure of visible light reflects the time-structure of the x-rays generated by the same electrons. Extracted through an optical light port, the time-structure of the visible synchrotron radiation can be diagnosed with the standard cross-correlation techniques used in ultrafast optical spectroscopy. Since a sliced electron bunch will have a void corresponding to the electrons which have been evacuated into the spatial wings, a cross-correlation scan will show a dip in the synchrotron pulse. Spatial alignment can be optimized by increasing the amplitude of the dip.

Once the energy modulation has been translated into a spatial separation, the electrons can be used in any radiator to generate x-rays. Beamline 5.3.1. is fed by a bend magnet that follows the modulating insertion device; choosing a radiator nearest the slicing

region of the storage ring allows for the extraction of the shortest possible synchrotron pulses. The radiation generated by the bend magnet is collected by a toroidal imaging mirror, and is guided into an experimental hutch where it is spectrally shaped and aligned for pump-probe experiments as is schematically depicted in Figure 3.13.

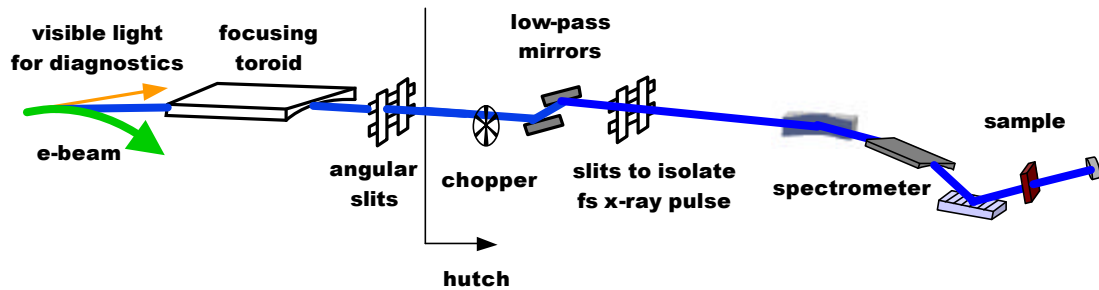


Figure 3.13: Schematic of BL 5.3.1 with x-ray hutch. X-rays from a bend magnet are apertured, transported and monochromatized before being placed on a sample to measure absorption spectra.

As the energy modulated electron bunch circulates the storage ring, the perturbation imposed by the slicing process dissipates. The electrons evacuated to the transverse wings smear longitudinally, and eventually become re-absorbed by the main bunch due to dampening mechanisms implemented in the storage ring.

3.4 Source Characterization

3.4.1 Single-Pass Free Electron Laser Gain

A direct measurement of the interaction between the electron beam and laser pulse is a measurement of the single-pass free-electron laser gain experienced by the slicing laser pulse. The energy given to and taken away from electron beam is complemented by energy taken away from and given to the optical field of the laser pulse. As depicted in Figure 3.14, the single-pass free-electron laser gain spectrum is the derivative of the spontaneous emission spectrum of the undulator. The physical interpretation is that the

energy required to accelerate and decelerated the electrons comes from and is given to energy in the optical field that is slightly red and blue of the resonant optical wavelength.

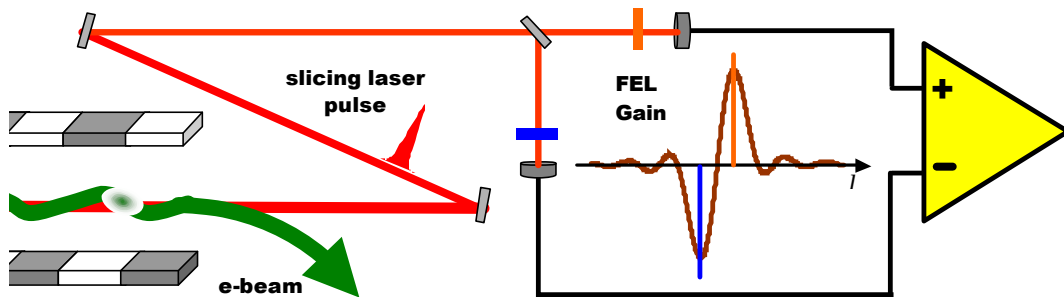


Figure 3.14: Schematic of single-pass FEL gain measurement apparatus. Laser light extracted *after* the laser-electron interaction is split and filtered in spectral positions that yield greatest gain and loss to perform differential measurements. The greater the interaction with the electrons, the greater the gain (and loss) measured in the laser light.

Laser light is extracted after it has interacted with the electron beam. A differential measurement is then made on the light at wavelengths of maximum gain and loss. Since the gain scales with the number of electrons involved in the interaction, by stepping through the time-delay between the slicing laser pulse and electron bunch, the bunch length of the electrons can be characterized [SCG⁺99]. A plot of this measurement is displayed in Figure 3.15

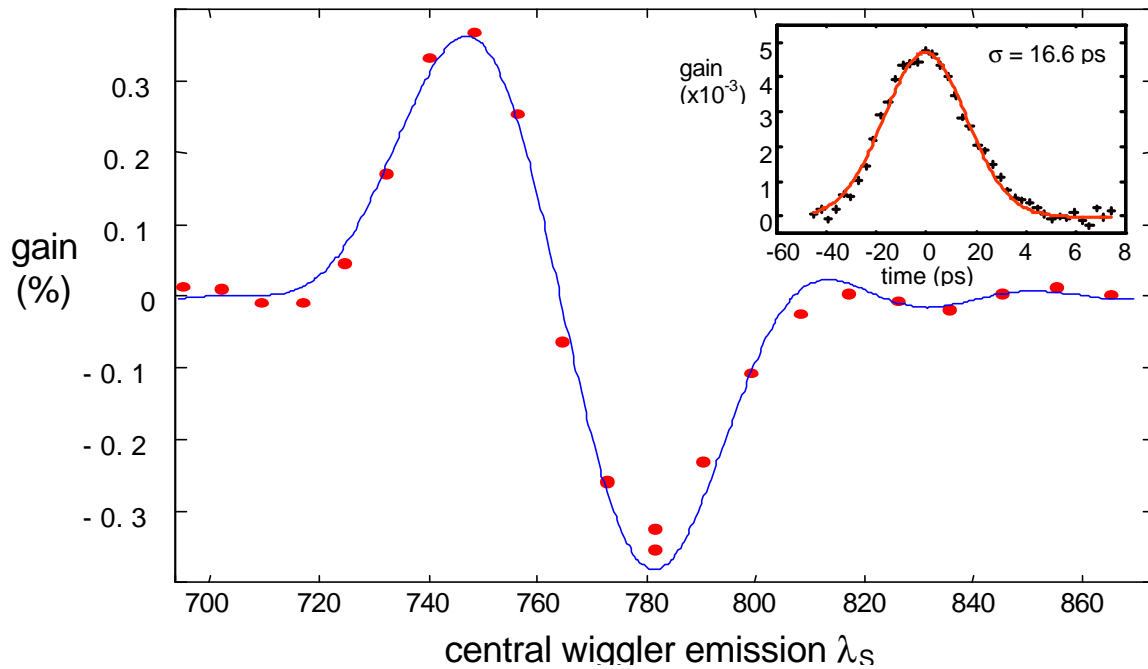


Figure 3.15: Plot of gain measured as a function of the central wavelength of the insertion device as it is tuned through the resonance. The inset displays a time-scan of the gain measurement under resonance conditions. The inset shows how the time-structure of the electron bunch can be characterized using this method.

3.4.2 Visible Light Cross-correlation

A complementary means of gauging the interaction between the laser and electrons is to perform a cross-correlation of the visible light from the synchrotron. Synchrotron light from the infrared through the hard x-ray region is emitted with the same time-structure, and mimics the time-structure of the electron bunch from which they originate. Using the visible portion of the spectrum is convenient. Techniques for cross-correlation characterization of short pulses of optical light using sum-frequency generation are reliable and easily performed. Schematically illustrated in Figure 3.16 is a simple apparatus required to characterize the time-structure of the synchrotron pulse against an optical pulse derived from the slicing laser pulse.

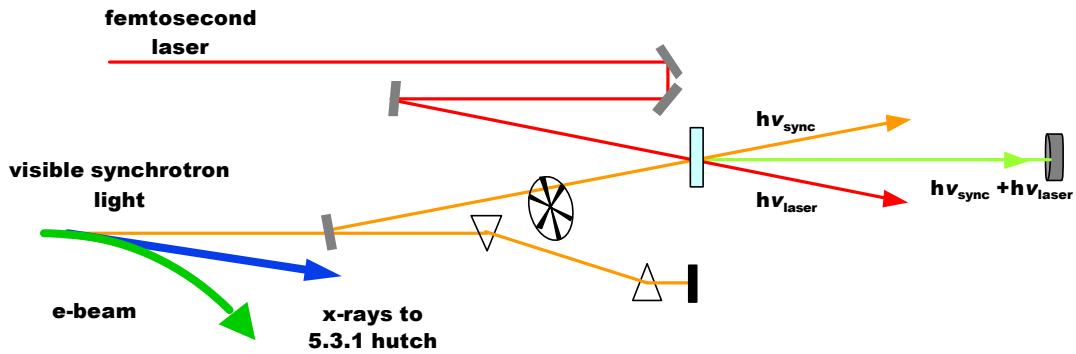


Figure 3.16: Visible synchrotron light is extracted and mixed in a sum-frequency generation crystal with laser light derived from the slicing laser. This is a means of profiling the time-structure of the electron bunch with high time-resolution.

By selecting different transverse regions of the synchrotron pulse the time structure of the electron bunch can be mapped out. The hole created by the evacuation of electrons from the electron bunch can be observed by selecting the central portion of the synchrotron pulse. The femtosecond pulses of synchrotron light can be observed by selecting the light from the wings of the synchrotron pulse as in Figure 3.17.

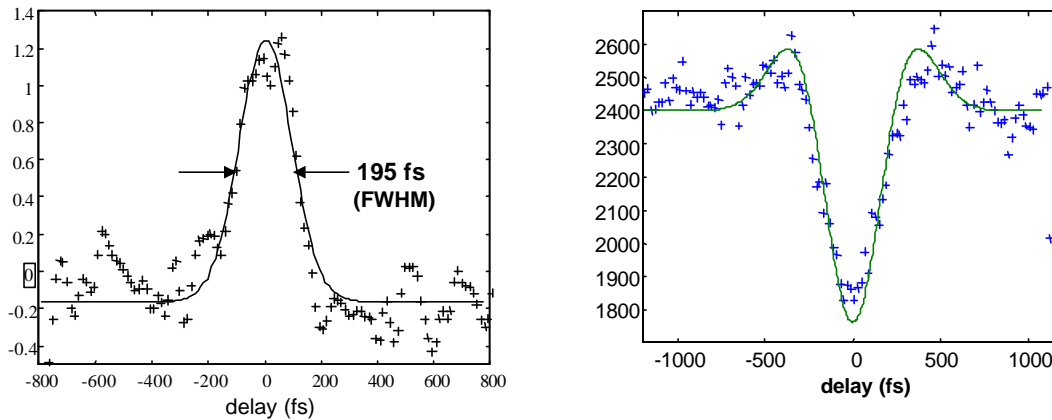


Figure 3.17: Cross-correlation traces made between visible synchrotron pulses and laser pulses from [SCC⁺00] and [SCC⁺03]. (Left panel) The femtosecond synchrotron pulse is measured by setting an aperture in the transverse wings of the synchrotron beam. (Right panel) A dip due to the evacuation of electrons can be observed by setting an aperture to collect the central portion of the synchrotron beam.

3.4.3 Spatial Beam Profile at ALS Beamline 5.3.1.

The most definitive and useful measurement of the sliced, femtosecond x-ray source is a measurement of the x-ray transverse beam profile. The energy modulation of the electrons is translated directly into transverse separation of sliced electrons from the main electron bunch by storage ring dispersion. Ultimately, it is the number of discernible x-ray photons from the electron slice against the background of the main electron bunch that is critical for pump-probe experiments. The measurement apparatus for a beam profile measurement is schematically illustrated in Figure 3.18.

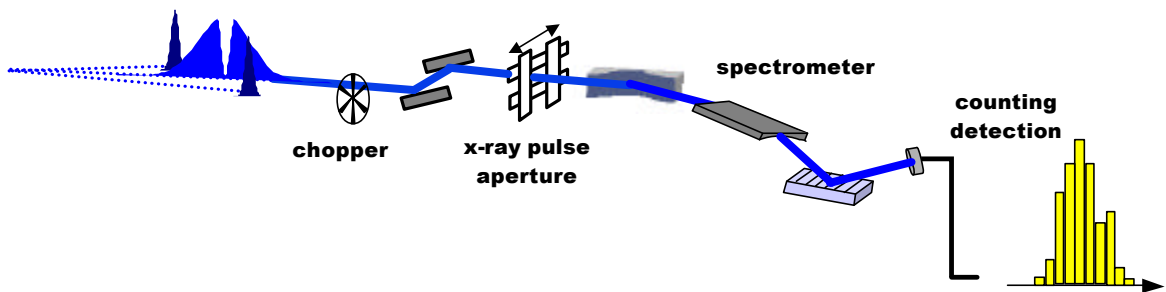


Figure 3.18: Counting detection used to directly observe femtosecond x-rays. The x-ray beam is apertured to isolate the femtosecond x-ray pulses before being detected. By setting the aperture at different positions, a transverse profile of the x-ray beam can be developed and compared to calculations of slicing efficiency.

The measurement scans the transverse profile of the incoming x-ray beam in the plane of the storage ring dispersion. There is an x-ray wavelength dependence on the beam profile as at short-wavelengths: non-specular scattering contributes greatly to the observed background imposed by the main electron bunch. Measured horizontal profiles of the x-ray beam and the observed femtosecond sliced pulses are presented Figure 3.19.

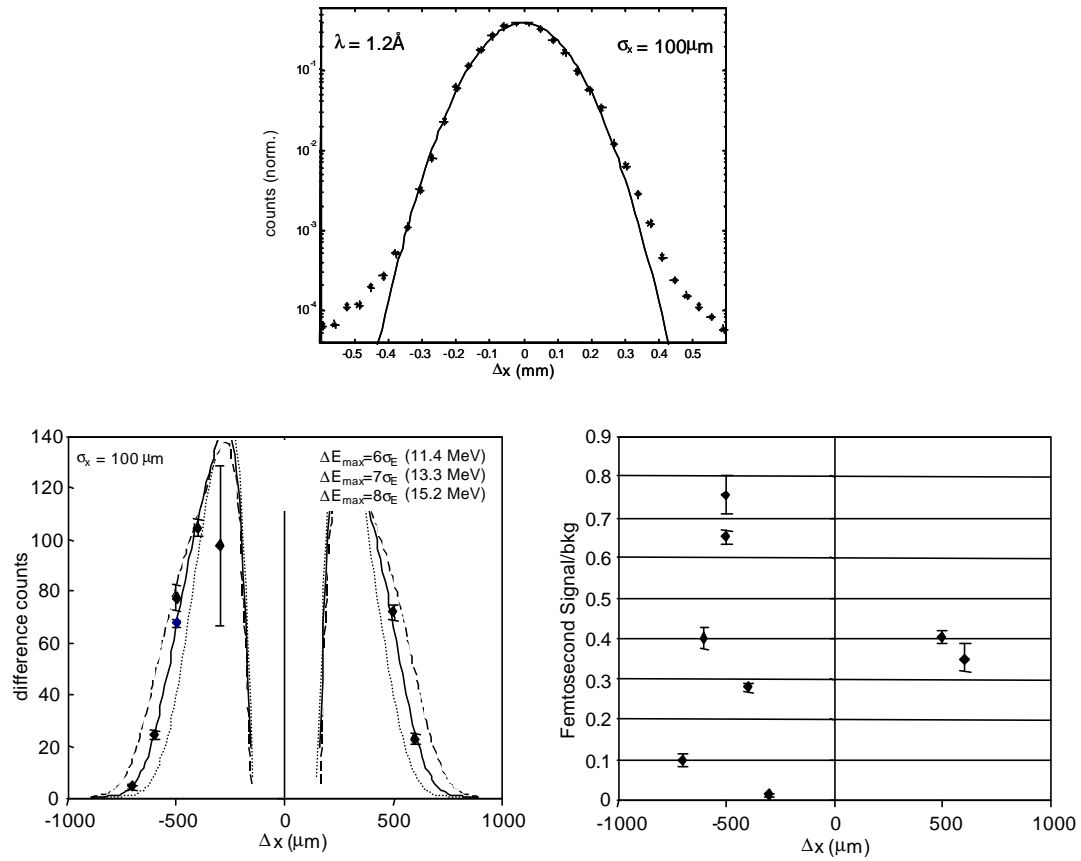


Figure 3.19: X-ray beam profile measurements at BL 5.3.1 from [SCC⁺03]. The top is a profile of an unsliced x-ray beam fitted to a gaussian function—notice the departure from the gaussian profile due to non-specular scattering in the wings of the x-ray beam. The lower plots are differential profiles displaying the femtosecond bunches fit to model calculations to estimate the degree of energy modulation imposed on the electron bunch.

4 TIME-RESOLVED STUDIES OF TRANSITION METAL COMPLEXES

Transition metal complexes are extremely useful model systems to study complex interactions of electronic, spin and structural degrees of freedom in molecules. These molecules have a hub of one or more transition metal ions bonded to a number of small, organic molecules called *ligands*. An example of a transition metal complex is pictured in Figure 4.1. Transition metal complexes can be engineered to have different electronic structure, magnetic properties and structural ground states by judicious choice of ligands and transition metal ions [BL03]. Appropriately tailored complexes can enhance or isolate particular properties and behaviors for study [MWM⁺93].

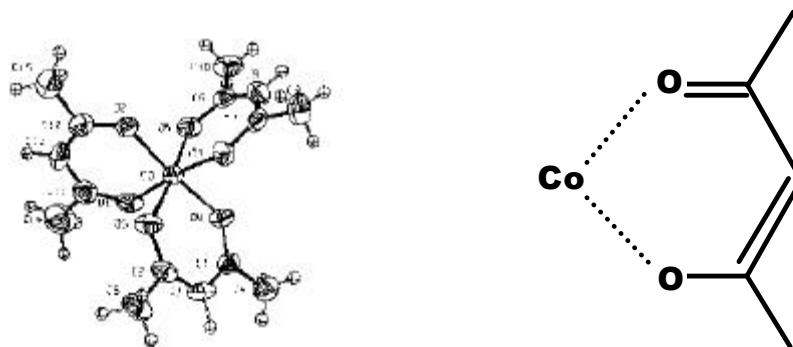


Figure 4.1: Trisacetylacetonatocobalt(III), $\text{Co}[\text{acac}]_3$, is a transition metal complex formed of a Co^{3+} ion surrounded by three acetylacetonate ligands. To the left is the atomic structure of the molecule taken from [KR74]. To the right is a schematic zoom of a single acetylacetonate ligand bonded to the cobalt ion.

4.1 Engineering Molecular Properties

The principle underlying the design of a transition metal complex is the manipulation of the d-orbitals of the transition metal ion. Ligands lower the spherical symmetry of the bare ion and break the energetic symmetry of the d-levels, which in turn affect the spin state and atomic structure of the ground state of the complex. The electron density of the five atomic d-orbitals is illustrated in Figure 4.2. Three of the five orbitals (d_{xy} , d_{yz} , d_{xz}) are qualitatively degenerate and are oriented *between* Cartesian axes. The remaining two orbitals (d_z^2 and $d_{x^2-y^2}$), on the other hand, are oriented *along* axes.

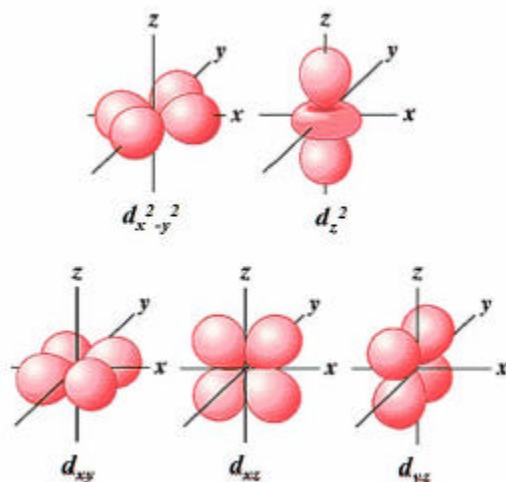


Figure 4.2: Spatial orientation of electron density distribution of atomic d-orbitals taken from [Zum00]. The d_z^2 and $d_{x^2-y^2}$ in the top row have their lobes directed along Cartesian axes; d_{xy} , d_{yz} and d_{xz} orbitals have their lobes directed between Cartesian axes.

In single ion complexes, two common ion-ligand bonding geometries coordinate ligands in tetrahedral and octahedral symmetry. In these two geometries, ligand s -bonding orbitals are directed either along Cartesian axes (in octahedral coordination) or between axes (in tetrahedral coordination). The ligands break the spherical symmetry of the bare ion, forcing the five d-bands of the transition metal ion to split in energy.

A simplified physical perspective to help understand the lifting of energetic degeneracy is to consider each orbital of the ion and ligand to be an electron cloud. If a ligand orbital is directed along a Cartesian axis, there is a great energy cost due to

repulsion from the ion orbital oriented along the same axis as the two clouds spatially overlap. For the ion orbital that is aligned between axes, however, the energetic cost is much less, as there is little to no forcible overlap between it and the ligand orbital. The energetic ordering of the split d-orbitals is depicted in Figure 4.3 for complexes of octahedral and tetrahedral coordination. The split ionic d-levels are referred to as t_{2g} bands (those directed between axes— d_{xy} , d_{yz} , d_{xz}) and e_g bands (those directed along axes— d_z^2 and $d_{x^2-y^2}$), and are ordered in a manner reflecting the spatial orientation of those orbitals with respect to those of the bonding ligands.

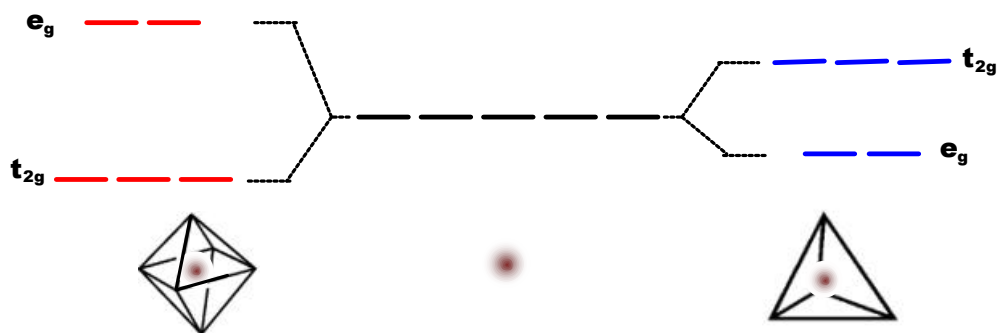


Figure 4.3: The d-orbitals of a bare ion are split according to symmetry considerations. In a bare ion, the d-orbitals are energetically degenerate. Degeneracy is lifted when the ion bonds to ligands. The d-orbitals separate to form t_{2g} and e_g bands and energetically order according to ligand coordination—to the left is octahedral (O_h) coordination and to the right is tetrahedral (T_d) coordination (the bonding atom from the ligand sits on the apices of the polyhedron).

The electrons of the d-shell populate the re-organized electronic states based on energetic considerations, affecting the spin state. Electronic orbitals are filled based on Hund's rule. Each orbital within the same band (e_g or t_{2g}) is occupied with an electron of parallel spin orientation before a second electron of opposing spin doubly occupies an orbital. The equilibrium spin-state of the molecule results from the filling of the split d-orbitals: there is competition between spin-pairing energy (energy to doubly occupy an orbital) and the ligand-field splitting energy (energy separating e_g and t_{2g} levels). If the ligand-field splitting energy is lower than the spin-pairing energy, the five d-orbitals will appear degenerate and be filled accordingly. If the ligand-field splitting energy is higher

than the spin-pairing energy, however, only the orbitals of the lower energy band will appear degenerate, and be populated according to Hund's rule, yielding a drastically different electronic and spin ground state. In this way, by choosing ligands that provide stronger or weaker ligand-field splitting, low- or high-spin complexes can be engineered.

The ground state atomic structure also depends on the electronic configuration of the transition metal complex. The ion-ligand bond length and bond strength depend on the occupation of bonding or anti-bonding orbitals. In an octahedrally coordinated complex with σ -donor ligands, empty metallic s- and p-orbitals and filled ligand donor orbitals meld to form strongly bonding orbitals energetically positioned below the d-block and strongly anti-bonding orbitals energetic positioned above d-block. Split d-orbitals tend to form a non-bonding lower band and a weakly anti-bonding upper band. The ligand-field splitting energy, again, determines the population of the weakly anti-bonding level, influencing the ground state atomic structure and structural stability of the complex. If an electron from the d-shell is excited into strongly anti-bonding, upper lying states, the effect of the electron on the structural stability of the complex becomes even more pronounced, initiating structural dynamics that will influence the excited-state evolution of the molecule.

The result of such strong correlations between the electronic structure, spin state and structural stability in these molecules makes them interesting, tunable model systems for the study of correlated dynamics. Molecular crystals of transition metal complexes have also demonstrated interesting cooperative (long-range) effects [RGG⁺92].

4.2 An Example: Fe[py₃tren]²⁺

Fe[py₃tren]²⁺ is a member of a family of iron-based, transition metal complexes called iron(II) complexes. These molecules all have an Fe²⁺ ion center. Molecules in this family exhibit similar properties, though specific properties, such as spectral location of optical absorption bands and equilibrium spin-state, can be tailored by using different ligands. Fe[py₃tren]²⁺ is a photo-sensitizer used in solar cells; other interesting examples of iron(II) complexes include haemoglobin which carries oxygen in blood [GGG00].

Structurally, $\text{Fe}[\text{py}_3\text{tren}]^{2+}$ can be best described as a carousel. The tridentate, tripod *tren* ligand is a crown. Three *pyridine* rings form a lower tier. And, chelating bonds form a second tier that bridges the *tren* crown to the three pyridines. Illustrated in Figure 4.4, a three-fold axis of symmetry can be observed by looking down the crown. Six nitrogen atoms form the first coordination shell around the iron in octahedral symmetry.

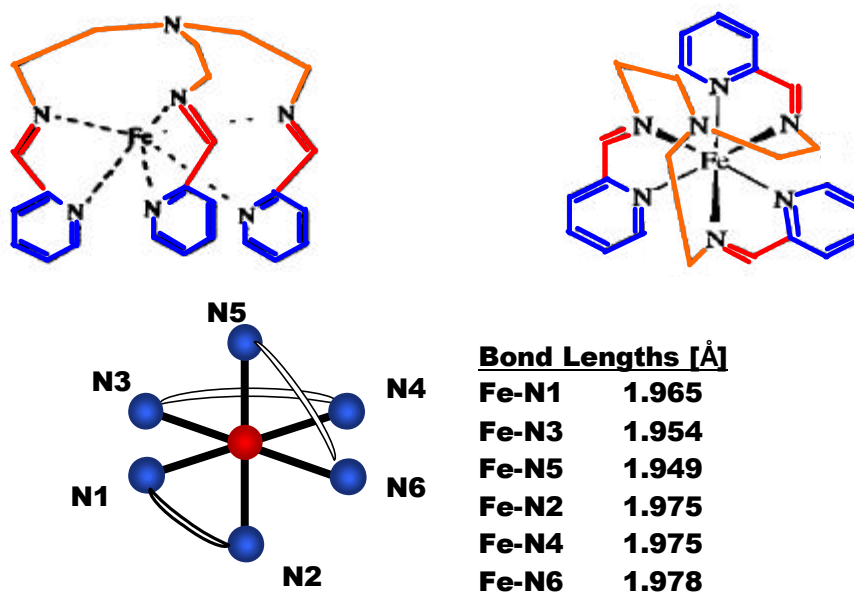


Figure 4.4: $\text{Fe}[\text{py}_3\text{tren}]^{2+}$ schematically depicted. The *tren* ligand is coded in orange, the pyridine ligands are coded blue and chelating bonds are coded in red. A three-fold axis of symmetry is clear from the perspective of the upper-left graphic. The bond lengths associated with the molecule in its low-spin, equilibrium state are presented.

For octahedrally coordinated Fe^{2+} systems, the d-shell is split into two levels, as previously illustrated in Figure 4.3. The six available d-electrons (this is a d^6 system) populate these states according to Hund's Rule, determining their configuration by weighing the splitting energy of the ligand field against the spin-pairing energy required to co-exist in a partially-filled orbital. With a strong ligand-field splitting energy, the tendency will be for electrons to pair in the lower t_{2g} state, producing a low-spin ground state, $S=0$. With a weaker ligand-field splitting energy, the energetic barrier to pair is greater than the energetic barrier separating the two manifolds. Electrons will populate

the higher-lying manifold to yield a high-spin ground state, $S=2$. The different electronic configurations, in turn, have an effect on the atomic structure of the complex—the more tightly bound low-spin complex exhibits shorter the bond lengths.

A tool used to illustrate the effect of varying ligand-field splitting strength on the electronic structure of a given complex is the *Tanabe-Sugano* (T-S) diagram.

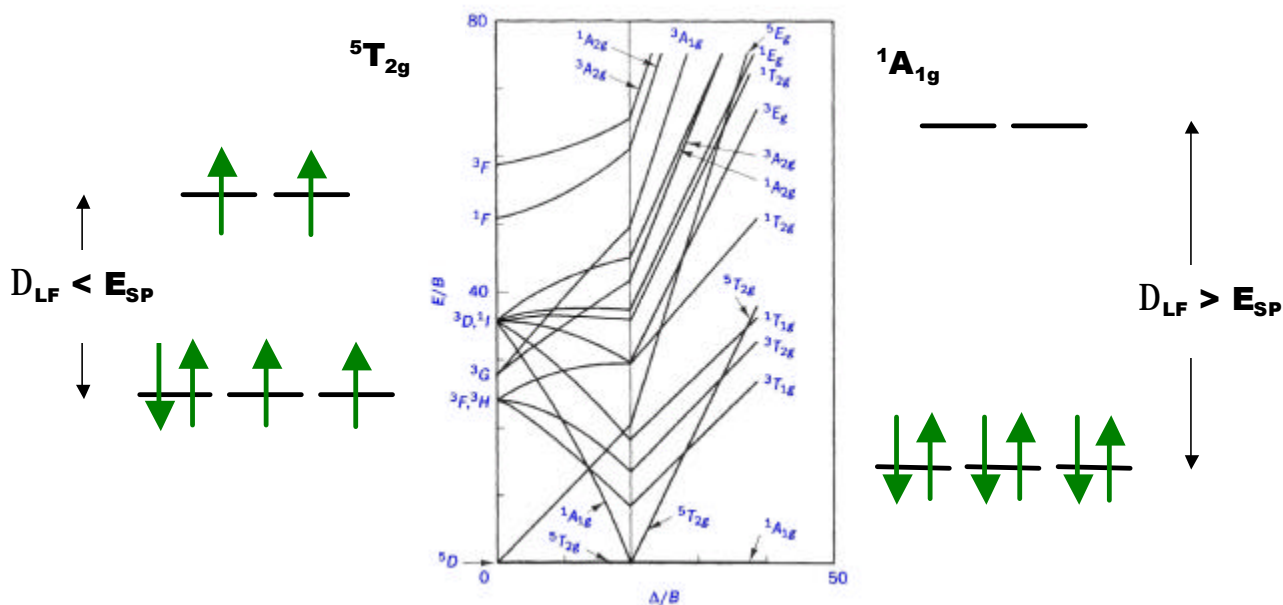


Figure 4.5: Tanabe-Sugano diagram for d^6 system with octahedral coordination. The d-shell of the possible ground-state electronic configurations is explicitly illustrated. The high-spin ${}^5T_{2g}$ state is preferred with a low ligand-field splitting energy. The low-spin, ${}^1A_{1g}$ state prevails when ligand-field splitting energy is larger than the spin pairing energy.

Illustrated in Figure 4.5, the T-S diagram has the ligand-field splitting energy as its abscissa and electronic energy as its ordinate. Both are normalized by the *Racah B-parameter* for the system. The electronic configurations are labeled by spectroscopic designations based on group-theoretic considerations. There is sharp threshold to demark the crossover where the ligand-field splitting energy becomes greater than the spin-pairing energy. The resultant re-organization of the lowest-lying electronic and spin state is self-evident. $\text{Fe}[\text{py}_3\text{tren}]^{2+}$ has a ligand-field splitting energy greater than spin-pair

energy. Its ground state configuration, then, is to the right of the threshold in the T-S diagram, favoring an equilibrium $^1A_{1g}$ state, rather than a $^5T_{2g}$ state.

The strong interplay between the electronic, spin and steric degrees of freedom make for exceptionally interesting dynamical behavior when $\text{Fe}[\text{py}_3\text{tren}]^{2+}$ is photo-excited. The molecule must accommodate an excess quantum of electromagnetic energy and ultimately dissipate it. The strong coupling between the various degrees of freedom means there is facile energy transduction between different modalities. Observing the intermediate, transient states of the molecule after excitation sheds light on these molecular energy transduction mechanisms and provides insight into similar processes involved in other photo-activated chemical and biological processes.

4.3 Excited-State Dynamics of $\text{Fe}[\text{py}_3\text{tren}]^{2+}$

The fundamental question regarding the dynamical evolution of transition metal complexes is what are the excitation and relaxation pathways for these molecules—what does introducing energy do to the system, where does it go and what is the nature of the different energy transduction mechanisms involved in dissipating it?

Each degree of freedom involved in the excited-state evolution of $\text{Fe}[\text{py}_3\text{tren}]^{2+}$ has a natural time scale. The rate at which structural changes can proceed is set by the periods of the available stretching and bending modes of the molecule. Electronic and spin dynamics, however, can occur almost instantaneously, and are limited by the alacrity with which electrons re-organize to accommodate a morphing energy landscape. By understanding the interplay between the electronic, steric and spin degrees of freedom, the nature of the excited-state evolution of the molecule can be unraveled.

Pump-probe techniques allow for energy deposition in a controlled manner (e.g., amount of energy, excitation wavelength and duration of excitation) while making observations on the system as it evolves after excitation, allowing both coherent and incoherent pathways to be observed. Optical pump-probe spectroscopy provides access to electronic dynamics and spin dynamics of appropriately prepared samples

[SKC92,XS89]. X-ray pump-probe techniques complete the picture by providing a means to observe structural dynamics of the system as it evolves after excitation. A complete picture of the dynamics and relaxation pathway of the system can be sewn together from these complementary measurements; a schedule of events can be assembled to see what impact deposited energy has on a molecule as it courses its way through the system.

The Problem

What is understood about the excited-state evolution of $\text{Fe}[\text{py}_3\text{tren}]^{2+}$ is illustrated in Figure 4.6. In its ground state, the d-shell of $\text{Fe}[\text{py}_3\text{tren}]^{2+}$ is occupied in a low-spin configuration with all six electrons paired. Absorption of a 3.1eV photon by one of these d-electrons, promotes it to an anti-bonding orbital that is in physical proximity to the ligands in what is termed as a metal-to-ligand charge transfer (MLCT)—there is a spatial re-organization of the electron density distribution as well as an increase in the electron energy. This initial excited-state is short-lived. Within 500fs, the transferred electron energetically and spatially relaxes back to the iron d-shell, but returns to a different electronic configuration. The preceding dynamics have altered the molecular system to energetically favor electronic occupation of the d-shell in a high-spin configuration.

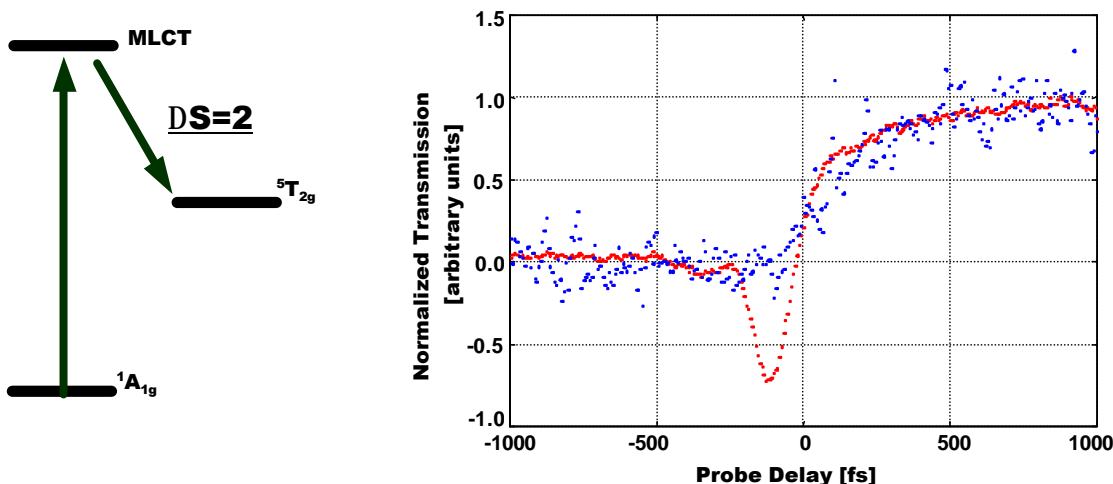


Figure 4.6: Excited-state dynamics of $\text{Fe}[\text{py}_3\text{tren}]^{2+}$. Upon photo-excitation from a low-spin ground state to a metal-to-ligand charge transfer state, the molecule quickly relaxes to a long-lived high-spin state. The differences between optical measurements made on solid- (blue dots) and solution-state (red dots) samples are attributed to different electron localization rates in the ligand due to solvent (or lack of) effects.

An interesting difference observed between the time-resolved optical absorption traces of the $\text{Fe}[\text{py}_3\text{tren}]^{2+}$ in solution and in the solid-state are shown in Figure 4.6. Each time-resolved trace was taken with 400nm pump and probe pulses of crossed polarization. Pulse durations of $\sim 85\text{fs}$ were used. The evolution of the molecule in solution exhibits a strong excited-state absorption—the sample transmission immediately drops—following excitation. The transmission of the solid sample, however, simply increases until it reaches its final state.

The formation of the final state takes the same amount of time for the molecule in solid state and in solution. The strong excited-state absorption is most likely due to the role the solvent plays in determining the early evolution of the complex as the electron is launched into the ligands and localizes on a particular ligand. The delayed-onset of increased sample transmission provides a sense of the time-response required for solvent environment to react to the change in electronic density of $\text{Fe}[\text{py}_3\text{tren}]^{2+}$ due to the MLCT transition. The electron remains delocalized among the ligands until solvent molecules can respond to break symmetry, forcing the electron to localize on a particular ligand and form a dipole. In solid-state $\text{Fe}[\text{py}_3\text{tren}]^{2+}$, the lack of an excited-state absorption feature is interpreted to be an instantaneous formation of a dipole as electron localizes on a ligand following excitation due to a highly anisotropic and dense local environment. Detailed studies of solvent effects on localization times and the early evolution of transition metal complexes have been performed on ruthenium(II) tris-(2,2'-bipyridine) [Yeh00].

The chain of events that gives rise to the ${}^1\text{A}_{1g} \rightarrow {}^5\text{T}_{2g}$ spin-crossover transition, however, is unclear. How does the interplay of electronic and steric re-organization conspire to allow a $\Delta S=2$ change in spin state of $\text{Fe}[\text{py}_3\text{tren}]^{2+}$ by simple photo-excitation, defying the need to conserve angular momentum? Clearly, a non-adiabatic transition is required. What role, then, does the atomic structure play?

Evidence from static x-ray spectroscopy suggests dynamics in the atomic structure do play a role: a steric distortion associated with formation of the photo-induced high-spin state is observed. The cage formed by the first coordination shell of nitrogen atoms around the iron distends by 10% in the $^5T_{2g}$ state [LSL⁺00]. However, it is not clear if the bond dilation results from a simple expansion or if the cage actually twists before finally settling into a symmetrical expansion as caricatured in Figure 4.7. It is also unclear if the structural changes are an artifact of the newly formed high-spin state or if a structural distortion drives the transition to a high-spin state for energetic stability. On a much longer time-scale, the high-spin state decays; the molecule returns to its low-spin state and the first coordination shell contracts to its original bond lengths.

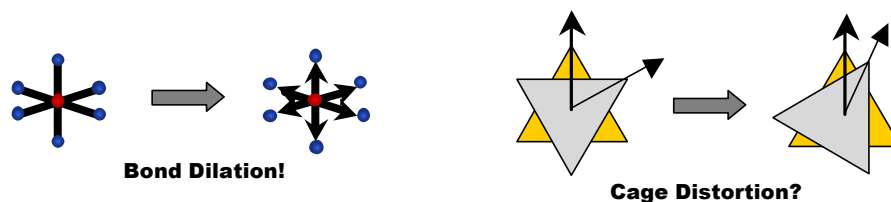


Figure 4.7: A bond dilation of the first-ordination shell of nitrogen atoms is associated with the formation of the $^5T_{2g}$ state and observed in static measurements where the sample is cryogenically frozen to extend the lifetime of the high-spin state. Since the formation of the high-spin state is complete in less than 500fs, the nature of the structural distortion and its relation to the spin-crossover of the molecule is poorly understood.

Possible Scenarios

Evidence suggests that different pathways can give rise to the spin-crossover behavior observed in $\text{Fe}[\text{py}_3\text{tren}]^{2+}$. High-spin analogs synthesized by the McCusker group at Michigan State University demonstrate structural distortions in the ligand cage give preference to a high-spin ground state. As presented in Figure 4.8, $\text{Fe}[\text{py}_3\text{tren}]^{2+}$ are synthesized with methyl groups bonded to the pyridine rings to form $\text{Fe}[\text{Me-py}_3\text{tren}]^{2+}$. To accommodate the addition methyl groups, the iron-nitrogen bonds associated with the pyridine bonds are stretched by 10%. The methylated version of $\text{Fe}[\text{py}_3\text{tren}]^{2+}$ has a high-spin $^5T_{2g}$ state as its equilibrium electronic ground state configuration. The ligand-field splitting energy of the $\text{Fe}[\text{py}_3\text{tren}]^{2+}$ is apparently close enough to the crossover threshold indicated on the T-S diagram of Figure 4.5, that this distortion to half the bonds

in first coordination shell is enough for energetic stability to favor a high-spin ground state.

Under photo-excitation, it is conceivable that as an electron localizes to a particular ligand, the dipole it forms polarizes the complex, forcing a structural distortion that lowers the ligand-field splitting energy sufficiently for $\text{Fe}[\text{py}_3\text{tren}]^{2+}$ to favor a high-spin state as the electron relaxes back to the iron center. In this scenario, a structural distortion drives the spin-crossover behavior of the molecule.

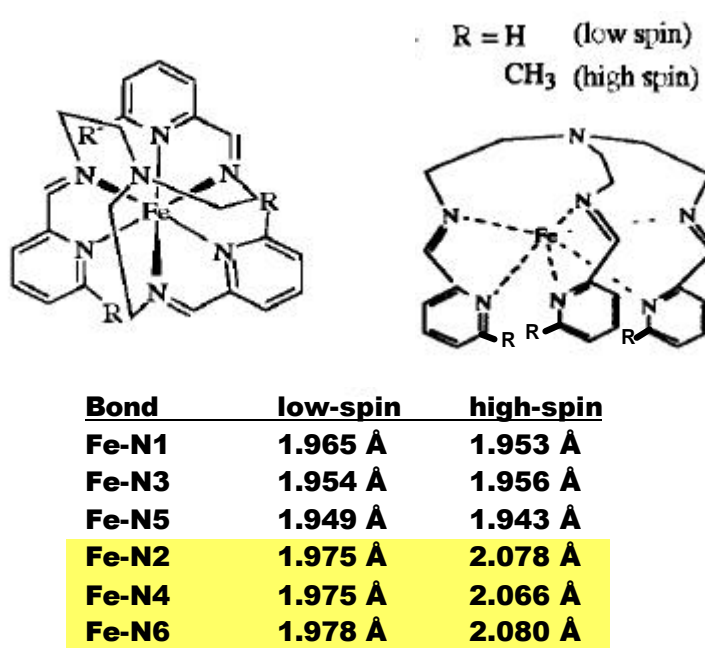


Figure 4.8: A high-spin analog of $\text{Fe}[\text{py}_3\text{tren}](\text{PF}_6)_2$, $\text{Fe}[\text{Me-py}_3\text{tren}](\text{PF}_6)_2$ has a synthetically distorted ligand cage with three of the six bonds lengthened by 10%. This provides a clue that a dipole-induced structural distortion may give energetic preference to a high-spin state. It also suggests that the ligand-field splitting strength of $\text{Fe}[\text{py}_3\text{tren}]^{2+}$ is near the crossover threshold for d^6 systems. Measurements were performed at the Chemistry Department Crystallography Facility at the University of California, Berkeley.

In contrast, electronic dynamics can also give rise to a transient high-spin state that, in turn, demands a distended first-coordination shell for stability. As schematically illustrated in Figure 4.9, $\text{Fe}[\text{py}_3\text{tren}]^{2+}$ starts in a low-spin $^1A_{1g}$ state and ultimately evolves into a high-spin $^5T_{2g}$ state. The nature of the intermediate electronic configuration in the MLCT state is unknown. A reasonable approach is to consider a

photo-excited $\text{Fe}[\text{py}_3\text{tren}]^{2+}$ molecule in a MLCT state to be an equivalent Fe^{3+} system [MM00]. In this oxidation state, two ground states are possible, a low-spin ${}^2\text{T}_{2g}$ state and a high spin ${}^6\text{A}_{1g}$ state. If the ligand-field splitting strength is weak, ${}^6\text{A}_{1g}$ state is energetically favored and the spin-crossover occurs due to electronic re-organization. Bond dilation then follows to ensure energetic stability [FH00,GC94]. The ${}^5\text{T}_{2g}$ state results when the excited electron relaxes back to the iron d-shell perturbed by an already distended ligand cage.

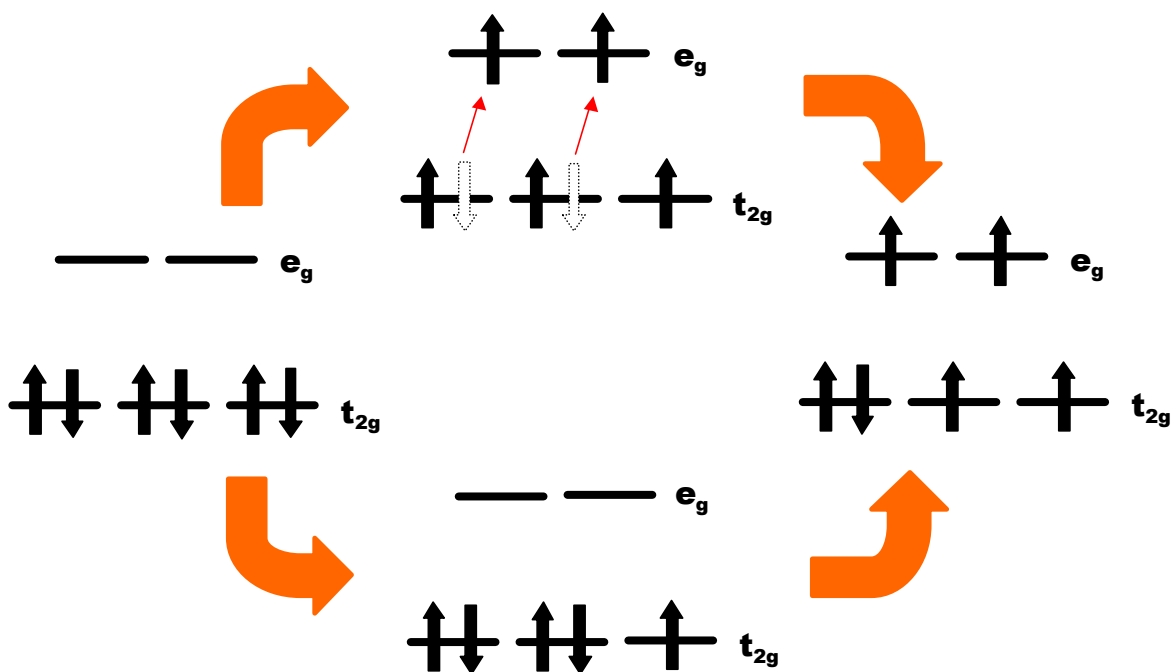


Figure 4.9: Electronic dynamics may give rise to spin-flip in MLCT state, prior to any structural changes in the $\text{Fe}[\text{py}_3\text{tren}]^{2+}$. In the MLCT state, the molecule can be considered an transient Fe^{3+} complex, a d^5 system with ${}^6\text{A}_{1g}$ and ${}^2\text{T}_{2g}$ as possible electronic configurations. If the high-spin ${}^6\text{A}_{1g}$ state is preferred upon photo-excitation, then the structural distortions that follow are to stabilize the new high-spin state.

A quick examination of T-S diagrams for d^6 and d^5 systems gives further credence to this scenario. Presented side-by-side in Figure 4.10, the ligand-field splitting strength required to maintain a low-spin configuration for a d^5 system is much higher than for the d^6 system. Though the exact ligand-field splitting strength seen by the Fe^{2+} ion cannot be assumed to remain unchanged under photon excitation, the qualitative features of the

T-S diagrams for Fe^{2+} and Fe^{3+} octahedral complexes and the relative proximity of the $\text{Fe}[\text{py}_3\text{tren}]^{2+}$ ligand-field splitting strength to the crossover threshold (inferred from the synthesized high-spin molecule) do not preclude this scenario as a reasonable relaxation pathway.

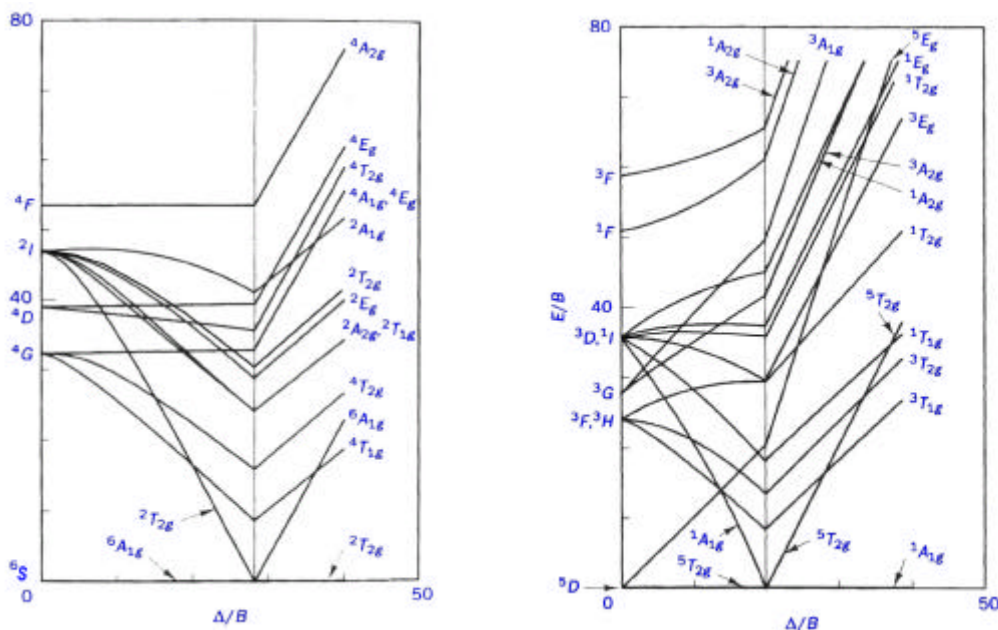


Figure 4.10: Tanabe-Sugano diagrams for d^5 and d^6 systems show that if a d^6 system does have a small enough ligand-field splitting energy, instantaneous removal of a d-electron to produce a d^5 system may yield a spin-flip.

Ultimately, the most exact means of determining the relaxation pathway for photo-excited $\text{Fe}[\text{py}_3\text{tren}]^{2+}$ is to perform time-resolved measurements to determine the time-scale for the development of structural changes, electronic re-organization and change in spin-state. The time-resolved optical transmission data presented provides a 500fs time-scale for the formation of a long-lived high-spin state. Optical dichroic measurements to monitor spin-states of $\text{Fe}[\text{py}_3\text{tren}]^{2+}$ could be performed if enantiomerically pure samples can be prepared. Unfortunately, consultation with experts in inorganic synthesis has established that the process could not be easily performed. With the recent development of tunable ultrashort pulse x-ray sources, the ability to monitor atomic structural changes local to a specific target atom is, however, accessible. To observe transient distortions in

the ligand cage surrounding the iron ion, time-resolved x-ray absorption measurements can be designed and performed.

4.4 Feasibility Calculations for Optical Pump/X-ray Probe Measurements

Due to the limited x-ray flux produced by current ultrashort-pulse x-ray sources, it is important to assess the experimental feasibility of a measurement. An assessment of the number of photons required to clearly resolve a physical process and the data acquisition time required to detect those photons can be made based on expectations of changes in signal amplitude estimated from empirical or computational results.

A general expression for calculating the number of x-ray photons required to see a signal with a chosen signal-to-noise ratio (SNR) is given by equation (4.1).

$$N_{xray} \approx \left[\frac{SNR}{\exp\left\{\frac{-s_u Nd}{2}\right\} [\Delta S F N d]} \right]^2 \quad (4.1)$$

The SNR is simply a ratio; a unity SNR means the signal is of the same amplitude as the fluctuations of the noise floor of the measurement. The other parameters are

s_u : unexcited x-ray absorption cross-section at the probe wavelength,

ΔS : the change in x-ray absorption cross-section at the probe wavelength,

N : the number density of the sample,

d : the thickness of the sample.

F : the sample photolysis—the fraction of the sample that is excited; F ranges from zero to unity. For optical excitation, sample photolysis can be computed with equation 4.2.

$$F = \frac{f s_{opt}}{d} \int_{sample} J(z) dz = \frac{J_0 f}{N d} [1 - \exp\{-s_{opt} N d\}] \quad (4.2)$$

Equation 4.2 accounts for the sample absorption of photons according to the Beer-Lambert law with

- \mathbf{s}_{opt} : the photo-absorption cross-section at the excitation wavelength,
- \mathbf{f} : the quantum efficiency of the absorption process,
- J_o : the fluence impinging on the sample in units of photons per unit area.

A complementary expression to calculate the SNR for given x-ray photon flux is given by equation 4.3.

$$SNR = \frac{I_0 \exp\{-\mathbf{s}_e FNd - \mathbf{s}_u (1-F)Nd\} - I_0 \exp\{-\mathbf{s}_u Nd\}}{I_0^{1/2} \exp\left\{\frac{-\mathbf{s}_e FNd - \mathbf{s}_u (1-F)Nd}{2}\right\}} \quad (4.3)$$

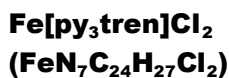
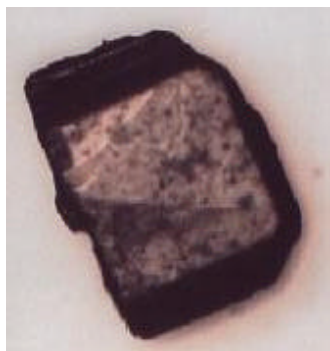
$$\approx I_0^{1/2} \exp\left\{\frac{-\mathbf{s}_u Nd}{2}\right\} [\Delta \mathbf{s} FNd]$$

I_o is the number of x-ray photons impinging on the sample and \mathbf{s}_e is the excited state x-ray absorption cross-section at the probe wavelength, thus $\mathbf{Ds} = \mathbf{s}_e - \mathbf{s}_u$. The numerator is composed of the differential signal measured; the denominator is the shot noise calculated as the square-root of the number of photons measured at the detector. With these expressions, it is possible to design and optimize a transmission pump-probe experiment and assess its feasibility.

For $\text{Fe}[\text{py}_3\text{tren}]^{2+}$, the experimental parameters can be taken from static optical spectra of the sample and anticipated shifts in x-ray spectroscopic features detailed in the literature [LSL⁺00, RGG⁺92] or measured empirically. As an example, a set of calculations to establish the experimental parameters to measure an x-ray absorption edge shift on the iron L-edge for $\text{Fe}[\text{py}_3\text{tren}]\text{Cl}_2$ —a molecular crystal of $\text{Fe}[\text{py}_3\text{tren}]^{2+}$ where a Cl_2^{-2} counter-ion is used form a salt—is presented.

As with all optimizations, experimental design is an iterative process. The process begins with assembling data regarding the optical and physical properties of the

sample, the static x-ray properties of the sample and an estimate of the change—either from calculation or empirical measurement—of the x-ray feature to be measured. For $\text{Fe}[\text{py}_3\text{tren}]\text{Cl}_2$, this is presented below in Figure 4.11.



$a = 13.346\text{Å}$ $a = 90$
 $b = 13.346\text{Å}$ $b = 90$
 $c = 18.201\text{Å}$ $g = 120$

$P6_3$ space group

$r = 1.401\text{g/cm}^3$

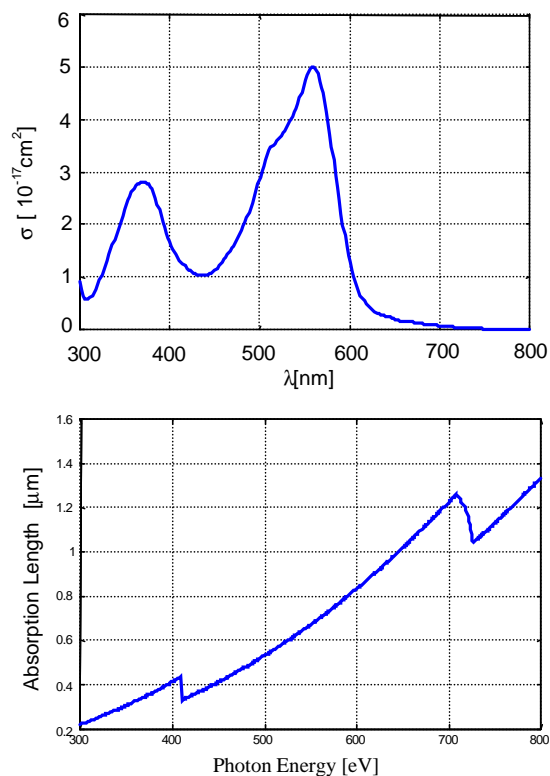


Figure 4.11: Physical properties of $\text{Fe}[\text{py}_3\text{tren}]\text{Cl}_2$ taken from crystallographic analysis, optical absorption spectra and x-ray absorption length in the soft x-ray region (from www-cxro.lbl.gov) are used in computing experimental feasibility for time-resolved x-ray experiments. Structural determination was performed at the Chemistry Department Crystallography Facility at the University of California, Berkeley.

From the data assembled, sample photolysis a can be computed as in Figure 4.12. A fluence of a single photon per molecule at the surface of the sample is assumed to avoid complicating nonlinear effects such as two-photon absorption processes.

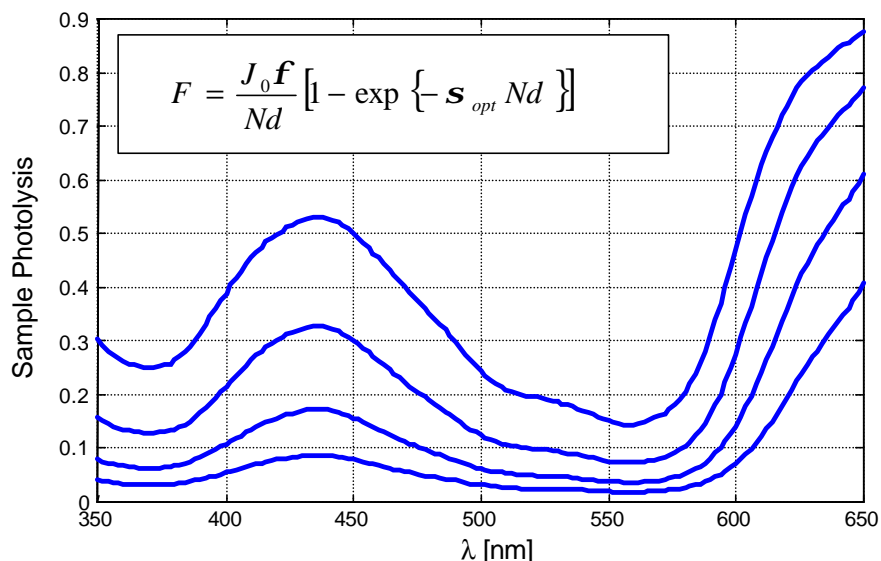


Figure 4.12: A family of sample photolysis curves computed for different sample thickness: 1 μm , 2 μm , 4 μm and 8 μm from high to low. Sample photolysis is an easy computation to perform and provides some sense of experimental feasibility, especially if only low photolysis levels are achievable. High-sample photolysis, however, does not necessarily imply a low-number of x-ray photons will be required to resolve features; it may only imply the sample is too thin.

Ultimately, maximum optical pump fluences and achievable sample photolysis levels that avoid nonlinear effects should be derived experimentally from optical pump-probe measurements and may often differ from calculation due to variation in sample preparation.

For example, single-wavelength pump-probe traces of solid-state samples of $\text{Fe}[\text{py}_3\text{tren}]\text{Cl}_2$ for different excitation fluences are presented in Figure 4.13. Crystals of $\sim 3\mu\text{m}$ thickness were prepared with a spin-coating technique on a microscope cover glass slide. Pump and probe pulses centered at 385nm were generated from 65fs, 790nm pulses extracted from a Ti:sapphire-based CPA system and doubled in a 1mm thick BBO crystal. The pump and probe pulses are cross-polarized to prevent measurement artifacts and brought to a focus with a 100 μm waist. The pump pulse energy was adjusted using graded neutral density filters. The data are fit with a single exponential with a characteristic rise-time of 350fs. The measurements suggest that a reasonable fraction,

nearly 20%, of the sample can be photo-excited without obviously damaging the sample or initiating nonlinear behavior.

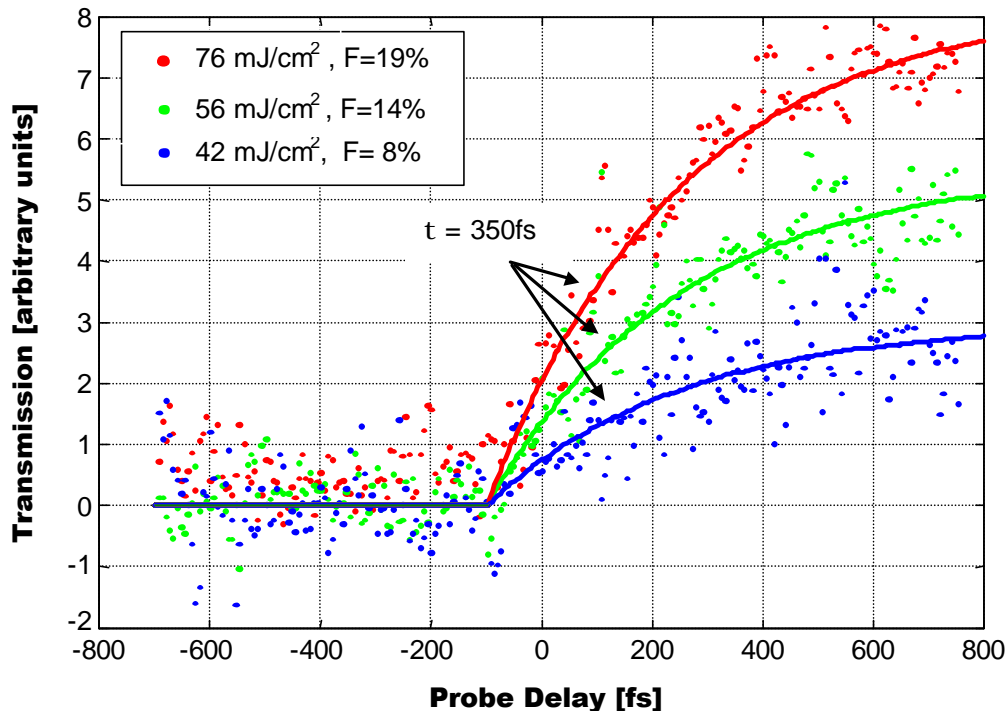


Figure 4.13: Single-wavelength pump-probe traces for $\sim 3\mu\text{m}$ thick crystals of $\text{Fe}[\text{py}_3\text{tren}]\text{Cl}_2$ at different excitation fluences with calculated sample photolysis levels. The traces are all fit to a single exponential with a characteristic rise-time of 350fs.

X-ray data from the Center for X-ray Optics (www-cxro.lbl.gov) or the literature allow for computation of x-ray absorption cross-sections. In conjunction with the sample photolysis calculations, the number of x-ray photons required to resolve changes in the x-ray signature of the sample with a chosen resolution (SNR) can be computed. At this point, the optimization of different experimental parameters can be addressed. The following are constraints that are considered.

J_0 : optical fluence, set by one photon per molecule at surface

s_{opt} : optical cross-section. Constrained by the ability to generate a reasonable fluence at specific wavelengths; a pump spot large enough to overfill the x-ray spot diameter, usually = $150\mu\text{m}$, is needed.

N and d : these are dual parameters. For solution samples, the sample thickness, d , is generally fixed and the solution concentration, N , is varied. For solid samples, N is fixed, and d can be varied. The number of required x-ray photons for the experiment can be computed for a range of reasonable values and a search performed to find an optimum with other experimental parameters fixed. For solid-state Fe[py₃tren]Cl₂, Figure 4.14 presents such an optimization.

$S_{x\text{-ray}}$: x-ray absorption cross-section. Access to different photon energies is limited by the available bandwidth of the x-ray source. Tuning to different absorption edges provides different physical information—K-edge provides structural information, L-edge provides electronic information. Solvents and any other source of background x-ray absorption (e.g., ambient gas backfill) should be included in the calculation.

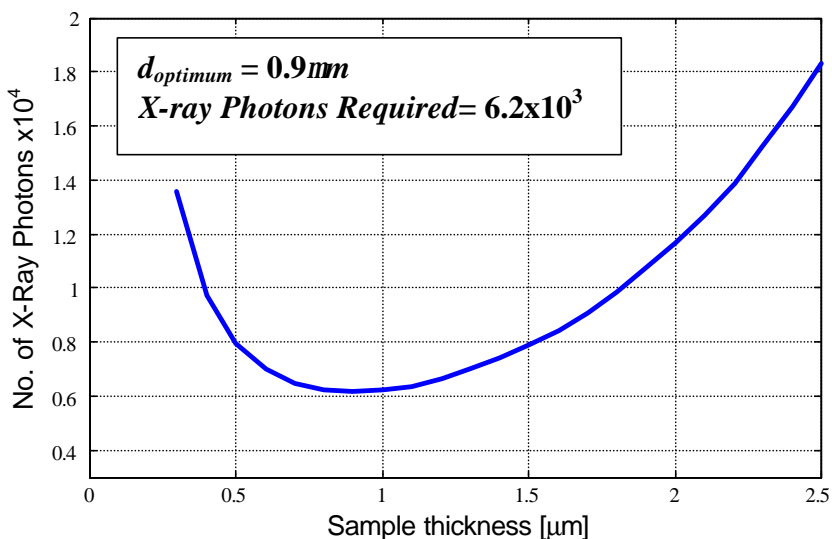


Figure 4.14: Optimization plot for sample thickness of Fe[py₃tren]Cl₂.

A tabulation of final values is presented in Table 4.1 for a time-resolved x-ray absorption experiment at the iron L-edge in a solid-state Fe[py₃tren]Cl₂ sample.

N	1.39×10^{21} molecules/cm ³ (2.31 M)
d_{sample}	$\sim 1 \mu\text{m}$
I_{pump}	400nm
$S_{optical}$	1.67×10^{-17} cm ²
J_o	0.030 J/cm ²
F	42%
DS_{x-ray}	100% at Fe L-edge (707eV)
N_{x-ray}	6.2×10^3 (SNR=10, unity detector efficiency)

Table 4.1: Final experimental parameters and expectations for a time-resolved x-ray absorption experiment on Fe[py₃tren]Cl₂ at the iron L-edge.

4.5 Experimental Considerations and Difficulties

Beyond the considerations made to assess feasibility, there are practical considerations needed to actually carry out the experiment—appropriate sample preparation, instrumentation and measurement modalities need all be considered.

With low x-ray flux as constraint, it is necessary to make measurements on solid density samples of Fe[py₃tren]Cl₂ at the Fe L-edge. The severe mismatch between the optical absorption length and the x-ray absorption length of Fe[py₃tren]Cl₂ near the Fe K-edge, one of several orders of magnitude, results in an imposing absorption background from the large fraction of unexcited sample probed in the measurement. At the iron L-edge, using a solution-state sample in a helium back-filled environment is prohibitive: near solid-densities are needed to afford reasonable data acquisition times and any solvent (or polymer matrix) absorbs strongly in the soft x-ray region near 700eV, overshadowing the iron x-ray features of interest. A 5 μm film of polypropylene, for example, absorbs nearly 90% of x-rays at 700eV.

To prepare a sample of optimal thickness required trials of many techniques. Native crystals of Fe[py₃tren]Cl₂ precipitate from solution in small bricks roughly 200 μm on a side. Initial attempts to apply *microtome* techniques, used to prepare thin samples for transmission electron microscopy samples, quickly revealed that Fe[py₃tren]Cl₂ is not

sturdy enough to survive of a cleaving process. A grinding procedure also met with failure. $\text{Fe}[\text{py}_3\text{tren}]\text{Cl}_2$ crystals of thickness below $15\mu\text{m}$ are not self-supporting—they simply crumbled.

To allow for a sample of thickness below $10\mu\text{m}$, a reasonable support structure was employed. The support material must be mechanically hardy and x-ray transparent. Ideally, it would also be optically transparent and possess thermal properties to allow it to dissipate heat from the sample. The preferred option is thin-film chemical vapor deposition (CVD) diamond. Diamond has ideal mechanical and thermal properties. Films of thickness below $0.5\mu\text{m}$ can be fabricated routinely on silicon substrates¹¹. Unfortunately, processing the diamond-coated silicon wafers to yield small windows of self-standing, thin-film diamond is still a developmental endeavor, and not routinely achievable¹².

Silicon nitride is commonly used as an x-ray transparent window material used at synchrotron facilities and is known for high mechanical integrity. Windows of specific dimensions are relatively easy to fabricate and windows of stock dimensions are commercially available¹³. The process for fabricating windows is similar to the process described for CVD diamond windows. Silicon nitride of chosen thickness is grown on silicon wafers through a nitrating process, then back-etched to provide small, self-standing windows which can span $100\mu\text{m}$ to 5mm on an edge as pictured in Figure 4.15.

¹¹CVD diamond on silicon substrate was fabricated by PIDiamond Inc., Santa Clara, CA. http://www.p1diamond.com/cvd_diam.html.

¹²A developmental run was performed with Peter Anastasi at Silson Ltd., Northampton, England with poor results. Others interested in developing a CVD diamond window process include the Structure Probe, Inc. Supplies, West Chester, PA., and the Lawrence Livermore National Laboratory Center for Microtechnology.

¹³ Stock silicon nitride windows can be ordered from Structure Probe, Inc. Supplies, West Chester, PA. For more information, see <http://www.2spi.com/catalog/instruments/silicon-nitride.shtml>.

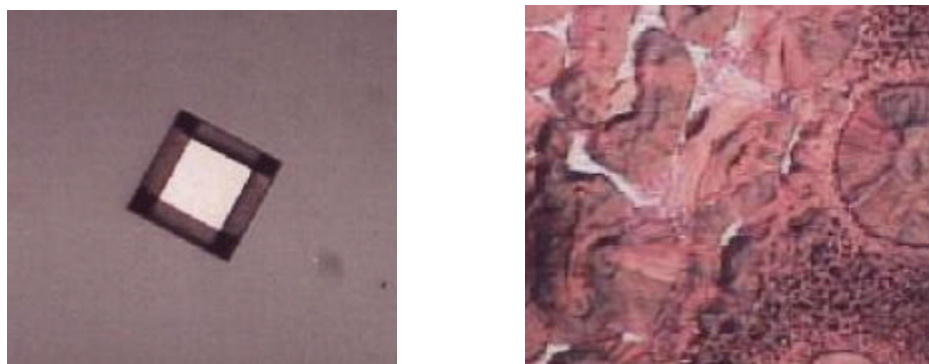


Figure 4.15: The left is an image of a bare silicon nitride window taken from the back-etched side of the silicon frame. The image to the right is a silicon nitride window coated with $\text{Fe}[\text{py}_3\text{tren}]\text{Cl}_2$. Crystals of $\text{Fe}[\text{py}_3\text{tren}]\text{Cl}_2$ were dissolved in ethanol and deposited on a spinning window to provide better sample uniformity as solvent evaporated.

$\text{Fe}[\text{py}_3\text{tren}]\text{Cl}_2$ samples were deposited on $0.2\mu\text{m}$ thick, $250\mu\text{m}$ windows by dissolving molecular crystals in a solvent, coating the silicon nitride windows with the solution and allowing the solvent to evaporate. With appropriate solute concentrations, sample coatings of $1\mu\text{m}$ to $10\mu\text{m}$ were reliably produced using a spin-coating process.

Initial experiments showed promise, but closer inspection of the data and the sample revealed that though the silicon nitride is mechanical hardy, it has extremely poor thermal conductivity. The window was unable to dissipate the energy supplied by the laser pulse and melted the sample in the region of the free-standing window as shown in Figure 2.2. Beyond the window, the thick silicon frame provided the necessary sink to prevent the $\text{Fe}[\text{py}_3\text{tren}]\text{Cl}_2$ sample from melting. Observed edge-shifts in the x-ray spectra were interpreted as a temperature-induced spin-crossover transition observed in other Fe(II) system [RGG⁺92].

To address the excessive thermal load, a gas-flow chamber was designed to flow helium across the sample in hopes of transporting heat away from the sample through convection. This apparatus is displayed in Figure 4.16. Unfortunately, it failed to provide a sufficient amount of thermal relief from the sample to prevent the samples from melting.



Figure 4.16: Helium flow chambers used to transport heat from samples. The chamber is composed of two Kwik-Flange[®] blanks. Each flange has a series of three conical holes cut into its face to facilitate non-collinear crossing of x-ray and laser beams on the sample. The holes are sealed vacuum-tight using silicon-nitride windows—the upstream flange bearing windows covered with Fe[py₃tren]Cl₂ samples, the downstream flange bearing bare windows. Helium flow through the chamber is facilitated through Swagelok[®] fitting soldered to the downstream flange. Opposing windows on up- and downstream flanges are aligned to allow transmission of x-rays.

To enhance the thermal conductivity of the sample support, silicon nitride windows were vacuum-coated with a 0.5 μ m layer of aluminum to provide a highly thermal conductive contact for the sample. Laser experiments demonstrated that the deposited Fe[py₃tren]Cl₂ samples survived with this preparation under fluence conditions a factor of three higher than standard operating conditions.

Under x-ray illumination, however, radiation damage appeared. Initial experiments were performed in a white-light transmission geometry where the sample was located between the slits and the soft x-ray spectrometer as depicted in Figure 4.17. A pair of silicon mirrors in the monochromator chamber reflects the incoming x-rays by total external reflection. Set at the correct angle, the reflection cuts off x-ray wavelengths beyond 1keV. The sample is placed in the resultant pink beam. The x-ray photons transmitted through the sample are dispersed and collected in parallel on a CCD detection system.

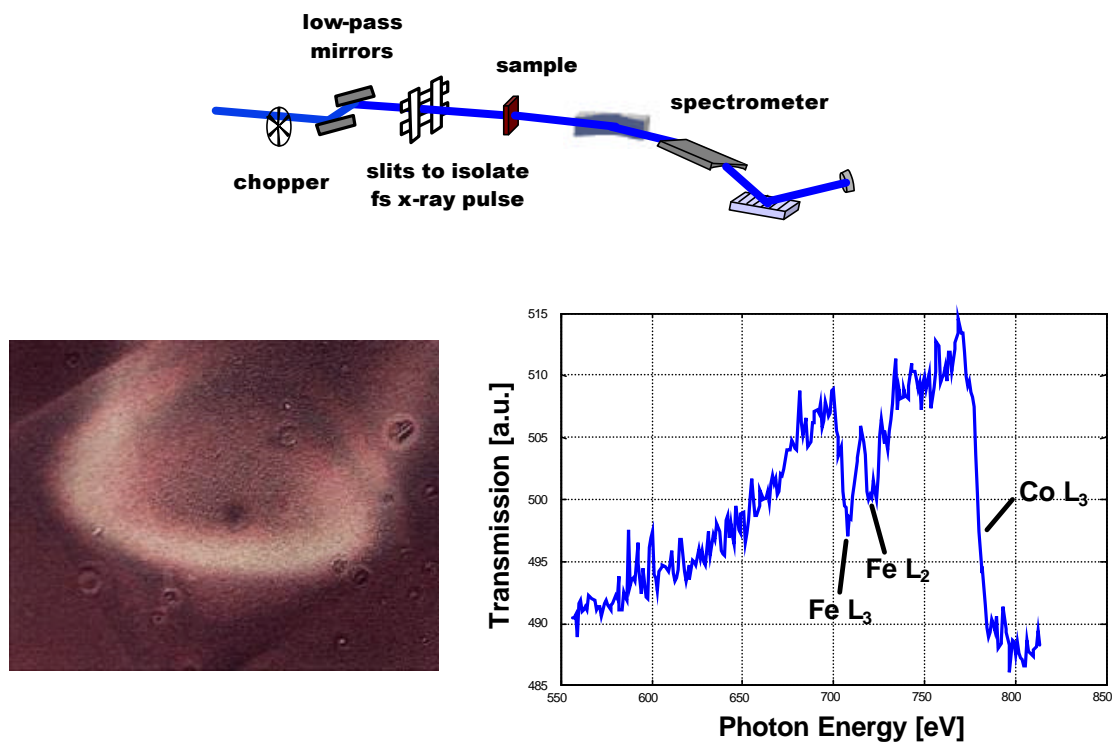


Figure 4.17: Static x-ray absorption spectrum of $\text{Fe}[\text{py}_3\text{tren}]\text{Cl}_2$ on aluminized silicon nitride windows. Two iron L-edges from the sample and a Co L-edge from a reference foil are featured. The measurement was performed in a white-light transmission geometry and the dispersed spectrum was collected on a CCD camera operating at 1kHz repetition rate. A silhouette of the transmitting window can be seen through the $\text{Fe}[\text{py}_3\text{tren}]\text{Cl}_2$ in the lower-left picture. Sample damage due to excess photon is evident as discoloration of the crystalline sample.

To further reduce the number of excess x-ray photons on the sample, the soft-x-ray spectrometer was modified to mount the sample in the image plane of the dispersed spectrum after the grating. Now, only monochromatic x-rays relevant to the measurement would be incident on the sample. A static x-ray spectrum of the sample was acquired by scanning the grating and detecting the x-rays transmitted through (and apertured by) the sample window on an avalanche photodiode as shown in Figure 4.18.

Even under these most cautious experimental conditions, with monochromatic light used on the sample at photon counting rates of 200 counts/second, x-ray damage was still observed as a decrease in magnitude of absorption edge with each scanning cycle. The x-ray damage physically appears as a thin stripe corresponding to the horizontally focused,

dispersed x-ray spectra on the sample shown in Figure 4.17. Unfortunately, this development confirmed that an optical pump-x-ray probe experiment on $\text{Fe}[\text{py}_3\text{tren}]^{2+}$ under even the most favorable of conditions is currently not experimentally possible.

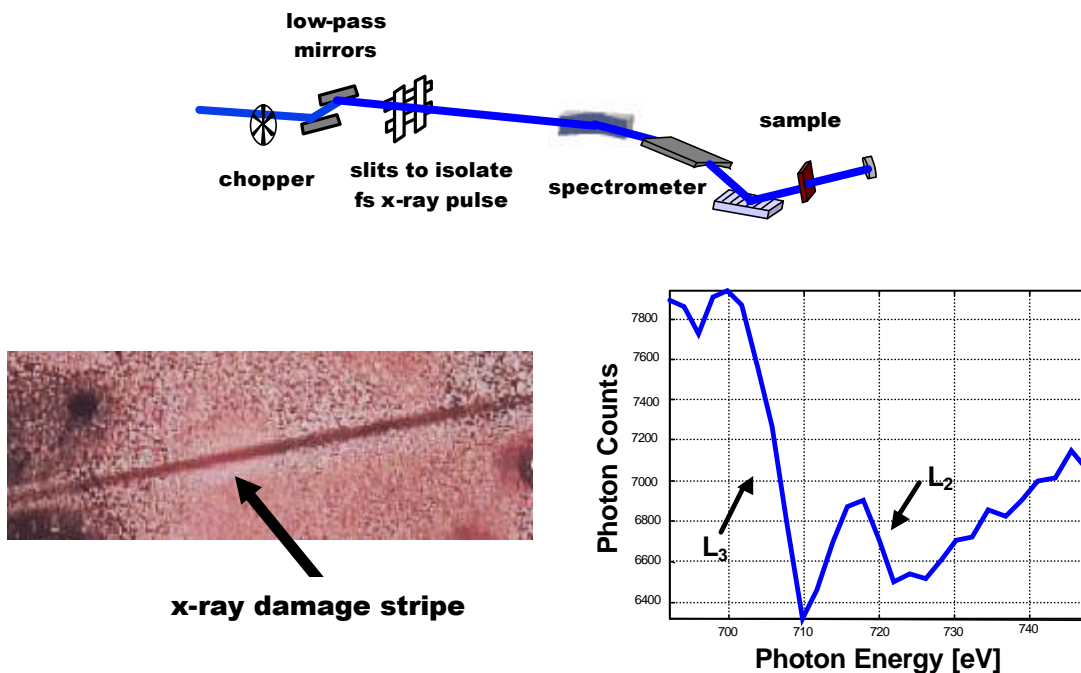


Figure 4.18: An absorption spectrum of the $\text{Fe}[\text{py}_3\text{tren}]\text{Cl}_2$ on an aluminized silicon nitride window taken with the sample in the image plane of the spectrometer. Two iron L-edges of the $\text{Fe}[\text{py}_3\text{tren}]\text{Cl}_2$ molecules are featured. A thin damage stripe associated with the focused, dispersed x-rays incident on the sample is evident in the microscope image.

5 CONSIDERATIONS FOR FUTURE WORK

The continued viability of ultrafast x-ray spectroscopy as a new field of research requires serious consideration of near- and long-term goals. A great deal of focus in the field currently revolves around the proposal and design of high-end, ultrashort x-ray pulse sources [Nap02]; the successful completion of these sources is projected to be in 10 to 15 years. In the interim, as a matter of practicality, there are many technical obstacles to overcome before time-resolved x-ray measurements can be routinely performed on even simple, well-characterized model systems. Also as a matter of practicality, long-term goals should include the consideration of scientifically interesting experiments—beyond simple observation experiments—if ultrafast x-ray spectroscopy is to become a relevant, unique and necessary experimental tool for the greater scientific community.

Near-term goals should focus on technical issues required to make successful time-resolved x-ray measurements a routine procedure. Continued funding for current research efforts and for the development of future ultrashort x-ray pulse generation facilities requires results from currently available ultrashort x-ray pulse sources; the personal sanity of researchers involved in the establishment of this field demands them as well. The technical hurdle highlighted in this thesis is sample survivability. A prudent choice of sample, of course, presents an immediate solution, but limits the scope of

investigation to a small selection of systems. More general solutions to these problems can be addressed through different elements of the experiment—source, sample preparation and detection chain—to allow for the study of a broader range of chemical and material systems.

A difficulty with machine-based sources is that x-ray repetition rates are in excess of data acquisition rates. Current machine-based sources generally operate at high-repetition rates and use integrating detectors to perform static, averaging measurements. This poses a problem not only for sample survivability, but also detection of optically triggered events during normal operations. For example, the slicing source at the ALS produces femtosecond pulses at kilohertz repetition rates; the synchrotron, however, produces a continuous train of x-ray pulses at 500MHz. For a given data acquisition period, a sample needs to survive a barrage of x-ray photons four to five orders of magnitude greater than the ones detected, and detectors with fast recovery times need to be employed and appropriately gated to detect only desired events.

A means of matching the repetition rate of the source to the data acquisition rate needs to be developed that is less invasive than filling the machine with a special electron bunch fill pattern. As suggested in Chapter Two, well-designed mechanical choppers can provide some relief by severely modifying the x-ray duty cycle. Mechanical choppers, however, cannot easily isolate a single x-ray pulse, but rather admit a short train of pulses. Though this alleviates abuse to the sample due to excess x-ray flux, standard detectors still cannot be used in an integrating fashion. An ambitious solution is to develop a fast x-ray switch to physically gate x-ray pulses of utility. Physical processes, like the Bormann effect [DRB⁺01], have been demonstrated to gate x-ray pulses with reasonable efficiency. The added experimental complexity required to implement it, however, may preclude it as a useful option.

Sample preparation also warrants serious consideration. The underlying problem with optical pump-x-ray probe experiments is the large mismatch between the optical and x-ray photon absorption lengths in most materials and the dearth of x-ray photon flux

available at current ultrashort x-ray pulse sources. To make experiments feasible requires the appropriate tailoring of sample density or thickness to afford reasonable data acquisition times for complete data sets. Solid-state samples are required for soft x-ray investigation due to strong solvent x-ray absorption, and the solid-state is the native state for many interesting material systems. Issues common to those discussed in Chapter Four should be addressed—support structures with suitable mechanical strength, x-ray transparency and thermal relief, like CVD diamond windows, and a consistent means of sample fabrication and characterization should be developed. Adapting in-vacuum sample preparation techniques from surface science may also be useful for the development of alternate measurement modalities like total-electron and fluorescence yield—both of which obviate concerns associated with absorption length mismatches between excitation and probe wavelengths due to their surface sensitivity. Outreach to the broader material processing and fabrication community to bring in expertise will also allow connections to be forged with a broader community with fresh perspectives and ideas regarding scientific questions that can be addressed using time-resolved x-ray techniques.

In the long-term, experiments need to be proposed and developed for sources with higher x-ray flux specifications. The ability to resolve atomic re-arrangement on a physically-limiting time-scale is both the manacle and demonic charm of ultrafast x-ray techniques. There will always be a temptation for researchers to make a career of serial “first observation” measurements regardless of whether or not those observations are meaningful. Ultrafast x-ray techniques, rather, should be considered a complement to other time-resolved techniques that provides unique, previously inaccessible insight into the dynamical evolution of a system.

A natural extension of this thesis is to continue work to experimentally determine the excitation and relaxation pathways of complex system that have function which follow from steric interactions. Due to current technical limitations, work will be limited to simple transition metal complexes and transition metal oxides. These model systems have interesting structural and electronic dynamics that can be simultaneously probed

with x-rays, and complemented with optical spectroscopic measurements. These well-characterized systems will also be useful to flesh out experimental complications that may arise in the course of developing instrumentation for more complex experiments.

More ambitious work should evolve to include fundamental studies of highly engineered, synthesized condensed-matter and material systems. Investigations of unusual states of matter and critical phenomena in materials to determine finite-size and reduced-dimensionality effects on the properties of many-body systems should be pursued. Liquid crystals exhibit a myriad of ordered states and novel melting phenomena in two-dimensions (a critical dimension where long-range order is not possible). Liquid crystal systems are currently being studied with x-rays using coherent scattering techniques [dOS03] and diffraction. Time-resolved x-ray measurements may provide information regarding structural dynamics that complements the information regarding fluctuations.

The field of ultrafast x-ray spectroscopy is in its nascency. The capability to probe atomic re-arrangement on the time-scales on which atoms can move in molecular and condensed-matter systems is unique and necessary for the progress of science. Though there are still many technical hurdles to overcome before ultrafast x-ray techniques can be considered a standard spectroscopic tool, with continued development, it promises to be an important gateway to future scientific innovation.

REFERENCES

- [AdG⁺91] M. Abbate, F.M.F. de Groot, J.C. Fuggle, Y.J. Ma, C.T. Chen, F. Sette, A. Fujimori, Y. Ueda and K. Kosuge. Soft-x-ray-absorption studies of the electronic-structure changes through the VO₂ phase transition. *Physical Review B*, 43:7263, March 1991.
- [Att99] D.T. Attwood. *Soft x-rays and extreme ultraviolet radiation : principles and applications*. Cambridge University Press, New York, New York, 1999.
- [BC64] B.W. Batterman and H. Cole. Dynamical Diffraction of X Rays by Perfect Crystals. *Reviews of Modern Physics*, 36:681, July 1964.
- [BDM⁺98] S. Backus, C.G. Durfee III, M.M. Murnane and H.C. Kapteyn. High power ultrafast lasers. *Review of Scientific Instruments*. 69:1207, March 1998.
- [Bar62] C.S. Barrett. *Structure of Metals*. McGraw-Hill, New York, NY. 1952.
- [BL03] M.V. Bennett and J.R. Long. New Cyanometalate Building Units: Synthesis and Characterization of [Re(CN)₇]³⁻ and [Re(CN)₈]³⁻. *Journal of the American Chemistry Society*. 125:2394, 2003.
- [CNS⁺98] G. Cerullo, M. Nisoli, S. Stagira and S. De Silvestri. Sub-8-fs pulses from an ultrabroadband optical parametric amplifier in the visible. *Optics Letters*, 23:1283, August 1998.
- [CSG⁺99] A.H. Chin, R.W. Schoenlein, T.E. Glover, P. Balling, W.P. Leemans and C.V. Shank. Ultrafast Structural Dynamics in InSb Probed by Time-Resolved X-Ray Diffraction. *Physical Review Letters*, 83:336, 1999.
- [CTS⁺01] A. Cavalleri, Cs. Tóth, C.W. Siders, J.A. Squier, F. Ráksi, P. Forget, and J.C. Kieffer. Femtosecond structural dynamics in VO₂ during an ultrafast solid-solid phase transition. *Physical Review Letters*, 87:237401, 2001.
- [Chi98] A.H. Chin. Ultrashort X-ray Pulse Science. Doctoral Thesis; University of California, Berkeley and Lawrence Berkeley National Laboratory; May 1998.
- [dOS03] W. H. de Jeu, B. I. Ostrovskii, and A. N. Shalaginov. Structure and fluctuations of smectic membranes. *Reviews of Modern Physics*, 75:181, February 2003.

- [DOE97] Report of the Basic Energy Sciences Advisory Committee Panel on D.O.E. Synchrotron Radiation Sources and Science. R. Birgeneau (Chair) and Z.-X. Chen (Vice-Chair). November 1997. Electronic access at <http://www-ssrl.slac.stanford.edu/lcls/papers/syncpanel.pdf>.
- [DRB⁺01] M.F. DeCamp, D.A. Reis, P.H. Bucksbaum, R. Clarke, R. Merlin, A. Cavalieri, E.M. Dufresne, D.A. Arms, A. Lindenberg, A. MacPhee and Z. Chang. Picosecond Switching of X-rays using the Boorman Effect. *Advanced Photon Source Activity Report*, 2001.
- [DWK02] S.E. Derenzo, M.J. Weber and M.K. Klintenberg. Temperature dependence of the fast, near-band-edge scintillation from CuI, HgI₂, PbI₂, ZnO:Ga and CdS:In. *Nuclear Instruments & Methods in Physics Research A*, 486:214, 2002.
- [FFY⁺02] T. Funk, S. Friedrich, A. Young, E. Arenholz and S.P. Cramer. Requirements for x-ray magnetic circular dichroism on paramagnetic biological systems and model compounds. *Review of Scientific Instruments*, 73:1649, March 2002.
- [FH00] B.N. Figgis and M.A. Hitchman. *Ligand Field Theory and Its Applications*. Wiley-VCH, New York, NY. 2000.
- [GC94] M. Gerloch and E.C. Constable. *Transition Metal Chemistry*. Wiley-VCH, New York, NY. 1994.
- [GGG00] P. Gutlich, Y. Garcia and H.A. Goodwin. Spin crossover phenomena in Fe(II) complexes. *Chemical Society Reviews*, 29:419, 2000.
- [HAC⁺pp] M.P. Hertlein, H. Adaniya, K. Cole, B. Feinberg, J. Maddi, M.H. Prior, R. Schriel and A. Belkacem. Electron correlation during the Auger cascade of potassium and argon after K-shell photoexcitation. *submitted for publication*.
- [Hau86] H.A. Haus. On the radiation from point charges. *American Journal of Physics*, 54:1126, December 1986.
- [Kit53] C. Kittel. *Introduction to solid state physics*. Wiley, New York, New York, 1953.
- [Kon90] J.A. Kong. *Electromagnetic wave theory*. Wiley, New York, New York, 1990.
- [KR74] G.J. Kruger and E.C. Reynhardt. New Investigation of the Structure of Trisacetylacetonatocobalt(III). *Acta Crystallographica B*, 30:822, 1974.

- [LSL⁺00] J.-J. Lee, H.-S. Sheu, C.-R. Lee, J.-M. Chen, J.-F. Lee, C.-C. Wang, C.-H. Huang and Y. Wang. X-ray Absorption Spectroscopic Studies on Light-Induced Excited Spin State Trapping of an Fe(II) Complex. *Journal of the American Chemical Society*, 122:5742, 2000.
- [MM00] J.E. Monat and J.K. McCusker. Femtosecond Excited-State Dynamics of an Iron(II) Polypyridyl Solar Cell Sensitizer Model. *Journal of the American Chemical Society*, 122:4092, 2000.
- [MWM⁺93] J.K. McCusker, K.N. Walda, D. Magda and D.N. Hendrickson. Picosecond Excited-State Dynamics in Octahedral Cobalt(III) Complexes: Intersystem Crossing versus Internal Conversion. *Inorganic Chemistry*, 32:394, 1993.
- [Mor91] M.A. Morrison. *Understanding More Quantum Physics: Quantum States of Atoms*. Prentice Hall, Englewood Cliffs, New Jersey, 1991.
- [Nap02] Workshop on New Opportunities in Ultrafast Science using X-rays, Napa, California, April 2002.
<http://www-esg.lbl.gov/esg/meetings/ultrafast/index.html>
- [PSR⁺98] B. Perman, V. Šrajer, Z. Ren, T.-Y. Teng, C. Pradervand, T. Ursby, D. Bourgeois, F. Schotte, M. Wulff, R. Kort, K. Hellingwerf and K. Moffat. Energy Transduction on the Nanosecond Time Scale: Early Structural Events in a Xanthopsin Photocycle. *Science*, 279:1946, March 1998.
- [RBW89] M.J.W. Rodwell, D.M. Bloom and K.J. Weingarten. Subpicosecond Laser Timing Stabilization. *IEEE Journal of Quantum Electronics*, 25:817, April 1989.
- [RGG⁺92] J.-A. Real, B. Gallois, Th. Granier, F. Suez-Panamá and J. Zarembowitch. Comparative Investigation of the Spin-Crossover Compounds Fe(btz)₂(NCS)₂ and Fe(phen)₂(NCS)₂ (Where btz = 2,2'-Bi-4,5-dihydrothiazine and phen = 1,10-Phenanthroline). Magnetic Properties and Thermal Dilatation Behavior and Crystal Structure of Fe(btz)₂(NCS)₂ at 293 and 130K. *Inorganic Chemistry*, 31:4972, 1992.
- [RRF⁺01] A. Rousse, C. Rischel, S. Fourmaux, I. Uschmann, S. Sebban, G. Grillon, Ph. Balcou, E. Förster, J.P. Geindre, P. Audebert, J.C. Gauthier and D. Hulin. Non-thermal melting in semiconductors measured at femtosecond resolution. *Nature*, 410:65, 2001.
- [RRG01] A. Rousse, C. Rischel and J.-C. Gauthier. Femtosecond x-ray crystallography. *Reviews of Modern Physics*, 73:17, January 2001.

- [RRU⁺97] C. Rischel, A. Rouse, I. Uschmann, P.-A. Albouy, J.-P. Geindre, P. Audebert, J.-C. Gauthier, E. Fröster, J.-L. Martin and A. Antonetti. Femtosecond time-resolved X-ray diffraction from laser-heated organic films. *Nature*, 390:490, December 1997.
- [RTH⁺00] E. Rotenberg, W. Theis, K. Horn and P. Gille. Quasicrystal valence bands in decagonal AlNiCo. *Nature*, 406:602, 2000.
- [RVW⁺01] I.K. Robinson, I.A. Vartanyants, G.J. Williams, M.A. Pfeifer and J.A. Pitney. Reconstruction of the Shapes of Gold Nanocrystals Using Coherent X-Ray Diffraction. *Physical Review Letters*, 87:195505, October 2001.
- [S-T⁺03] K. Sokolowski-Tinten, C. Blome, J. Blums, A. Cavalleri, C. Dietrich, A. Tarasevitch, I. Uschmann, E. Förster, M. Kammler, M. Horn-von-Hoegen and D. von der Linde. Femtosecond X-ray measurement of coherent lattice vibrations near the Lindemann stability limit. *Nature*, 422:287, March 2003.
- [SCC⁺00] R.W. Schoenlein, S. Chattopadhyay, H.H.W. Chong, T.E. Glover, P.A. Heimann, C.V. Shank, A.A. Zholents, and M.S. Zolotorev. Generation of Femtosecond Pulses of Synchrotron Radiation. *Science*, 287:2237, March 2000.
- [SCC⁺03] R.W. Schoenlein, A. Cavalleri, H.H.W. Chong, T.E. Glover, P.A. Heimann, A.A. Zholents, M.S. Zolotorev. Generation of Femtosecond Synchrotron Pulses: Performance and Characterization, *SYNCHROTRON RADIATION INSTRUMENTATION: Eighth International Conference on Synchrotron Radiation Instrumentation*, August 2003, Proceedings to be published.
- [SCG⁺99] R. Schoenlein, H. Chong, T.E. Glover, P. Heimann, A. Zholents, M. Zolotorev. Low signal FEL gain: measurement, simulation and analysis. *IEEE Proceedings of the 1999 Particle Accelerator Conference*, p. 2498-2500, 1999.
- [SKC92] J.B. Stark, W.H. Knox and D.S. Chemla. Femtosecond Circular Dichroism Study of Nonthermal Carrier Distributions in Two- and Zero-Dimensional Semiconductors. *Physical Review Letters*, 60:3080, 1992.
- [SLC⁺96] R.W. Schoenlein, W.P. Leemans, A.H. Chin, P. Volfbeyn, T.E. Glover, P. Balling, M. Zolotorev, K.-J. Kim, S. Chattopadhyay and C.V. Shank. Femtosecond X-ray Pulses at 0.4 Å Generated by 90° Thomson Scattering: A Tool for Probing the Structural Dynamics of Materials. *Science*, 274:236, October 1996.

- [Sto92] J. Stohr. *NEXAFS Spectroscopy*. Springer-Verlag, New York, New York, 1992.
- [TSW01] S. Techert, F. Schotte and M. Wulff. Picosecond X-Ray Diffraction Probed Transient Structural Changes in Organic Solids. *Physical Review Letters*, 86:2030, March 2001.
- [Teo86] B.K. Teo. *EXAFS : basic principles and data analysis*. Springer-Verlag, New York, New York, 1986.
- [V-S⁺03] A. Vila-Sanjurjo, et.al. X-ray crystal structures of the WT and a hyper-accurate ribosome from Escherichia coli. *Proceedings of National Academy of Science* 100:8682, 2003.
- [War69] B.E. Warren. *X-ray diffraction*. Addison-Wesley, Reading, Massachusetts, 1969.
- [XS89] X. Xie and J.D. Simon. Picosecond time-resolved circular dichroism spectroscopy: experimental details and applications. *Reviews of Scientific Instruments*, 60:2614, August 1989.
- [Yeh00] A.T. Yeh. Ultrafast Excited State Dynamics of Tris-(2,2'-Bipyridine) Ruthenium(II). Doctoral Thesis; University of California, Berkeley and Lawrence Berkeley National Laboratory; March 2000.
- [ZZ96] A.A. Zholents and M.S. Zolotarev. Femtosecond X-Ray Pulses of Synchrotron Radiation. *Physical Review Letters*, 76:912, February 1996.
- [Zum00] S. Zumdahl, *Chemistry*. Houghton Mifflin Company, the Research Foundation of the State University of New York, and Cubic Science, Inc., 2000. Available online at <http://hmchemdemo.clt.binghamton.edu/zumdahl/docs/library.htm>

APPENDICES

- A. *Computation for slicing and evolution of slices in ring.*
part.m
- B. *Feasibility calculation for solution-state pump-probe experiment.*
snr_solution.m
- C. *Code for analog data acquisition.*
ExtScanClk_N_AI_OneShot.vi
- D. *Code for laser on/off acquisition with CCD.*
background.v,
multishot_log_laseronoff_advise.vi
- E. *Schematic & code for photon counting detection.*
Difference.vi
- F. *Code for Feedback Mirror Control for Slicing Laser Alignment.*
rooftop_passive.vi,
multishot_log_laseronoff_advise.vi

APPENDIX A

Computation for slicing and evolution of slices in ring. Written in consultation with A.A. Zholents.


```

% part.m: particle approach to electron distribution determination
% from Sasha's Deep etc. calculation

% Energy Distribution
sigmaL = (150/2.36)*sqrt(2);
c = 2.99792e10;
ncycle = (c/0.8e-4)*sigmaL*1e-15;
ar = 2*pi*ncycle;
mod = 6.3;

N = 50000;
e0 = randn(1,N);
x0 = randn(1,N); xp0 = randn(1,N);
z0 = 12*(rand(1,N)-0.5);
figure(1); plot(sigmaL*z0,e0, '.'); grid on;
energy

e1 = e0+mod*exp(-((z0.^2)/2)).*sin(ar*z0);
figure(2); plot(sigmaL*z0,e1, '.'); grid on;
interaction

% Spatial Distribution following storage ring dispersion parameters
alphaE = -(((31e-4)/c)*1e15);
alphaX = (((6e-4)/c)*1e15);
alphaXP = (((2e-4)/c)*1e15);

betax = 0.8;
disp = 0.1;
emit = 4e-9;
sigmaE = 0.8e-3;
sigmab = sqrt(betax*emit); sigmas = disp*sigmaE;
bet = sqrt((sigmab^2)/((sigmab^2)+(sigmas^2)));
syn = sqrt((sigmas^2)/((sigmab^2)+(sigmas^2)));

% no. of electrons in simulation
% normal distribution in energy
% normal distribution in transverse direction
% uniform distribution in longitudinal direction
% original particle distribution in space and

% energy modulation
% energy distribution after laser-electron

% [m]
% [m]
% [m]

```

```
x1 = bet*x0 + syn*e1;
z1 = sigmaI*z0 + alphaE*e1 + alphax*x0 + alphaxp*xp0;
% tranverse transformation
% longitudinal transformation

figure(3); plot(z1,x1, '.'); grid on; axis([-1000 1000 -8 8]);
dispersive section
% spatial distribution after
```

APPENDIX B

Feasibility calculation for solution-state pump-probe experiment.

```

% snr_solution.m
% K-edge, solution-state SNR calculation for Fe[py3tren]2+ at single x-ray wavelength
% Henry Chong, March 11, 2004.

% load solvent absorption length data files from CXRO
load acetoneitrile_attenlength.dat; aceto = acetoneitrile_attenlength;
load ethanol_attenlength.dat; ethan = ethanol_attenlength;
load methanol_attenlength.dat; metha = methanol_attenlength;
load water_attenlength.dat; water = water_attenlength;

% load sample absorption length data files from CXRO
load fepy3trencl2.dat; fecl2 = fepy3trencl2;
load fepy3trenp2f12.dat; fep2f12 = fepy3trenp2f12;

% plot solvent absorption length CXRO data in [cm-1] -- 1e-4 factor
aceto(:,2)=aceto(:,2)*1e-4;
ethan(:,2)=ethan(:,2)*1e-4;
metha(:,2)=metha(:,2)*1e-4;
water(:,2)=water(:,2)*1e-4;
figure(1);
plot(aceto(:,1),aceto(:,2),':'); hold on;
plot(ethan(:,1),ethan(:,2),'-');
plot(metha(:,1),metha(:,2),'.');
plot(water(:,1),water(:,2),'b'); hold off; grid on;
legend('acetoneitrile','ethanol','methanol','water');
title('Solvent Attenuation Length');
ylabel('Attenuation Length [cm]');
xlabel('Photon Energy [eV]');

```

```

% compute unexcited x-ray cross sections from CXRO data without EXAFS
aw_pf6 = 759.30;
aw_cl2 = 592.28;
r_pf6 = 1.753;
r_cl2 = 1.401;
Na = 6.022e23;
fec12(:,2) = (fec12(:,2))/(r_cl2*Na/aw_cl2);
fep2f12(:,2) = (fep2f12(:,2))/(r_pf6*Na/aw_pf6);
figure(2);
plot(fec12(:,1),fec12(:,2), ':'); hold on;
plot(fep2f12(:,1),fep2f12(:,2), 'b'); hold off; grid on;
title('X-ray Absorption Cross-section for Fe[py_3tren]^{2+} salts');
xlabel('Photon Energy [eV]'); ylabel('Cross-section [cm^{-2}]');
legend('Cl_2', '(PF_6)_2');

% compute fluence as a function of number density
d = 0.01;
N = (0.01:0.01:2)*6.022e20;
s_optical = 1.7e-17;
Jo = 1e16;
phi = 1;
F = ((Jo*phi)./(N*d)).*(1-exp(-s_optical*N*d));
% sample photolysis computed as a function of sample conc.
figure(3);
plot(N/6.022e20,F);
title('Sample Photolysis vs. Sample Concentration');
xlabel('Sample Concentration [M]'); ylabel ('Sample Photolysis [% of sample]'); grid on;
text(0.1*max(N/6.022e20),max(F),strcat('Maximum Photolysis = ',num2str(max(F)*100,'%0.4g','%')));

```

```

% compute No. of X-ray required at single x-ray photon energy
desiredSNR = 2; % desired SNR
xindex = 110; % index for desired x-ray energy: 110 @ 7.4088keV
ds = 0.05; % estimated change in x-ray cross-section
SNR = sqrt(4*exp(-aceto(xindex,2)*d)*exp(-
fep2f12(xindex,2)*N*d).*(sinh(F.*N*ds*fep2f12(xindex,2)*d)).^2));
figure(4); % plot required no. of x-ray photons at
plot(N/6.022e20,(desiredSNR^2)./(SNR.^2));
sample for measurement
title(strcat('No. of X-ray Photons to Resolve \Delta=', num2str(ds*100), '% change with SNR
=', num2str(desiredSNR)));
xlabel('Sample Concentration [M]'); ylabel('No. of X-ray Photons Required'); grid on;

[minval,minidx] = min((desiredSNR^2)./(SNR.^2));
text(0.1*max(N/6.022e20),1.70*mean((desiredSNR^2)./(SNR.^2)), 'Optimum Parameters:')
text(0.1*max(N/6.022e20),1.65*mean((desiredSNR^2)./(SNR.^2)),strcat('No. Photons =
', num2str(minval, '%0.4g')));
text(0.1*max(N/6.022e20),1.60*mean((desiredSNR^2)./(SNR.^2)),strcat('Concentration =
', num2str(N(minidx)/6.022e20, '%0.4g'), 'M'));
text(0.1*max(N/6.022e20),1.55*mean((desiredSNR^2)./(SNR.^2)),strcat('Photolysis =
', num2str(F(minidx)*100, '%0.3g'), '%'));

```

APPENDIX C

Code for analog data acquisition. Modified from a LabVIEW example.

ExtScanClik_N_AI_OneShot.vi
 C:\Users\Henry\Research\Slices\SliceSoftware\Analogm\ExtScanClik_N_AI_OneShot.lib\ExtScanClik_N_AI_OneShot.vi
 Last modified on 3/16/2004 at 4:33 PM
 Printed on 4/14/2004 at 6:29 PM

device (1) 1 channels 0.1.2 number of scans to acquire (1000) 1000

The scan clock rate is dictated by actual rate of the connected signal.
 time limit in sec (5 sec) 300.00 clock source

clock source code PFI pin, low to high [clock source string] 4

README file comments

Data Path Root C:\Users\Henry\Analogm\Data\6feb

Acquired Data

Histogram

array size 20000 max value 3 1.32843C min value 3 -1.50909

mean (difference) -0.001123

std deviation σ/\sqrt{N} 0.284836

σ/\sqrt{N} 0.00201

intervals 100 N 20000

Difference Array

0	0.16	-0.02	0.10	-0.10	-0.52	0.06	0.25	-0.80	0.03	-0.10	-0.17
---	------	-------	------	-------	-------	------	------	-------	------	-------	-------

Mean #2 -0.33481

Mean #1 -0.3359

difference/mean 0.00335

Error/Mean -0.0060

sigma #1/ \sqrt{N} / σ 0.0014

sigma #2/ \sqrt{N} / σ 0.0013

lock-in sig (A/D ch2) 0.00000

APPENDIX D

Code for laser on/off acquisition with CCD. Modified from LabVIEW routines originally written by S. Johnson.

```

/* BACKGROUND.V, V++ script to allow LabVIEW to control CCD */

var x dde 'stop';
var semaphore dde 'flag';
var count dde 'counter';
var ready dde 'expose';
var Image;

begin
    count := 111;
    x := 1;
    semaphore := 0;
    ready := 0;
    writeinfo('started');
    while (x=1) do
        begin
            if (semaphore=1) then
                begin
                    pvcOpenCamera('Super Camera');
                    pvcSetExpMode(pvc_ExpBulb);
                    ready := 1;
                    Image := pvcCapture(160,0,300,1023,2,2);
                    ready := 0;
                    Show(Image);
                    Image := Align( Image,0,0,2.4*pi/180,false );
                    {SetROI( Image,118,0,133,511 )};
                    Save(Image,str('E:\Henry\17nov02\17nov',count,'.tif'));
                    {Delete(Image)};
                    pvcCloseCamera('Super Camera');
                    WriteLn('17nov',str(count));
                    count := count+1;
                    semaphore := 0;
                end;
            end;
        end;
        WriteInfo('done');
    end
end

```

multishot_log_laseronoff_advise.vi
C:\Users\Henry\Research\Slice\SliceSoftware\CCD\multishot_log_laseronoff_advise.llb\
multishot_log_laseronoff_advise.vi
Last modified on 3/16/2004 at 4:56 PM
Printed on 4/14/2004 at 9:41 PM

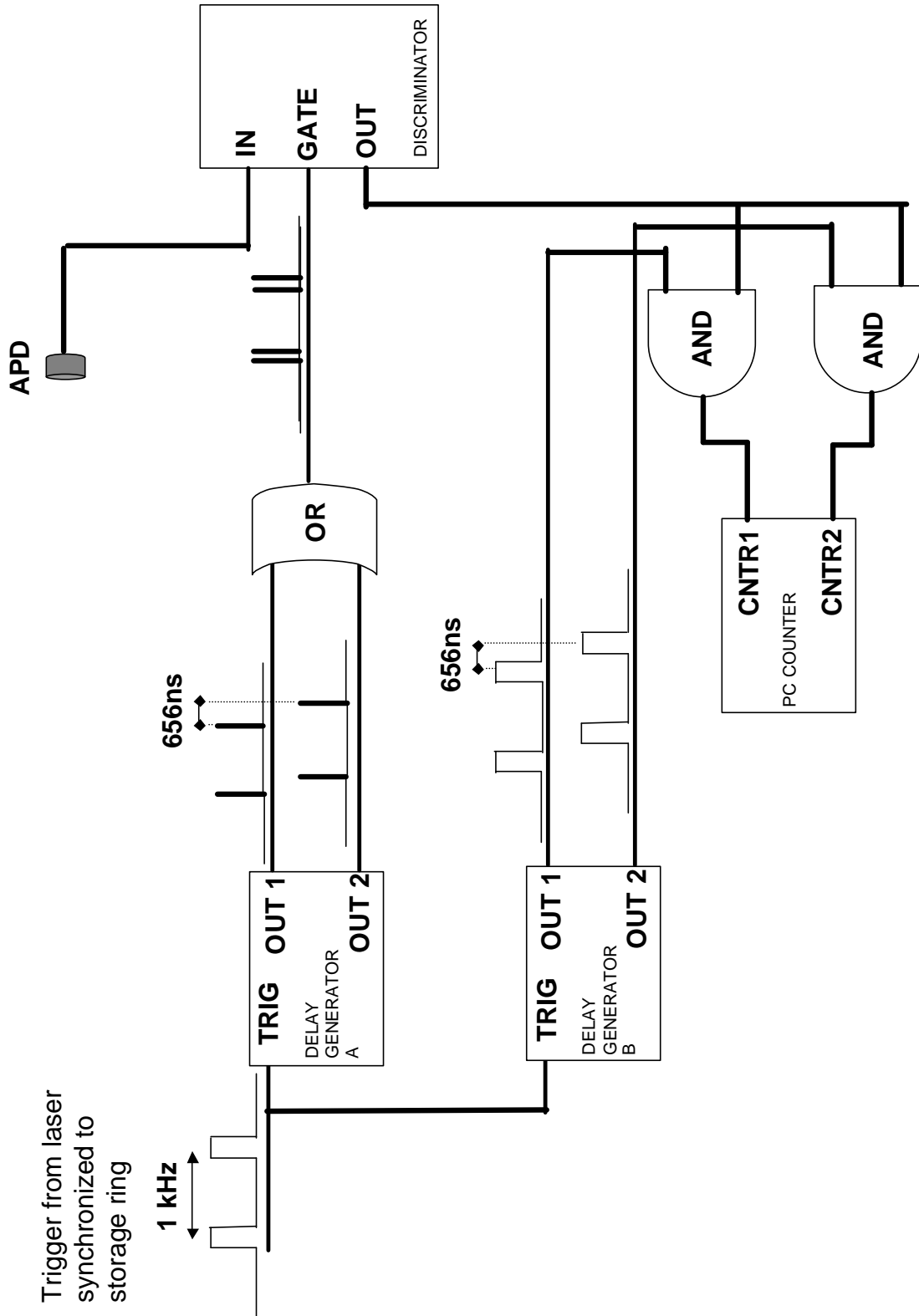
The screenshot shows a LabVIEW control panel for a laser system. The panel is titled "Laser" and features a large "LATE" indicator. The following table summarizes the visible controls and their values:

Control Label	Value
number of PAIR spectra	10
number of shots	10
current spectra index	99
time	0.00
current shot index	99
milliseconds to keep shutter open	8
shutter trig device	1
shutter trig line	1
shutter trig digital channel	0
milliseconds to wait between shots	500
camera trig device	1
camera trig digital channel	0
camera trig line	0

APPENDIX E

Schematic & code for photon counting detection.

Counter drivers written by E. Domning.

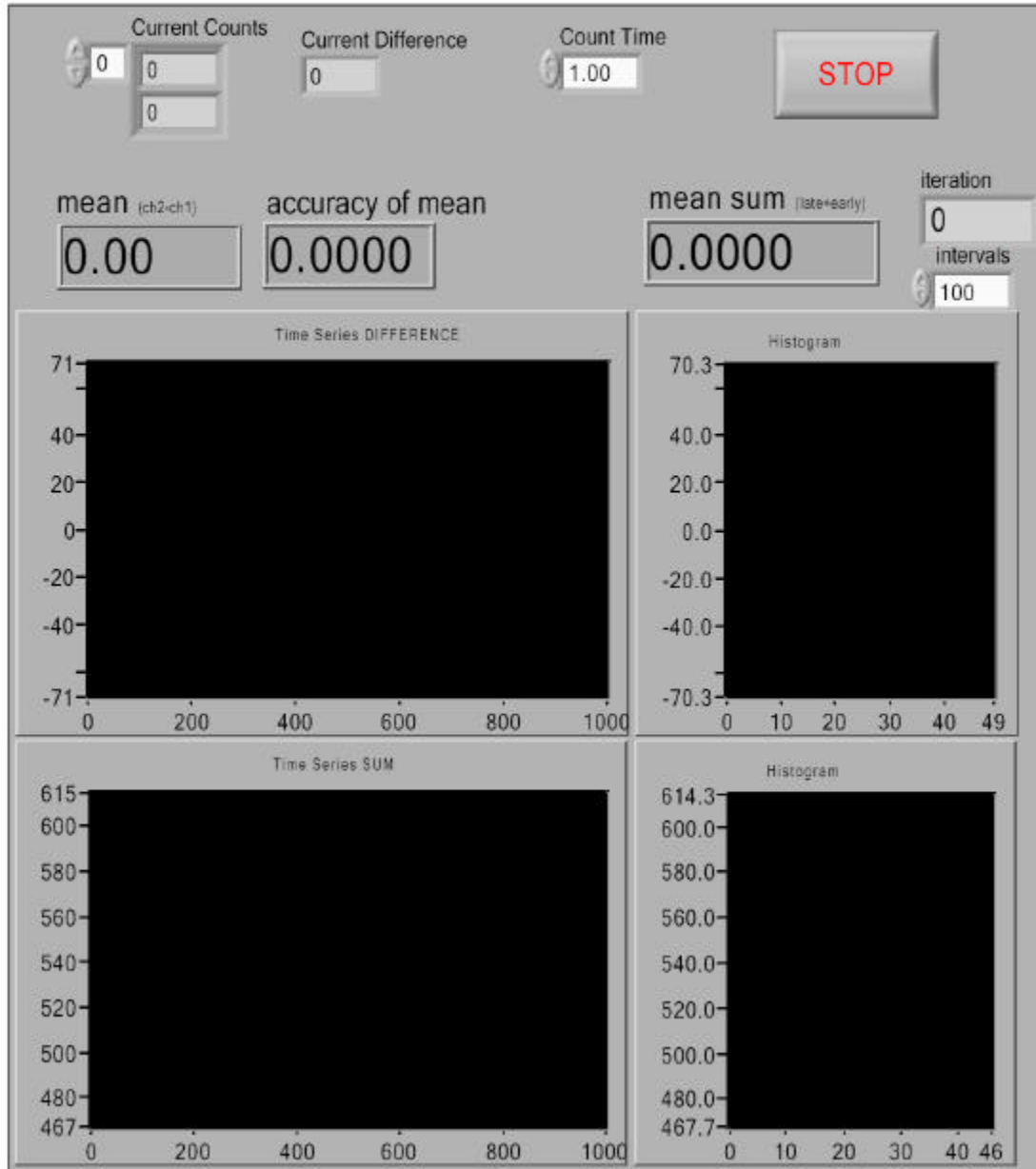


Difference.vi

C:\Users\Henry\Research\Slice\SliceSoftware\Counters\Difference.llb\Difference.vi

Last modified on 3/16/2004 at 4:35 PM

Printed on 4/14/2004 at 10:46 PM

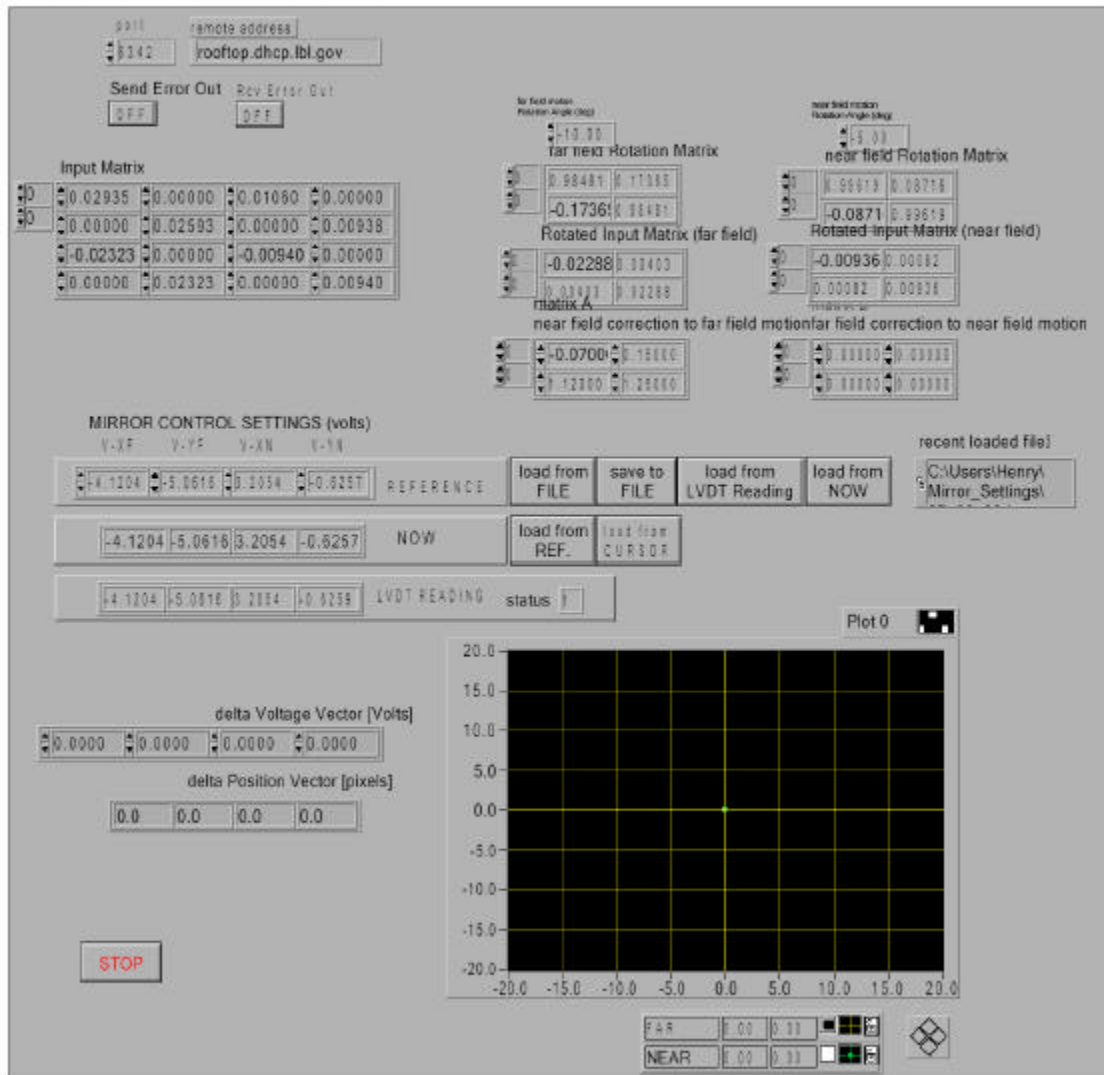


APPENDIX F

Code for Feedback Mirror Control for Slicing Laser Alignment.

Co-authored by R.W. Schoenlein.

inversion_XYinterface5.vi
 C:\Users\Henry\Research\Slice\SliceSoftware\MirrorControl\picolvdtxy.llb\
 inversion_XYinterface5.vi
 Last modified on 7/22/2003 at 4:06 AM
 Printed on 4/14/2004 at 10:37 PM



IP: rootop.dhcp.lbl.gov

Send Error Out: OFF, Recv Error Out: OFF

Input Matrix:

0	0.02935	0.00000	0.01060	0.00000
0	0.00000	0.02593	0.00000	0.00938
0	-0.02323	0.00000	-0.00940	0.00000
0	0.00000	0.02323	0.00000	0.00940

far field motion Position Angle (deg): 13.30

far field Rotation Matrix:

0.98481	0.17365
-0.17365	0.98481

Rotated Input Matrix (far field):

-0.02288	0.02400
0.01473	0.02288

matrix A

near field motion Position Angle (deg): 5.00

near field Rotation Matrix:

0.98619	0.08716
-0.08716	0.98619

Rotated Input Matrix (near field):

-0.00936	0.00082
0.00082	0.00936

near field correction to far field motion: 0.0700, 0.1800, 0.1200, 0.2000

far field correction to near field motion: 0.0000, 0.0000, 0.0000, 0.0000

MIRROR CONTROL SETTINGS (volts):

V-XF	V-YF	V-XN	V-YN
-4.1204	-5.0616	3.2054	-0.8257
-4.1204	-5.0616	3.2054	-0.8257
-4.1204	-5.0616	3.2054	-0.8257

recent loaded file: C:\Users\Henry\Mirror_Settings\



delta Voltage Vector [Volts]: 0.0000, 0.0000, 0.0000, 0.0000

delta Position Vector [pixels]: 0.0, 0.0, 0.0, 0.0

STOP

Plot 0: A 2D plot with axes from -20.0 to 20.0. A central point is visible at (0,0).

Legend:

FAR	0.00	0.33	
NEAR	0.00	0.33	



rooftop_passive.vi

C:\Users\Henry\Research\Slice\SliceSoftware\MirrorControl\picol\vdtdt.llb\

rooftop_passive.vi

Last modified on 9/13/2000 at 5:59 PM

Printed on 4/15/2004 at 8:45 AM

set values				command
0	0.00000	0.00000	0.00000	0.00
		Send Error Out	Rcv Error Out	
		OFF	OFF	
port				
6342				
remote address				
control_area.dhcp.lbl.gov				